This thesis project *in cotutela* has been supported by a grant from "*Universitá Italo-Francese*" , *Bando Vinci 2007.*

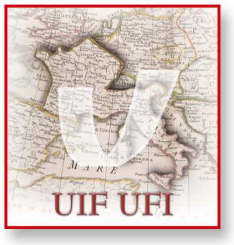

Logo Univeristá Italo-Francese

Univeristá Italo-Francese: Segretariato di Collegno, P.zza Cavalieri dell'Ordine Supremo della Ss.ma Annunziata 10093 Collegno (TO), Secrétariat Général de Grenoble: BP25 Domaine Universitarie, F-38040 Grenoble cedex 9.

Contents

Chapter 1

Magnetohydrodynamic turbulence

1.1 The magnetohydrodynamic description of plasmas

1.1.1 The descriptions of plasma

Plasmas are gases composed mainly by charged particles, representing the "fourth state" of the matter. Even if plasmas are very rare on Earth (for example, the channels electric discharges go through, as in lightenings), about 99% of the matter in the universe is in the state of plasma.

The dynamic of a plasma is rather complex, due to the electromagnetic nature of the interactions between the charged particles composing the gas. Nonetheless, it can be described, using sets of equations, at different approximation levels (Akhiezer *et al.*, 1975). Before introducing the magnetohydrodynamic description of a plasma, it is useful to define some quantity which can characterize the state of the plasma. Let us reduce, for the sake of semplicity, to two kinds of particles, namely electrons (e) and a single kind of positive ions (i, mainly protons). Let $n_{e,i}$ be the density of the particles, $m_{e,i}$ their mass, and e the electron charge. Then:

- The typical particle velocity can be represented by their thermal velocity:

$$v_{e,i} \simeq \sqrt{k_B T_{e,i}/m_{e,i}} \, ,$$

where $T_{e,i}$ are the average temperatures of the particle gases, and k_B is the Boltzmann constant.

- The *electron plasma frequency* is the typical oscillation frequency of a plasma seen as an oscillator, and its reciprocal gives the typical separation time between charges:

$$\omega_{pe} \simeq \sqrt{\frac{4\pi n_e e^2}{m_e}} \, .$$

  The *ion plasma frequency* can also be defined, using the ion mass, density and charge.

- The *Debye lenght* is the ratio between the thermal speed of electrons and the plasma frequency:

$$\lambda_D \simeq \frac{v_e}{\omega_{pe}} \simeq \sqrt{\frac{k_B T}{4\pi n_e e^2}} \, ,$$

  and is the typical shielding lenght of the charges. In fact, it represents the balance lenght between thermal and electrostatic effects, so that for scales larger than λ_D, the plasma can be seen as electrically neutral.

- The *cyclotron frequency* of electrons and ions is defined if an external magnetic field B is present, which is often the case in plasmas. In that case, the frequency at which electrons and ions turn around the magnetic field lines is

$$\Omega_{e,i} = \frac{eB}{cm_{e,i}}$$

  c being the speed of light.

- The parameter $\beta = (8\pi p)/B^2$, p being the kinetic pressure, is the ratio between the kinetic and magnetic pressures. It is useful to describe the state of magnetization of the plasma, and to individuate if magnetic or kinetic effects are predominant in the dynamic.

All these quantities can be used to describe the conditions of the plasma, and to use approximations, in order to semplify the equations in the different

Plasma	T (K)	n_e	B (Gauss)	λ_D (cm)	ω_{pe} (Hz)	Ω_i (Hz)
SC	10^6	10^6	10^2	10	10^8	10^9
SW	10^5	10	10^{-4}	10^3	10^5	10^3
MS	10^8	1	10^{-3}	10^5	10^5	10^4
IS	10^3	10^{10}	1	10^{-3}	10^{10}	10^7
IM	10^4	1	10^{-5}	10^3	10^5	10^2

Table 1.1: Typical values of some parameters for different kinds of astrophysical plasmas. SC = Solar Corona; SW = Solar Wind at 1 AU; MS = Magnetosphere; IS = Ionosphere; IM = Interstellar Medium.

regimes. Typical values of the previous quantities in different plasma systems are displayed in the Table 1.1, revealing the extremely wide range in which they lay. The Figure 1.1 illustrates different examples of plasmas in a density-temperature diagram.

1.1.2 The magnetohydrodynamic description

Since plasmas can be seen as gases, a statistical description seems to be the more appropriate. The presence of electromagnetic interactions is a further complication of the dynamic of the system. However, it is often possible to look at the plasma as a non neutral fluid, when the scales involved are large enough to forget about, for example, the collisions between particles.

At the most detailed level, the evolution of the distribution functions of the different kind of particles are described by the Liouville equation. Using some assumption the *Vlasov equation* can be obtained, and used to describe the dynamics, together with the *Maxwell equations*. The particle densities and their velocities, as well as higher order moments, can then be obtained by integration of the distribution functions. This kind of approach is useful when a microscopic description of the system is needed. Collisions between particles are taken into account at this level.

Very often one is interested in a large scale description of the plasma, neglecting the effects of particles collisions, and considering the dynamics of each single kind of particles as a whole. When this is the case, the so called *fluid* description can be used. In this picture, the plasma can be seen as

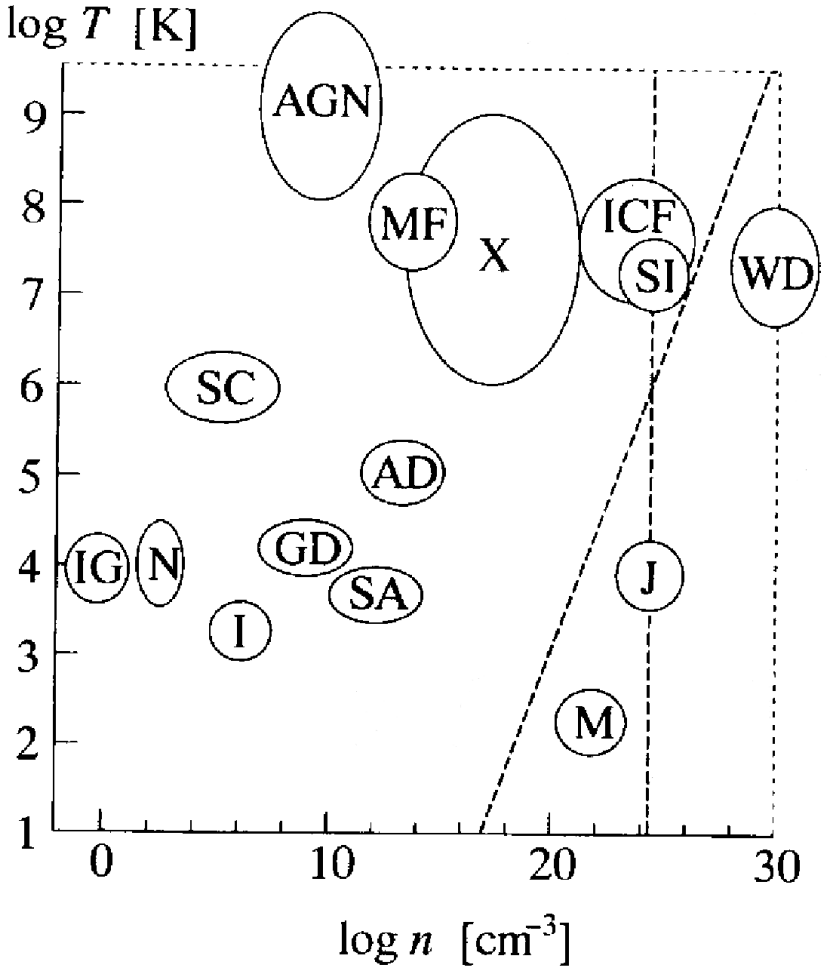

Figure 1.1: Temperature-density diagram showing different plasma regimes. interstellar gas (IG), gas nebulæ (G), ionosphere (I), solar chromosphere (SA), arc discharge (AD), solar corona (SC), active galactic nuclei (AGN), magnetic fusion (MF), X-ray source star (X), inertial fusion (ICF), solar interior (SI), metal (M), Jupiter interior (J) and white dwarf (WD).

a superposition of interacting fluids, each one composed of a single kind of particles, and thus each one obeying to a (non-closed) set of fluid-like equations. Non-collisionality of the plasma requires termalization, so that the distribution functions of the particles can be approximated by Maxwellians. Of course this can be only done if the dynamical time scales are larger than the typical termalization time. This condition is referred to as *local termodynamical equilibrium (LTE)*. In that case, conservation laws can be written, by integration of the Vlasov equation, for the moments of the particle distributions, leading to the set of the moment equations. For each particle species, these are the conservation laws for mass, moment, energy and so on. A closure hypothesis, as for example a state equation, is required to close the hierarchy of the moment equations. Moreover, the Maxwell equations, together with the Ohm's law, are needed in order to describe the electromagnetic interations.

Still, the fluid equations are quite difficult to use, and further approximations can be made in order to semplify them. This can be done if some assumptions are satisfied, leading to the *magnetohydrodynamic* (MHD) description of a plasma. First of all, the particle involved are electrons (of mass m_e) and protons (of mass m_p), or even heavyer ions. Since $m_p \sim 2000 m_e$, it is clear that terms containing m_e/m_p can be neglected with respect to unity or m_p/m_e. This corresponds to ignore the inertia of the electrons in the flow. In a plasma, electrons and protons can interact through coulomb interactions, so that particles oscillate at their plasma frequency ω_p. We consider now large time scales, at which we do not "see" the plasma oscillations. The plasma can then be seen as a proton fluid, described by a fluid-like equation, "followed" by an electron current obeying the Ohm's law. The current follow the flow with a delay of the order of the separation time, which is not detectable, so that we can neglect it. For time scales larger than the reciprocal of the electron plasma frequence, and for spatial scales larger than the Debye lenght, the *quasi-neutrality of charge* is assured and the plasma can be considered as electrically neutral. Finally, when nonrelativistic regime is concerned, all the contributions of order $(v/c)^2$ can be neglected in the equations. The conservation laws can then be written for the mass density ρ, flow velocity $\boldsymbol{v}$

and internal energy per mass unit U of the protons (Akhiezer *et al.*, 1975):

$$\frac{\partial \rho}{\partial t} + \boldsymbol{\nabla} \cdot (\rho \boldsymbol{v}) = 0 \tag{1.1}$$

$$\rho \left[\frac{\partial}{\partial t} + (\boldsymbol{v} \cdot \boldsymbol{\nabla}) \right] \boldsymbol{v} = \boldsymbol{f} - \boldsymbol{\nabla} p + \boldsymbol{\nabla} \cdot \overline{\overline{\boldsymbol{\sigma}}} \tag{1.2}$$

$$\rho \left[\frac{\partial}{\partial t} + (\boldsymbol{v} \cdot \boldsymbol{\nabla}) \right] U = -p(\boldsymbol{\nabla} \cdot \boldsymbol{v}) - \boldsymbol{\nabla} \cdot \boldsymbol{q} + \sum_{i,j} \sigma_{ij} \frac{\partial v_i}{\partial x_j} + Q \; . \tag{1.3}$$

In previous equations, $\boldsymbol{f}$ represents the sum of the external forces acting on the magneto-flow per unit mass. The term $\overline{\overline{\boldsymbol{\sigma}}}$ is the stess tensor excluding the kinetic pressure p contribution, which is treated separately. The term $\boldsymbol{q}$ is the heat flux, and Q is the heat produced inside the system. In many cases, as for the plasmas treated whithin the present work, the only force involved is the Lorentz force. In fact, other kinds of forces, as the gravitational one, are negligible with respect to the electromagnetic interactions. In this case, the force term can be written as:

$$\boldsymbol{f} = \frac{1}{c} \boldsymbol{J} \times \boldsymbol{B} \; . \tag{1.4}$$

where the quasi-neutrality has been used to drop the electric field contribution to the force, that is to use the Laplace force. The same arguments hold for the heat terms, so that the Joule effect is often the only internal source of heat. It is worth mentioning again that the previous equations are not closed. In fact, a closure hypothesis is needed. It is often possible to use a state equation, so that the number of unknowns is reduced and the system is closed. For example, if the plasma behaves like a perfect gas, the state equation $p = k_B \rho T / m$ can be used to eliminate the kinetic pressure from the equations.

The moments equations must be coupled to the Maxwell equations to include the electromagnetic properties of the plasma. In case of quasi-neutrality of charge, and in non-relativistic regime, the Maxwell equations become:

$$\boldsymbol{\nabla} \cdot \boldsymbol{E} = 0 \tag{1.5}$$

$$\boldsymbol{\nabla} \cdot \boldsymbol{B} = 0 \tag{1.6}$$

$$\boldsymbol{\nabla} \times \boldsymbol{E} = -\frac{1}{c} \frac{\partial \boldsymbol{B}}{\partial t} \tag{1.7}$$

$$\boldsymbol{\nabla} \times \boldsymbol{B} \;=\; \frac{1}{c}\frac{\partial \boldsymbol{E}}{\partial t} + \frac{4\pi}{c}\boldsymbol{J} \tag{1.8}$$

where $\boldsymbol{E}$ and $\boldsymbol{B}$ are the electric and magnetic fields respectively, ρ_c is the charge density and $\boldsymbol{J}$ the current density. The Ohm's law, in the MHD framework, is rewritten in its generalized form as:

$$\boldsymbol{E} + \frac{1}{c}\boldsymbol{v} \times \boldsymbol{B} = \eta \nabla^2 \boldsymbol{B} \; . \tag{1.9}$$

where η is the resistivity of the plasma.

The Laplace force (1.4), the last Maxwell equation (1.8) and the Ohm's law (1.9) can be now used to rewrite the conservation laws. The mass conservation law (1.1) remains invariate, and so does the energy conservation law (1.3), as far as we don't use any state equation. The impulse conservation law, also called the Newton equation, become

$$\rho \left[\frac{\partial}{\partial t} + (\boldsymbol{v} \cdot \boldsymbol{\nabla}) \right] \boldsymbol{v} = \frac{1}{4\pi}(\boldsymbol{\nabla} \times \boldsymbol{B}) \times \boldsymbol{B} - \boldsymbol{\nabla} p + \boldsymbol{\nabla} \cdot \overline{\overline{\boldsymbol{\sigma}}} \tag{1.10}$$

The Maxwell equation (1.7) is used to describe the evolution of the magnetic field. In the MHD framework, it can be rewritten as

$$\frac{\partial \boldsymbol{B}}{\partial t} = \boldsymbol{\nabla} \times (\boldsymbol{v} \times \boldsymbol{B}) + \frac{c^2 \eta}{4\pi} \nabla^2 \boldsymbol{B} \tag{1.11}$$

and is called the *induction equation*.

Equations (1.1), (1.10), (1.11) and (1.3) are the full set of the MHD equations, and together with the remaining Maxwell laws, the Ohm's law, and a state equation for the closure, can be used to describe the dynamics of a plasma in the magnetohydrodynamic approximation. It is worth noting that the unknowns ρ, p, $\boldsymbol{B}$, $\boldsymbol{v}$ are seen in a reference frame comoving with the flow, and represent the fields as average over volumes of space smaller than the scales we want to study, but larger than the collisional scales ($\sim \lambda_D$), as required for MHD to be valid. It is clear that the heat terms q and Q, as well as the stess tensor $\overline{\overline{\sigma}}$, could introduce new variables in the equations, and thus need to be modeled in order to solve the equations.

The MHD equations own a similar structure to the Navier-Stokes equations (NS), which describe the dynamic of a fluid. The main characteristic of

both sets of equations is the presence of non-linear terms, but the MHD equations have extra terms describing the coupling between velocity and magnetic field. As will be discussed in the following, these nonlinearities lead to scaling of the equations, which is prelude to turbulence.

1.1.3 The incompressible case and the Elsässer variables

As for the NS equations in the fluid case, the MHD equations are strongly simplified if the flow is incompressible, that is if the density is a constant, $\rho = constant$. The mass conservation law become simply the incompressibility condition $\boldsymbol{\nabla} \cdot \boldsymbol{v} = 0$. The energy conservation equation can also be dropped. Let us introduce the following new variable

$$\boldsymbol{b}(\boldsymbol{r}, t) = \frac{\boldsymbol{B}}{\sqrt{4\pi\rho}} \, .$$

In the incompressible case, since ρ is constant the field $\boldsymbol{b}$ is proportional to the magnetic field $\boldsymbol{B}$ only, but with the dimension of a velocity. Using incompressibility, replacing the magnetic field with the field $\boldsymbol{b}$, and introducing the kinematic viscosity ν and the magnetic diffusivity $\mu = \frac{c^2\eta}{4\pi\rho}$, the (incompressible) MHD equations can be written in the simpler form:

$$\begin{aligned} \frac{\partial \boldsymbol{v}}{\partial t} + (\boldsymbol{v} \cdot \boldsymbol{\nabla})\boldsymbol{v} &= (\boldsymbol{\nabla} \times \boldsymbol{b}) \times \boldsymbol{b} - \boldsymbol{\nabla} p + \nu \nabla^2 \boldsymbol{v} && (1.12) \\ \frac{\partial \boldsymbol{b}}{\partial t} &= \boldsymbol{\nabla} \times (\boldsymbol{v} \times \boldsymbol{b}) + \mu \nabla^2 \boldsymbol{b} && (1.13) \\ \boldsymbol{\nabla} \cdot \boldsymbol{v} &= \boldsymbol{\nabla} \cdot \boldsymbol{b} = 0 \, . && (1.14) \end{aligned}$$

The previous equations can be compacted introducing the Elsässer variables (Elsässer, 1950):

$$\boldsymbol{z}^{\pm} = \boldsymbol{v} \pm \boldsymbol{b} \tag{1.15}$$

The Elsässer variables are useful when we want to study, for example, the correlation between the fluctuations of velocity and magnetic field. Using these new variables, the MHD equations become

$$\frac{\partial \boldsymbol{z}^{\pm}}{\partial t} + (\boldsymbol{z}^{\mp} \cdot \boldsymbol{\nabla})\boldsymbol{z}^{\pm} = -\frac{1}{\rho}\boldsymbol{\nabla}\left(p + \frac{B^2}{8\pi}\right) + \frac{\nu+\mu}{2}\nabla^2\boldsymbol{z}^{+} + \frac{\nu-\mu}{2}\nabla^2\boldsymbol{z}^{-} \quad (1.16)$$

$$\boldsymbol{\nabla} \cdot \boldsymbol{z}^{\pm} = 0 \quad (1.17)$$

This is a very compact, symmetric set of four equations. It is worth noting that the nonlinear term is proportional to both variables, so nonlinearities vanishes if one of the Elsässer fields is zero, that is the solution $\boldsymbol{z}^{\mp} = 0$ and $\boldsymbol{z}^{\pm} \neq 0$ is a result of the nonlinear equations. In case of vanishing magnetic field, the two "+" and "–" equations (1.16) become identical, as well as the two equations (1.17), and the NS equations are recovered.

1.2 Scaling and turbulence

1.2.1 The Reynolds number

The nonlinear structure of the MHD equations lead to turbulence. In the framework of turbulence phenomenology, it is possible to individuate, within the MHD equations, different terms whose contribution to the dinamics depends on the particular regime. In particular, nonlinear terms and dissipative ones are present. In fluid dynamic, the usual way to look at the balance between these terms is by the so called *Reynolds number Re*. As a phenomenological approach is required, let us introduce some typical values for the main variables in the MHD equations. So, let ℓ_0 be a typical lenght scale of the system, v_0 and B_0 typical (average) velocity and magnetic field. It is useful to introduce the *Alfvèn velocity*

$$c_A = \frac{B_0}{\sqrt{4\pi\rho}}$$

representing the typical propagation velocity for Alfvèn waves (see for example Akhiezer *et al.*, 1975). By dimensional analysis, the nonlinear term $(\boldsymbol{v} \cdot \nabla)\boldsymbol{v}$ of the MHD equations (or the NS equations) is then $\sim v_0^2/\ell_0$. For the dissipative term in the same equation, $\nu\nabla^2\boldsymbol{v} \sim \nu v_0/\ell_0$, so that the ratio

between the two terms gives the (kinematic) Reynolds number:

$$R_v = \frac{\ell_0 v_0}{\nu} \, .$$

In analogy, a *magnetic Reynolds number* is also defined as

$$R_m = \frac{\ell_0 c_A}{\mu} \, .$$

For low Reynolds numbers, it is clear that the (linear) dissipative terms dominate the dynamics. The nonlinear interactions are small enough for the equations to be linearized, and thus solved. In fluid dynamics, this is referred to as "laminar" regime. As the Reynolds numbers reach or overcome unity, the nonlinear terms become important. The effect of the presence of such terms is easily seen looking at the frequency representation of the equations (for example, in the Fourier decomposition). In that case, the nonlinear term can be represented as

$$(\boldsymbol{v} \cdot \nabla)\boldsymbol{v} \rightarrow (\boldsymbol{v}_{\boldsymbol{k_1}} \cdot i\boldsymbol{k_2}\boldsymbol{v}_{\boldsymbol{k_2}})$$

so that interactions (energy exchanges) between the different wave vectors $\boldsymbol{k_1}$ and $\boldsymbol{k_2}$ are permitted in a triangular way, so that a new wave vector is involved, $\boldsymbol{k_1} + \boldsymbol{k_2} = \boldsymbol{k}$ (see Dobrowolny et al., 1980).

1.2.2 The turbulent cascade

In fluid dynamics, one of the main features of turbulence is the presence of singular structures, as for examples vortices (or eddies). At low Reynolds numbers, as the nonlinear terms begin to be non-negligible, large turbulent structures are formed at some typical scale ℓ_0 (for example the size of an obstacle in a flow, or the mesh size of a grid, or the distance between the walls in a channel). As the Reynolds number increases, the energy is transferred from largest vortices to smaller and smaller structures, because of the nonlinear interactions. When the Reynolds number is larger than some critical value, the flow is said to be in *fully developed turbulence* regime. In these conditions, the fields are highly chaotic, with overlapping of different structures over a whide range of scales. In fully developed turbulence it is possible

to individuate three different ranges of scales. The large scales, at which the energy is injected into the system from some external forcing, are called *integral scales*. The scales at which the dissipation is dominant belong to the *dissipative range*. Between these two ranges, in which the dynamics is linear, the dominant term in the equations is the non-linear term, so that energy transfers between different wave-vectors are dominating the dynamics. This range of scales is usually called "inertial range"[1].

This idea has been first visualized in the simple picture of an energy cascade by Richardson (1922). Figure 1.2 is a representation of such cascade. In this framework, the energy is injected in the sistem at the integral scale (the large scale ℓ_0 in the picture) at some rate ε. Since non-linear interactions are present, such energy "cascades" through a hierarchy of smaller and smaller structures within the inertial range. In the Richardson picture, the energy transfer is assumed to have the same rate ε as the energy injection. At smaller scales the dissipation become dominant so that the cascade is eventually stopped and the energy is dissipated, always at rate ε.

1.2.3 The field increments

The energy cascade through the scales can be labeled introducing a scale dependent Reynolds number, simply using a scale ℓ, and the typical fields v_ℓ and b_ℓ associated with such scale:

$$R_v(\ell) = \frac{\ell v_\ell}{\nu} \qquad R_b(\ell) = \frac{\ell b_\ell}{\eta} \, .$$

These numbers allow to estimate the scale at which the dissipative terms of the equations (MHD or NS) become dominant with respect to the nonlinear terms, and the cascade is stopped. The usual tool to study the turbulent cascade is by way of the field increments. Given a field $\boldsymbol{\psi}(\boldsymbol{r})$ one can define the following variables:

$$\delta\boldsymbol{\psi}_\ell(\boldsymbol{r}) = \boldsymbol{\psi}(\boldsymbol{r}+\boldsymbol{\ell}) - \boldsymbol{\psi}(\boldsymbol{r}) \, . \tag{1.18}$$

[1]Due to the shape of the nonlinear terms of MHD equations, in MHD this picture is real only when the correlations between velocity and magnetic field $\boldsymbol{v}\cdot\boldsymbol{b}$ are small.

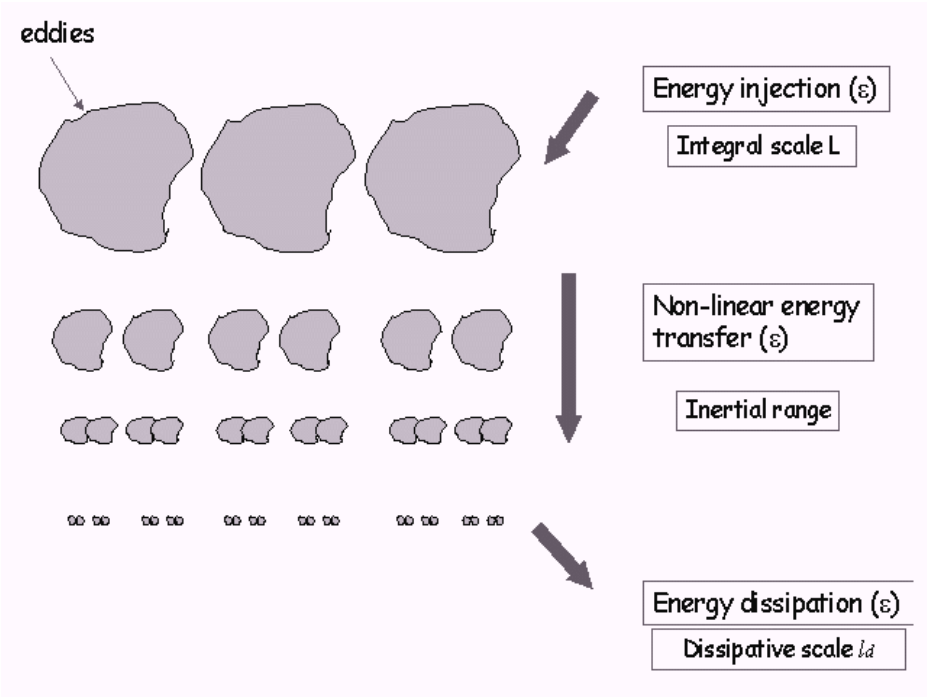

Figure 1.2: A schematic picture of the Richardson cascade. The hierarchy of structures represents the non-linear transfer of energy between different scales.

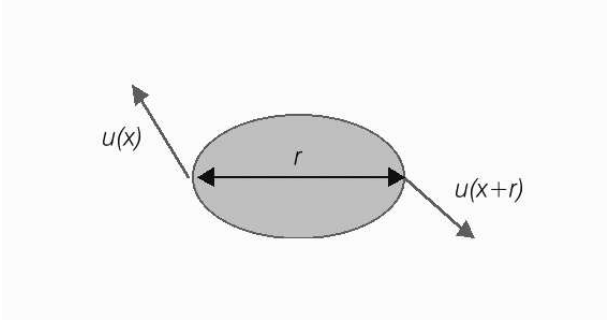

Figure 1.3: A schematic image showing how the field differences can be used to represent the presence of vortical structures. In fact, in correspondence of such structures, the velocity increment computed at the scale of the structure is high when, the velocities being directed in opposite directions at the edges of the eddy.

As can be easily understood, these variables can give informations about the presence of structures in the field at a given scale ℓ (see Figure 1.3), and can be used as typical field values to compute the Reynolds numbers. The field increments are stochastic variables, and a statistical approach is needed.

1.2.4 Energy spectra

We will now introduce some well known concepts in order to point out the relationship between the classical tools used for the analysis of turbulent fields. Given a stochastic field $\boldsymbol{\psi}(\boldsymbol{r})$, the Fourier transform of its i-th component is

$$\psi_i(\boldsymbol{r}) = \int \hat{\psi}_i(\boldsymbol{k}) \mathrm{e}^{i\boldsymbol{k}\,\cdot\,\boldsymbol{r}}\, d^3\boldsymbol{r}\ .$$

If homogeneity and isotropy are assumed, the associated energy spectrum is

$$E(k) = 4\pi k^2 U(k)$$

where $U(k) = |\hat{\psi}(\boldsymbol{k})|^2/2$. The energy spectrum is simply related to the autocorrelation function

$$\frac{1}{2}\langle \psi_i(\boldsymbol{r})\psi_j(\boldsymbol{r})\rangle = \int_0^\infty E(k)\, dk\ . \tag{1.19}$$

Energy spectra are powerful turbulence analysis tools. In fact, they allow a description which is able to capture the main energy cascade features.

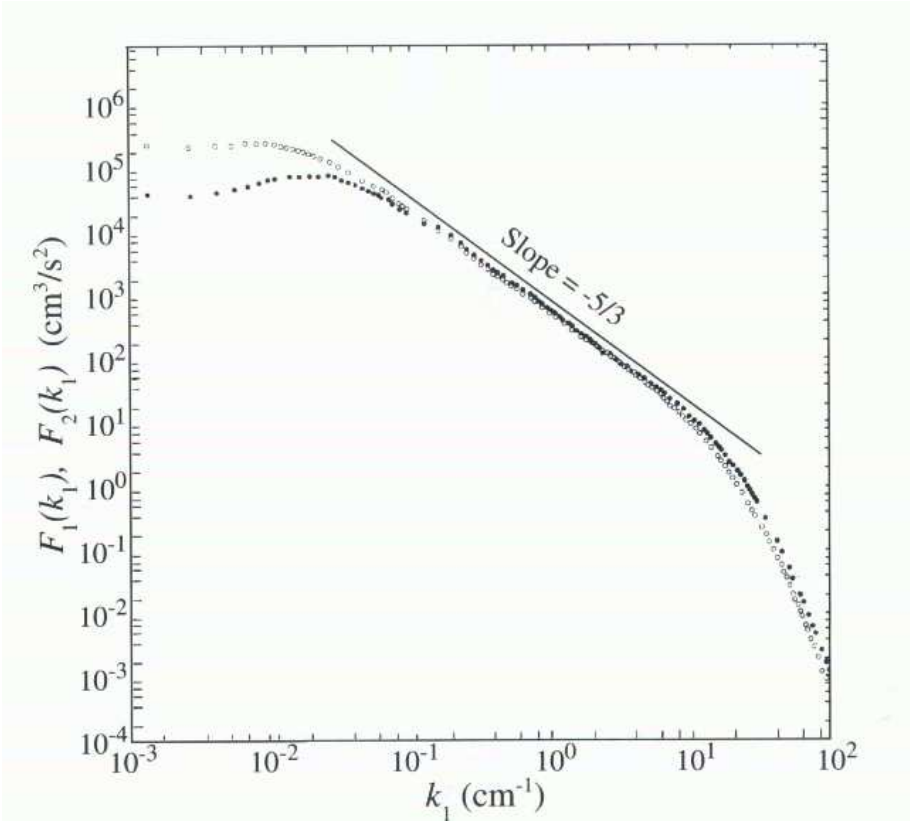

Figure 1.4: The energy spectra of the streamwise component (white circles) and lateral component (black circles) of velocity fluctuations in high Reynolds number jet (from Frisch, 1995).

In particular, it is found that the energy spectrum of a turbulent field has power-law behavior (Kolmogorov, 1941; see also Frisch, 1995)

$$E(k) \sim k^{-\alpha} \tag{1.20}$$

which defines the inertial range of the energy cascade. Figure 1.4 shows an example of spectrum for fluid case. The different ranges described by the Richardson cascade can be easily identified in the spectrum. It is easy to relate the energy spectra to the field increments variance. Using the relation (1.19) and recalling that:

$$\frac{1}{2}\langle \psi_i(\boldsymbol{r})\psi_j(\boldsymbol{r}+\boldsymbol{\ell})\rangle = \int_0^\infty E(k)\,\frac{\sin k\ell}{k\ell}\,dk\;,$$

it is straightforward to figure out that

$$\langle |\psi_i(\boldsymbol{r}+\boldsymbol{\ell}) - \psi_i(\boldsymbol{r})|^2 \rangle = 4 \int_0^\infty E(k) \left(1 - \frac{\sin k\ell}{k\ell}\right) dk \; . \tag{1.21}$$

If the spectrum $E(k)$ decreases slowly enough (a power law with exponent $\alpha > 1$), then the main contribution to the integral (1.21) comes from $E(k)$, at least for scales smaller than the large scale ℓ_0, so that the energy spectrum is directely related to the second order moment of the field increments.

1.2.5 Probability distribution functions (PDFs)

As we are dealing with stochastic variables, a statistical approach can provide informations about the physical properties of the system. In particular, it is interesting to capture the reproducible features of the signal, and this can be done only through the statistical properties. The main statistical tool is the Probability Distribution Function (PDF) of the field increments. We present here some relationship between PDFs and other useful tools as energy spectra and structure functions.

If the PDF $P(x)$ of a stochastic variable x is known, then it is possible to compute the infinite set of moments defined as:

$$\langle x^n \rangle = \int x^n \, P(x) \, dx \; . \tag{1.22}$$

Let us introduce the characteristic function of $P(x)$, (*i. e.* its Fourier transform)

$$\Phi(k) = \int \mathrm{e}^{ikx} \, P(x) \, dx = \langle \mathrm{e}^{ikx} \rangle \; ;$$

using the Taylor series to develop the exponential e^{ikx},

$$\Phi(k) = \int dx \, P(x) \sum_{m=0}^{\infty} \frac{(ik)^m}{m!} x^m \; = \sum_{m=0}^{\infty} \frac{(ik)^m}{m!} \langle x^m \rangle \; , \tag{1.23}$$

Transforming backward to the physical space

$$P(x) = \frac{1}{2\pi} \int dk \; \sum_{m=0}^{\infty} \frac{(ik)^m}{m!} \langle x^m \rangle \, \mathrm{e}^{-ikx} \; . \tag{1.24}$$

so that it is possible to compute the PDF of a stochastic variable if all the moments $\langle x^m \rangle$ are known. Note that for experimental purposes, given the

stochastic signal provided by some measurements, it is in principle possible to use the ergodic theorem to compute the moments of the signal without the knowledge of the PDF, as would be required to apply equation (1.25). In fact, by deriving n times equation (1.23) and putting $k = 0$, it is possible to recompute the moments directely from the data even if the PDF is unknown:

$$\langle x^n \rangle = \frac{1}{i^n} \frac{d^n \Phi}{dk^n}\bigg|_{k=0} . \tag{1.25}$$

Gaussian PDFs are a peculiar case. It is a very interesting PDFs class, both because of its large presence in real systems, and for its statistical properties. In fact it is very easy to show that a Gaussian PDF needs only the first two moments to be completely determined. The first order moment is the average, and is generally used to translate the PDF so that the new PDF is meanless. The second order moment is the variance $\sigma^2 = \langle (x - \langle x \rangle)^2 \rangle$. The gaussian being a even function, the odd order moments are trivially zero. Let us compute now the even order $(2n)$ moments using the relation (1.25). It is well known from the Fourier transformation that the characteristic function of a gaussian is itself gaussian, with standard deviation $\sigma' = 1/\sigma$:

$$\Phi(k) = \mathrm{e}^{-\frac{1}{2}\sigma^2 k^2} .$$

The derivative can be computed using the Hermite polinomials $H_n(y)$ of order n, that is:

$$\frac{d^n}{dk^n} \mathrm{e}^{-y^2} = (-1)^n \mathrm{e}^{-y^2} H_n(y) .$$

Then, using $y = \sigma k/\sqrt{2}$ the even moments can be written as:

$$\langle x^{2n} \rangle = (-1)^n (-1)^{2n} \mathrm{e}^{-y^2} H_{2n}(y) \frac{d^{2n} y}{dk^{2n}}\bigg|_{k=0} = (-1)^n 2^{-n} H_{2n}(0) \sigma^{2n} \tag{1.26}$$

that is, all the moments of order larger than two are trivially computed from the variance, or they are zero. So, the gaussian PDF can be built up knowing only the average and the variance of the stochastic variables, for example using the power spectrum. In other words, energy spectra play the fundamental role in the classical picture of turbulence, where gaussian PDFs are hypothized.

Of course for non Gaussian distributions all the infinite set of the moments is required to build the PDF using equation (1.24), so that the energy spectra lose their key role.

1.2.6 Structure functions

The spectral analysis does not provide a complete description of the statistical properties of the field, unless this has Gaussian PDF. In fact, we have seen that spectra are a representation of the second order moment. For non Gaussian fields, the properties of turbulence can be described using the *longitudinal structure functions* to represent the higher order moments of the field. The structure function are defined as:

$$S_p(\ell) = \langle \delta\psi_\ell^p \rangle \tag{1.27}$$

where

$$\delta\psi_\ell = [\boldsymbol{\psi}(\boldsymbol{r}+\boldsymbol{\ell}) - \boldsymbol{\psi}(\boldsymbol{r})] \cdot \frac{\boldsymbol{\ell}}{\ell}\,. \tag{1.28}$$

are the longitudinal field increments.

1.3 Phenomenology of turbulence

1.3.1 Scaling laws of MHD equations

The NS equations own scaling properties (Frisch, 1995), that is there exists a class of solutions which are invariate under scaling transformations. Let us write the MHD equations neglecting dissipative terms

$$\frac{\partial \rho}{\partial t} + \boldsymbol{\nabla} \cdot (\rho \boldsymbol{v}) = 0 \tag{1.29}$$

$$\rho \left[\frac{\partial}{\partial t} + (\boldsymbol{v} \cdot \boldsymbol{\nabla}) \right] \boldsymbol{v} = \frac{1}{4\pi} (\boldsymbol{\nabla} \times \boldsymbol{B}) \times \boldsymbol{B} - \boldsymbol{\nabla} p \tag{1.30}$$

$$\frac{\partial \boldsymbol{B}}{\partial t} = \boldsymbol{\nabla} \times (\boldsymbol{v} \times \boldsymbol{B}) \tag{1.31}$$

$$\left[\frac{\partial}{\partial t} + (\boldsymbol{v} \cdot \boldsymbol{\nabla}) \right] \left(\frac{p}{\rho^\gamma} \right) = 0\,. \tag{1.32}$$

Let us now introduce the scaling transformations by defining a typical scale ℓ, the characteristic time t, the scaling factor λ and the characteristic scaling exponent for the time α. When the scale is changed of a factor λ, the time variable itself changes as

$$\ell \longrightarrow \lambda \ell' \quad , \quad t \longrightarrow \lambda^{\alpha} t' \; . \tag{1.33}$$

The scaling of the fields obeying to the ideal MHD equations can be described using a scaling exponent for each field, so that when $\ell \longrightarrow \lambda \ell'$

$$\boldsymbol{v} \longrightarrow \lambda^{h} \boldsymbol{v'} \quad , \quad \boldsymbol{B} \longrightarrow \lambda^{\beta} \boldsymbol{B'} \quad , \quad p \longrightarrow \lambda^{\nu} p' \quad , \quad \rho \longrightarrow \lambda^{\mu} \rho' \quad . \tag{1.34}$$

Inserting the previous relations (1.33) and (1.34) into the MHD equations, and recalling that $\boldsymbol{\nabla} \sim 1/\ell$, we obtain

$$\lambda^{\mu-\alpha} \frac{\partial \rho'}{\partial t'} + \lambda^{\mu+h-1} \boldsymbol{\nabla'} \cdot (\rho' \boldsymbol{v}) = 0 \; ,$$

$$\rho' \lambda^{\mu+h-1} \left[\frac{\partial \boldsymbol{v'}}{\partial t'} \lambda^{h} + \lambda^{2h-1} (\boldsymbol{v'} \cdot \boldsymbol{\nabla'}) \boldsymbol{v'} \right] = -\lambda^{\mu-1} \boldsymbol{\nabla'} p' + \frac{1}{4\pi} (\boldsymbol{\nabla'} \times \boldsymbol{B'}) \times \boldsymbol{B'} \lambda^{2\beta-1}$$

so that the same scaling factor is found for the whole equations if $\alpha = 1 - h$, $\mu = 2(\beta - h)$, and $\nu = 2\beta$. Under these conditions, that is, if the scaling for the fields is

$$\begin{aligned} \ell \longrightarrow \lambda \ell' \quad , \quad t \longrightarrow \lambda^{1-h} t' \quad , \quad \boldsymbol{v} \longrightarrow \lambda^{h} \boldsymbol{v'} \quad , \\ \boldsymbol{B} \longrightarrow \lambda^{\beta} \boldsymbol{B'} \quad , \quad p \longrightarrow \lambda^{2\beta} p' \quad , \quad \rho \longrightarrow \lambda^{2(\beta-h)} \rho' \quad , \end{aligned} \tag{1.35}$$

then the MHD equations remain invariate, for each value of h and β. Note that in the incompressible case, $\rho = const$, the scaling exponent is the same for velocity and magnetic field, $\beta = h$.

The scaling relations (1.35) just obtained reveal that a scaling solution must be expected:

$$\frac{\delta \psi_{\ell}}{\delta \psi_0} \sim \left(\frac{\ell}{\ell_0} \right)^{h}$$

(ψ being v or b). We are thus interested in the scaling relations of the fields fluctuations, which remain invariate for scaling transformation of the MHD equations.

1.3.2 Kolmogorov law and spectrum

As described by the Richardson cascade, the phenomenology of turbulence involves some fragmentation process of turbulent structures, which transfer energy through different scales. Kolmogorov (1941) for fluids, and then Kraichnan (1965) for MHD (see also Dobrowolny et al., 1980), did formalize such picture, giving the bases for the phenomenological analysis of turbulence.

The phenomenological approach to turbulence is mainly based on dimensional analysis and physical considerations. The equations (NS or MHD) are not directely involved. The basic ingredients are thus typical values of the variables involved in the system. First of all, as we look for scaling, we need to introduce a typical lenght ℓ; the typical values of the fields (say ψ) corresponding to such scale can be represented for example by the field increments $\delta\psi_\ell$; a characteristic time t_ℓ, associated to the scale ℓ, is also needed, as well as a local (in scale) Reynolds number $R_\ell = \ell\delta\psi_\ell/\nu$ and the mean energy transfer rate ε_ℓ. The latter can be defined for fluids:

$$\varepsilon_\ell = \frac{1}{2}\frac{\partial}{\partial t}\langle \boldsymbol{v}(\boldsymbol{r}) \cdot \boldsymbol{v}(\boldsymbol{r}+\boldsymbol{\ell})\rangle$$

and for plasmas:

$$\varepsilon = \frac{1}{2}\left(\varepsilon^{\pm} + \varepsilon^{\mp}\right)$$

where the pseudo-energy transfer rates are defined as:

$$\varepsilon^{\pm} = \frac{1}{2}\frac{\partial}{\partial t}\langle \boldsymbol{Z}^{\pm}(\boldsymbol{r}) \cdot \boldsymbol{Z}^{\pm}(\boldsymbol{r}+\boldsymbol{\ell})\rangle$$

and take into account both magnetic and kinetic contributions to energy transfer. In the framework of the Kolmogorov theory (K41) for fluids ($\psi = v$), in fully developed turbulence, and whithin the inertial range, all the statistical properties of the fields depend only on the scale ℓ, on the mean energy dissipation rate ε, and on the viscosity ν (first Kolmogorov similarity hypothesis). Also, ε is supposed to be the common value of the injection, transfer and dissipation rates. Moreover, the dependence on the viscosity only arises at small scales, near the bottom of the inertial range. Under such assumptions, it is possible to compute, by dimensional analysis, the typical

energy transfer (or dissipation) rate (for unit mass) as $\varepsilon \sim \delta v_\ell^2/t_\ell$. The time t_ℓ associated to the scale ℓ is the typical time needed for the energy to be transfered on a smaller scale. By dimensional analysis, $t_\ell \sim \ell/\delta v_\ell$, so that a scaling law for the field increments can be obtained (Kolmogorov's law):

$$\delta v_\ell \sim \varepsilon^{\frac{1}{3}} \ell^{\frac{1}{3}} \tag{1.36}$$

It turns out, when applying the Kolmogorov law to the integral scale ℓ_0, that $v_0 \sim \varepsilon^{\frac{1}{3}} \ell_0^{\frac{1}{3}}$. This relation can be used to eliminate the energy transfer rate from (1.36), so leading to the following scaling law for velocity:

$$\delta v_\ell \sim v_0 \left(\frac{\ell}{\ell_0} \right)^{\frac{1}{3}} . \tag{1.37}$$

Recalling the scaling law for the velocity arising from scaling analisys of NS equations (or MHD as in our case), the similarity hypothesis lead to $h = 1/3$. Note that, since from dimensional considerations the scaling of the energy transfer rate should be $\varepsilon \longrightarrow \lambda^{1-3h}\varepsilon'$, $h = 1/3$ is the only possible choice to guarantee the scaling invariance of ε, required by the similarity hypothesis.

At small scales, dissipation (viscosity) is involved. The typical time associated to dissipative effects can be obtained by dimensional analysis as: $t_\ell^{(\nu)} \sim \ell^2/\nu$. The scale at which the dissipation terms are comparable with the nonlinear trasfer terms is called *Kolmogorov scale* η, and can be simply obtained putting $t_\ell^{(\nu)} = t_\ell$, so that

$$\eta \sim \left(\frac{\nu^3}{\varepsilon} \right)^{\frac{1}{4}} \tag{1.38}$$

It is straightforward to translate the dimensional analysis results to spectra. In fact, using the wave vector $k \sim 1/\ell$, the previous scaling laws can be written in the wave vector space. In particular, it is possible to introduce the power spectrum $E(k) \sim \delta v_\ell^2/k$, so that from the similarity hypothesis the spectrum has a power-law behavior within the inertial range

$$E(k) \sim \varepsilon^{\frac{2}{3}} k^{-\frac{5}{3}} . \tag{1.39}$$

The power law spectrum (1.39) is whidely observed in experimental data, and is called the *Kolmogorov spectrum* (see Figure 1.4). Note that in terms

of the generic scaling exponent h, the spectral index is $\alpha = 1 - 2h$, so that the choice $h = 1/3$ leads to the *Kolmogorov spectrum.*

1.3.3 Alfvén effect: the Kraichnan spectrum

When performing dimensional analysis of plasma turbulence, it turns out that the *Alfvén effect*, that is the presence of small scales fluctuations leaving apart along the large-scale magnetic field, modify the interactions between structures. Under the same assumptions as for fluid turbulence, we can compute by dimensional analysis the typical energy flux between scales:

$$\Pi_\ell^\pm \sim \frac{|\delta z^\pm(\ell)|^2}{t_\ell^\pm}$$

t_ℓ being the typical duration of the energy transfer. Now, as can be seen looking at equations (1.16), the Alfvénic fluctuations propagate in opposite direction along the magnetic field lines, so that the interacting structures are set apart in a time $t_A \sim \ell/c_A$, so modifying the actual interaction time. If the (non linear) eddy turnover time is $t_{NL}^\pm \sim \ell/\delta z_\ell^\mp$, then the interaction time results

$$t_\ell^\pm \sim \frac{(t_{NL}^\pm)^2}{t_A^\pm} \sim \frac{\ell c_A}{\delta v^2} \tag{1.40}$$

obtained by considering the number of non linear interactions occurring during a Alfvén time, $t_{NL}^\pm/t_A^\pm$, and considering similar scaling behavior between the Elsässer fields and the velocity, $\delta \boldsymbol{z}^+ \sim \delta \boldsymbol{z}^- \sim \delta \boldsymbol{v}$. The energy flux, corresponding to the energy transfer rate $\varepsilon^\pm$, can thus be written as:

$$\Pi_\ell^\pm \sim \varepsilon^\pm \sim \frac{\delta v^4}{\ell c_A} \tag{1.41}$$

so that the scaling law for the velocity (or magnetic field, or Elsässer fields) is modified by the Alfvén effect

$$\delta v_\ell \sim v_0 \left(\frac{\ell}{\ell_0}\right)^{\frac{1}{4}} . \tag{1.42}$$

that is $h = 1/4$. The spectrum is then also modifyed,

$$E(k) \sim c_A^{\frac{1}{2}} \varepsilon^{\frac{1}{2}} k^{-\frac{3}{2}} . \tag{1.43}$$

The power law spectrum with Alfvénic effect has spectral index $\alpha = -3/2$ and is called *Kraichnan spectrum.*

1.3.4 The structure functions scaling laws

Given the Kolmogorov and Kraichnan scaling laws for fields increments (1.37) and (1.42), it is straightforward to compute the scaling law for the longitudinal structure functions from (1.28):

$$S_\ell^{(p)} = \langle \delta\psi_\ell^p \rangle \sim \ell^{\frac{p}{m}} \,, \tag{1.44}$$

where $m = 4$ if Alfvén effect decorrelates the interacting structures, and $m = 3$ if this effect is negligible. The scaling exponent of the structure functions is then a linear function of the order p, that is $\zeta_p = p/m$.

The scaling (1.44) implies the power law scaling of the second order moment, *i. e.* the standard deviation: $\sigma \sim \ell^{\frac{2}{m}}$. If the field differences $\delta\psi_\ell$ have Gaussian distribution, from the expression (1.26) the linear scaling of the structure functions is then obtained:

$$\langle \delta\psi_\ell^{2p} \rangle \sim \ell^{\frac{2p}{m}} \,.$$

In other words, the Kolmogorov and Kraichnan scalings for the field increments require Gaussian PDFs.

1.4 Intermittency

1.4.1 The problem of intermittency in turbulence

Except for the $-5/3$ spectrum which is observed everywhere in turbulence, the linear behavior of the structure functions scaling exponent with the moment order, and the gaussianity of the PDFs of increments, representing the Kolmogorov scaling, are not observed in experimental data. The K41 theory is thus just the base for turbulence studies, and includes the main fundaments, which however need further developement in the approach to turbulence (Frisch, 1995). As far as the experimental analysis was dealing with spectral analysis, the K41 theory worked well, because only the second order moment behavior was investigated. But when the more and more accurate experimental techniques permitted the investigation of higher moments, the need for a different interpretation arised. The most discussed point, has

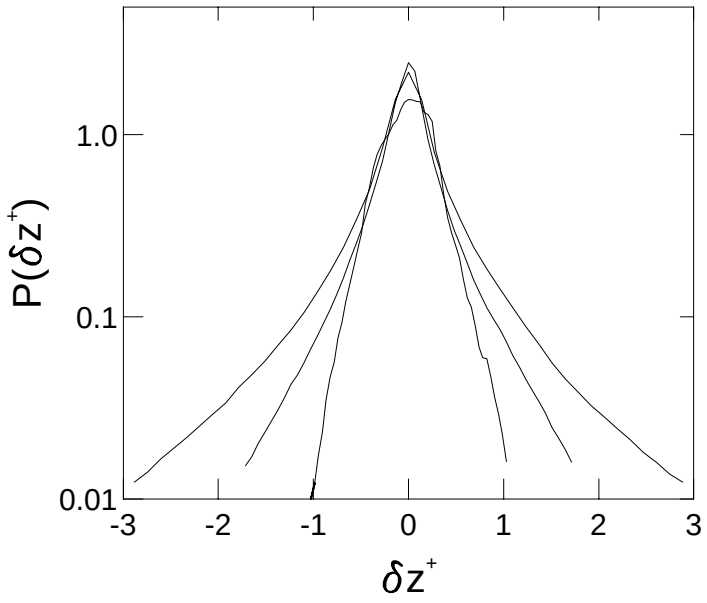

Figure 1.5: The PDFs of fields increments change shape with the scale.

been the uniform distribution of the energy transfer rate along the cascade, supposed by the K41 model (Landau & Lifshitz, 1987). Experimental results show that for fully developed turbulence, in most of the cases the shape of the field increments PDFs changes with the scale. The large scale PDFs are generally nearly Gaussians, but as the scale decreases the tails of the PDFs become higher and higher (see Figure 1.5). As a consequence, the moments, represented by the structure functions, scale in a different way, and this is visible by looking at their scaling exponents, which differ from the K41 prediction $\zeta_p = p/3$. This peculiar behavior is due to the fact that large values of the fields increments are present, and with higher probability than in a Gaussian statistics. In other words, the signal is characterised by the presence of strong eddies in some regions of space. This is why the field fluctuations are a *intermittent* signal. In general, this kind of signals are not purely self-similar.

In Figure 1.6 an example of *self-similar* signal is presented. This kind of signal displays the same statistical properties independently on the scale at which is observed. Moreover, it is similar for each region we observe. The K41 theory would lead to such a signal, for which the PDF shape would not change with the scale. On the contrary, Figure 1.7 shows a simple example of intermittent signal: the *devil staircase*, characterised by "active" zones alternated with flat regions. That is, the self-similarity of the signal in this last case depends on the position. To understand the concept of intermittency in turbulent fields, the picture of the Richardson cascade, presented to introduce turbulence, can be modified. One of the main points on which the Kolmogorov K41 theory was based is that the non linear cascade is controlled by the mean energy transfer rate ε. The actual spatial distribution of ε does not come into play at that level, the idea of universality implied by the model suggesting a uniform distribution. In the intermittent case, however, we should restate that only the *global* mean value of the energy transfer rate is constant through the cascade, while its local value can be a (stochastic) fluctuating function, presenting bursty and quite zones alteratively. Moreover, the presence of strong activity regions is scale-dependent, as can be visualized in Figure 1.8. This modified Richardson cascade picture shows the concentration of active structures on definite positions of the space, and such concentration become more and more evident as the scale decreases. Figure 1.9 shows an example of real intermittent data. The four panels represent the longitudinal velocity differences computed from solar wind data for four different values of the scale. The bottom panel is the large scale case, and the signal appears self similar. As the scale decreases, that is for the upper panels, the signal is more and more intermittent, with localization of active regions which is stronger as the scale decreases.

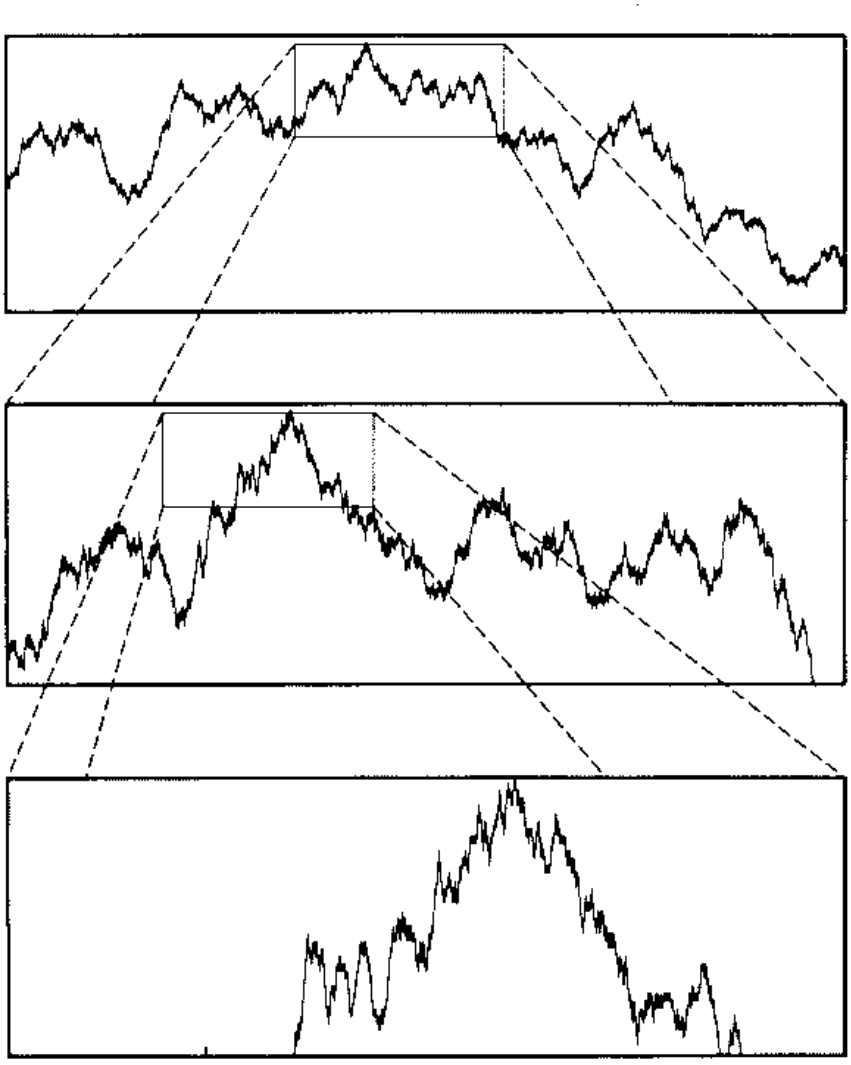

Figure 1.6: An example of self-similar signal: the brownian motion. The signal shows the same statistical properties everywhere and at all scales. The zoomed segments of signal repeat the large scale behavior in all positions (from Frisch, 1995).

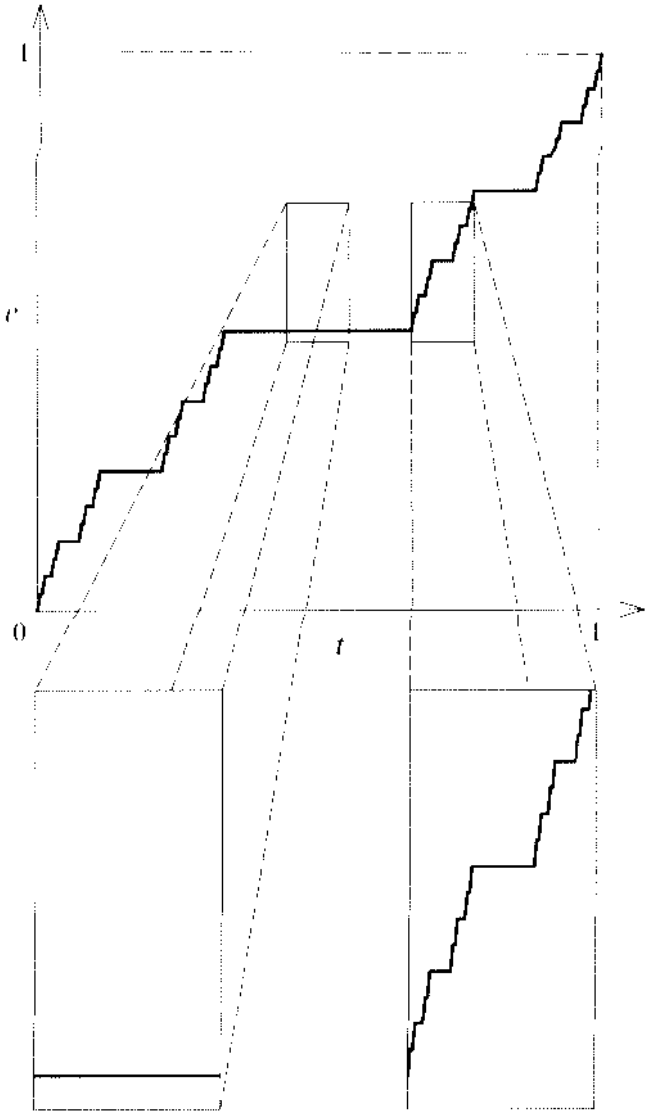

Figure 1.7: The devil staircase: an intermittent signal. The statistical properties of the signal change when we look at different scales, in different positions. The zoomed fragments of signal can be active or flat, depending on the position, and are in general different from the large scale (whole signal), which inculdes both (from Frisch, 1995).

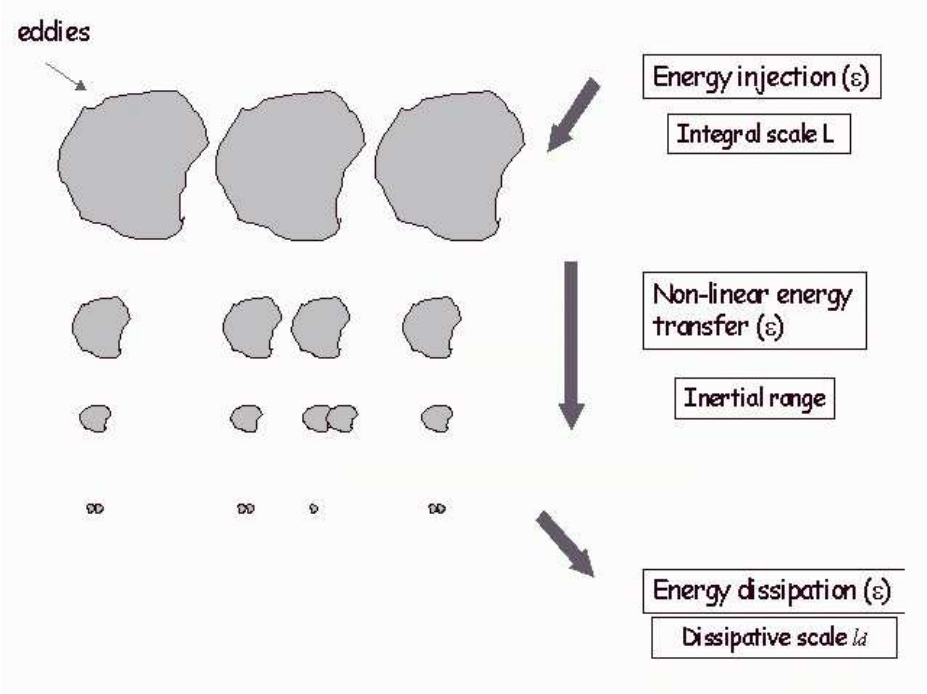

Figure 1.8: A schematic picture of the intermittent Richardson cascade. The local differences of transfer of energy are represented by concentration of active structures ir regions of the space. At the dissipative scales, the dissipation field is bursty and intermittent.

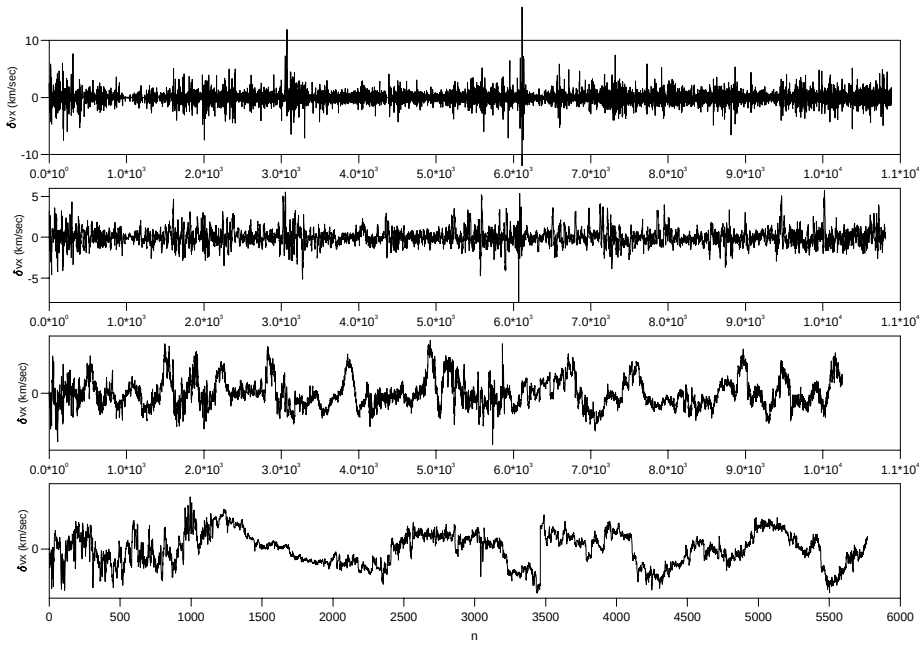

Figure 1.9: The longitudinal velocity increments in the solar wind for four different values of the scale (bottom, large scale; top, small scale).

Chapter 2

Description of the data

2.1 The solar wind data

2.1.1 The solar wind

Solar wind is a continuous flow of charged particles, mainly electrons and protons, departing from the sun into the heliosphere. Since the 50's, the solar wind origin has been located in the atmospheric regions of the sun, where it is accelerated, because of the high temperature, toward the external space in order to get hydrostatic equilibrium (Figure 2.1). The plasma particle are expelled in radial direction, their velocity increasing up to a saturation far away from the sun. Because of such acceleration, the solar wind becomes supersonic very close to the sun (*i. e.* near some solar radii), and then superalfvénic. Typical values of the solar wind speed near 1 AU are in fact about 500 Km/sec, while the Alfvén speed at the same distance from the sun is about 30 Km/sec. The solar wind plasma has $\beta \sim 1$, so that the magnetic and kinetic pressure effects are of the same order. The solar magnetic field is carried out into the heliosphere by the solar wind, because of its *frozen in* condition (see for example Akhiezer, 1975). The solar rotation is then responsible for the large scale structure of the Interplanetary Magnetic Field (IMF), which is a sort of *Archimede's spyral* (Hundhausen, 1972; see Figure 2.2 for a representation). Because of this peculiar shape, the large scale IMF near the earth orbit (1 AU) forms with the sun-earth direction an angle of about 45°.

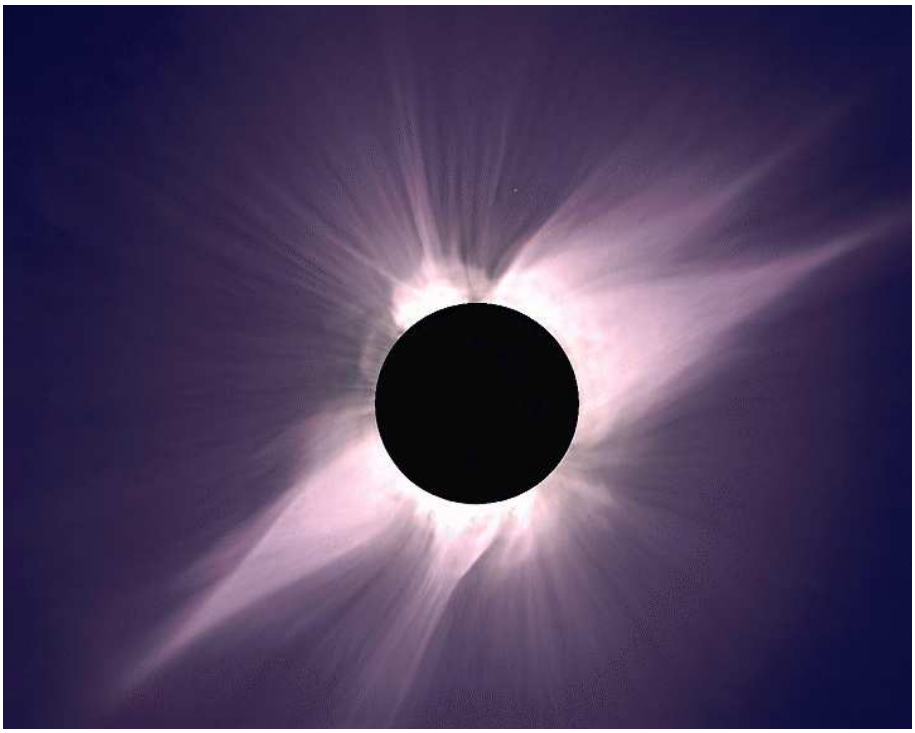

Figure 2.1: The sun during the solar eclypse occurred in 1991. The solar corona is visible and the origin of the solar wind is clearly evidenced.

Figure 2.2: A picture of the Archimede's spyral of the interplanetary magnetic field, centered on the sun. The orbits of inner planets and Jupiter are also shown.

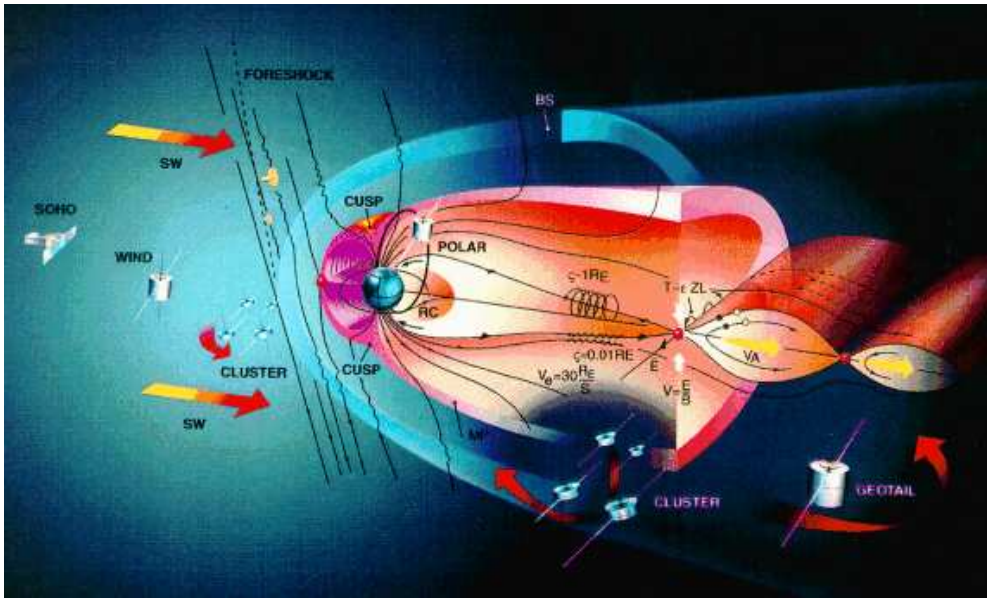

Figure 2.3: The Earth magnetosphere and the location of some of the spacecrafts currently involved in measurement campaigns.

2.1.2 Large scale properties of solar wind

The solar wind is the most important plasma laboratory present in nature. Since the beginning of the space exploration, some spacecraft have been used to collect *in situ* measurements of solar wind fields and parameters (see for example Hundhausen, 1972; Tu & Marsch, 1995). Figure 2.3 shows some of the missions currently at work. Table 1.1 reports typical values of main plasma parameters in the solar wind. Figure 2.4 shows measurements of many parameters of the solar wind between $0.3AU$ and $1AU$, as collected by the spacecraft Helios II. The upper plot represents the velocity of the wind. It is possible to distinguish portions of wind which are alternatively fast and slow. This is a peculiar situation in the solar wind as seen on the ecliptic plane, and it is related to the presence of two types of wind, namely fast solar wind and slow solar wind. The existence of two types of wind could be due to the different topology of the solar atmosphere from which they are emitted. In fact, fast wind seems to blow mainly from regions of the solar surface in correspondence with the coronal holes. In that zones,

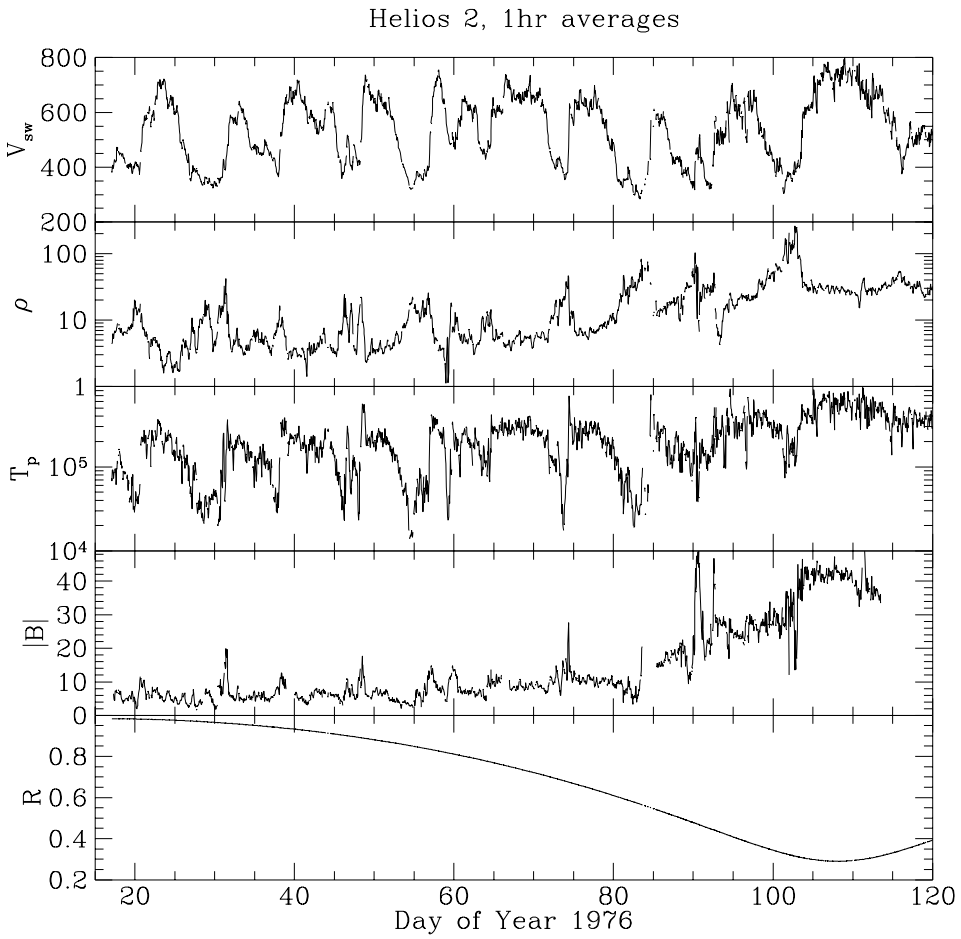

Figure 2.4: Velocity, mass density, temperature and magnetic field of solar wind, as measured by Helios II at heliocentric distance from $0.3AU$ e $1AU$, as shown in the bottom plot.

the magnetic field lines are "open" and the plasma is emitted with higher velocity. In corrispondence with active regions of the solar surface where magnetic loops are present, the solar wind is emitted with slower velocity, and is thus slow wind. The spatial distribution of the coronal holes is quite stable, but is tuned by the solar activity. In corrispondence with the polar regions of the sun, large and stable coronal holes are present, due to the dipolar form of the solar magnetic field. As the latitude decreases, more and more closed mgnetic lines regions are present, even if smaller coronal holes are distributed on all the solar surface. During the low solar activity periods the number of closed magnetic structures decreases, so that a large portion of the sun is covered by coronal holes. In these conditions, most of the wind is fast. As the activity increases, the closed structures occupy regions which extends more and more toward the high latitudes, so reducing the fast wind origin zones. Figure 2.5 schematically shows such behavior. The large scale structure of high latitude solar wind is quite regular, with rather stationary velocity and magnetic field, the latter describing the Parker spyral. At lower latitude the solar wind structure is more complicate. Because of the presence of coronal holes, both fast and slow winds are alternatively emitted from the solar corona. Moreover, near the equatorial plane the polarity of the solar magnetic field changes, so that at interface between positive and negative magnetic sectors a thin neutral current sheet is estabilished. Because of solar rotation, the current sheet is ondulated, like a "ballerina skirt" , so that the equatorial plane is crossed again and again by the current sheet, revealing alternate positive and negative magnetic field regions, as well as fast and slow speed streams. The solar wind is a turbulent system. Both the high velocity (supersonic and superalfvénic, with shocks and waves, and with very high Reynolds number, approximatively of the order $Re \sim 10^9$) and the turbulence of the emetting regions (solar surface and corona) are responsible for higly developed turbulence in the solar wind.

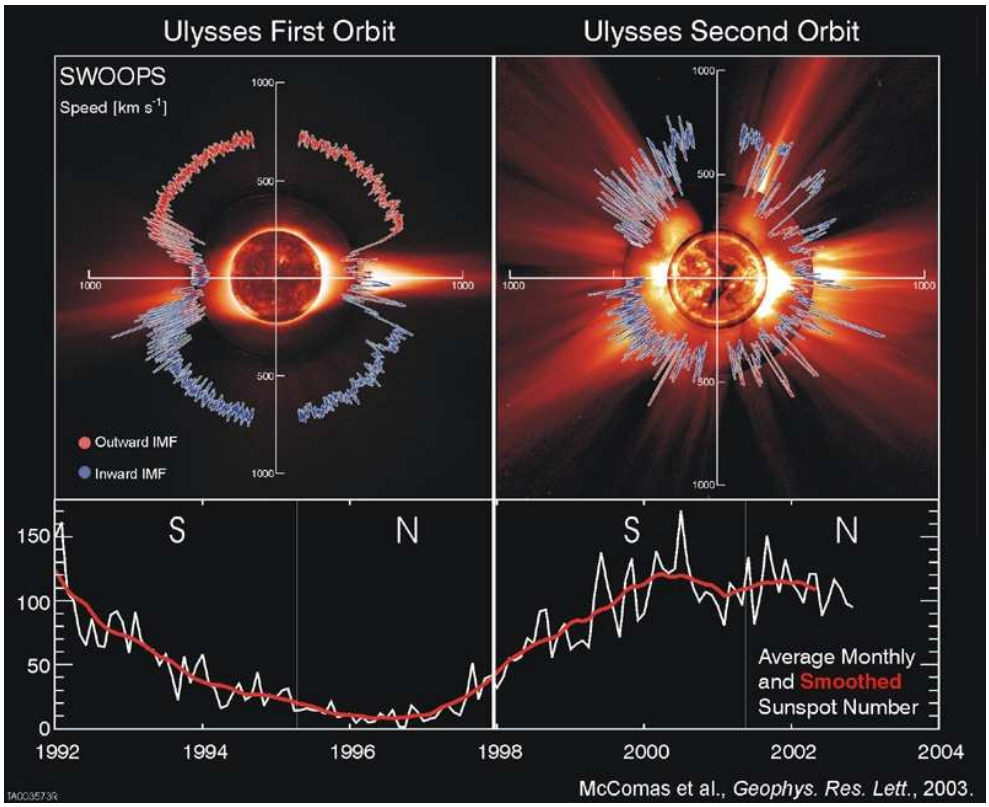

Figure 2.5: A composed picture showing the X-ray emission of the sun, and the latitude dependence of velocity and magnetic field. In the left panel (low solar activity) It is evident that wind velocity is high at high latitudes, where coronal holes are visible.

2.2 Exploring the heliosphere

2.2.1 Space missions

Since the beginning of the space age, several tens of spacecraft (see Fig. 2.6) have explored the heliosphere at virtually all latitudes up to the outskirts of the solar system, and returned a host of data. Most space probes lie close to the ecliptic plane that is the plane of the Earth's orbit around the Sun. The reason is that a spacecraft leaving the Earth starts with a velocity vector equal to the Earth's orbital velocity plus that provided by the launcher; since the Earths velocity is about 30 km/s and lies in the ecliptic plane, one must give to the spacecraft a velocity perpendicular to the ecliptic of at least this amount to put it into an orbit angled far from this plane; this is outside the capabilities of existing rocket technology (Fig. 2.7). As a result, there tens of space probes exploring the solar wind near the ecliptic. Particles and fields are intimately coupled in solar wind plasma, so that in order to explore them, space probes carry at least a particle detector, a magnetometer and an electric antenna measuring waves, in addition to power and communication resources and to the necessary software; most spacecraft generally carry many other instruments.

2.2.2 The spacecraft Ulysses

When the idea of an out-of-ecliptic mission arose, nobody knew how to realise it, and only in the 1970s did the idea appear technically feasible. The American and European Space Agencies then proposed a joint package of two spacecraft that were to be launched in 1983. But in the early 1980s, the National Aeronautical and Space Administration (NASA) decided to cancel the US spacecraft because of financial and technical difficulties. The project was reduced to a single spacecraft, to be built by the European Space Agency (ESA), launched by NASA with the Space Shuttle, and equipped with European and American instruments. This spascecraft was named *Ulysses* (a picture is shown in Figure 2.8) because its mission, to explore the heliospehere at high latitudes where no probe had been ever sent, was reminiscent of

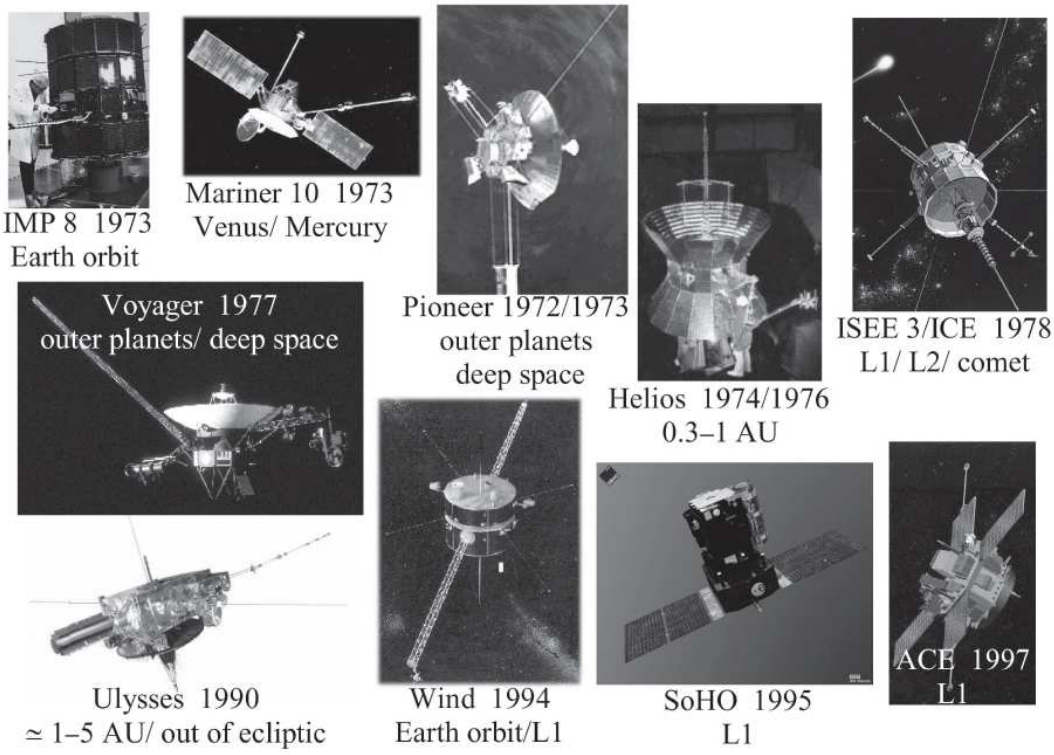

Figure 2.6: Some spacecraft that have explored the solar wind (Images by ESA and NASA)

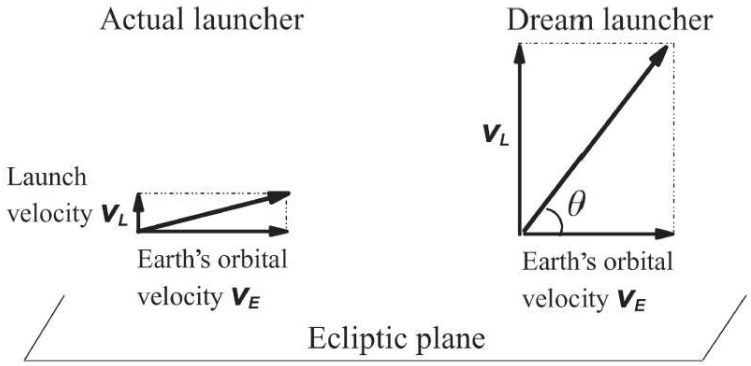

Figure 2.7: The difficulty of sending a spacecraft outside the ecliptic: because the Earth speed V_E is much greater than the launch speed V_L , the spacecraft velocity $V_L + V_E$ in the solar frame makes a very small angle to the ecliptic (adapted from Meyer-Vernet, 2007).

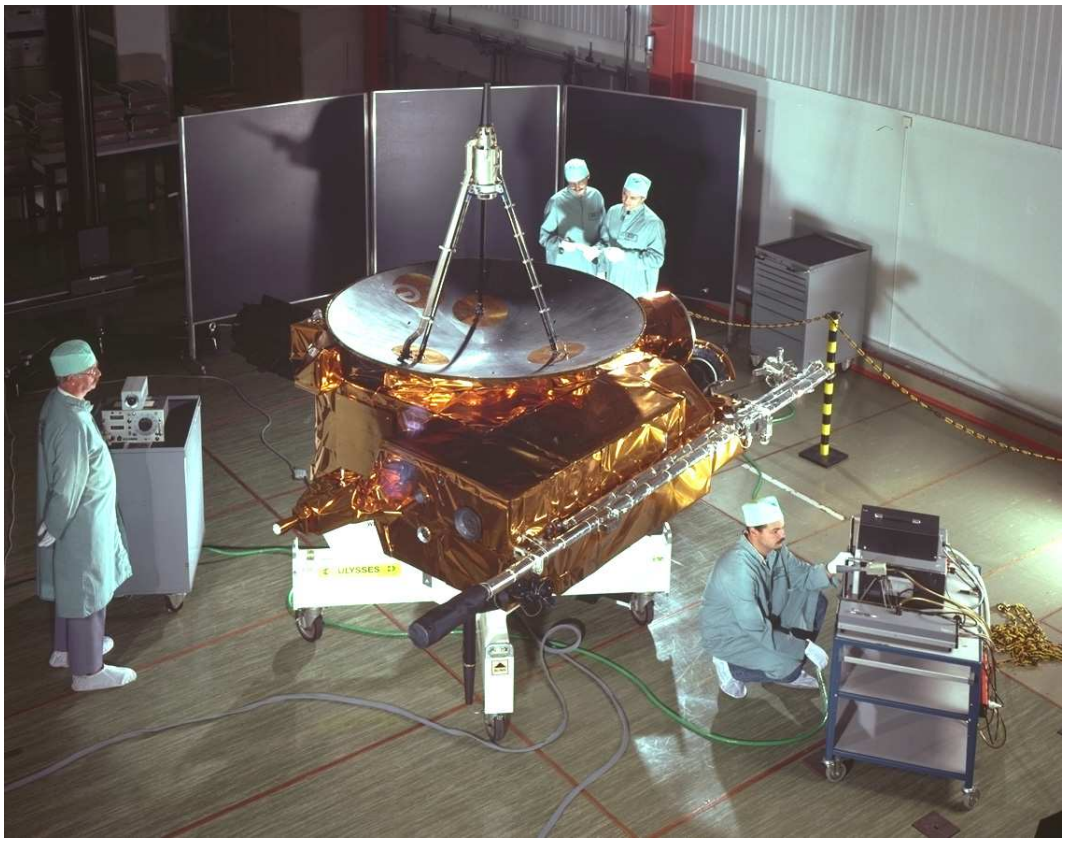

Figure 2.8: The spacecraft Ulysses in the ESA laborartory.

the journey of the mythical Greek warrior. The launch of Ulysses took place at last in October 1990 close to solar activity maximum. In 1991 the probe travelled in the ecliptic towards Jupiter. In February 1992 it swung around Jupiter - using the gravity assist of that planet - into an elliptic orbit inclined by 80° to the ecliptic (Fig. 2.9). It then travelled into the Sun's southern hemisphere, passed over the south polar region in late 1994, crossed the ecliptic plane at 1.3 AU from the Sun, and passed over the north polar region in 1995 near solar activity minimum. The second orbit took it over the polar regions once more in 2000 2001, this time near solar activity maximum. A third orbit tooke it again over the polar regions in 2007 (near solar activity minimum) and after 18.6 years in space, defying several earlier expectations of its demise, Ulysses finally switched off its transmitter on 30 June 2009.

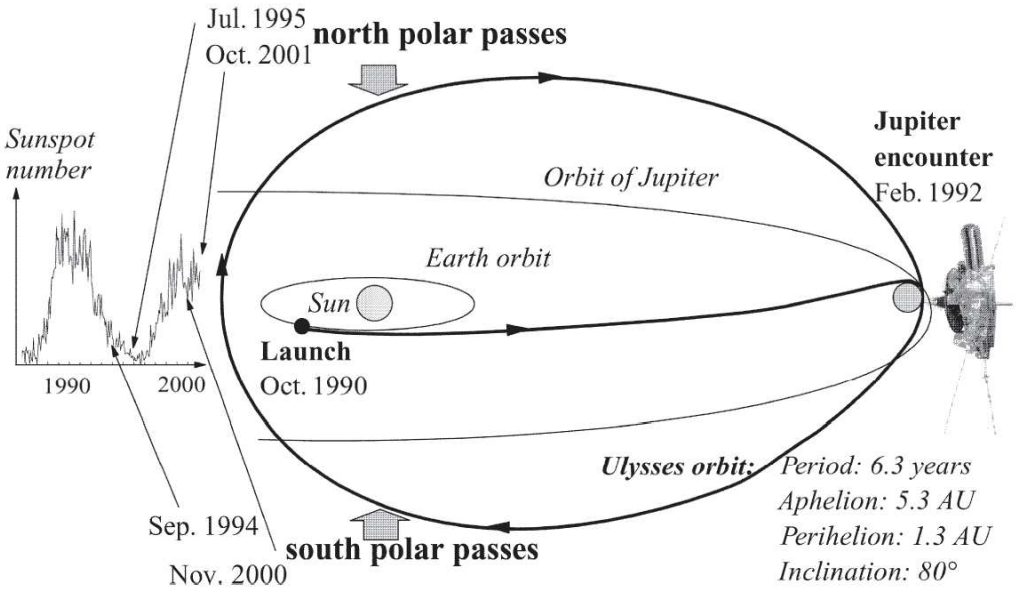

Figure 2.9: Sketch of Ulysses trajectory. The dates of the first two passages over the solar poles are indicated on the left, along with solar activity. The orbital period is such that the fast pole-to-pole transits, covered in less than a year on the perihelion side, take place alternatively near sunspot minimum and maximum (adapted from Meyer-Vernet, 2007).

2.2.3 The Ulysses dataset

The Ulysses's orbit is especially suitable for studying the heliosphere. The orbital period is nearly half a solar activity cycle, and the pole-to-pole transit near perihelion takes less than a year a time-span during which solar activity and distance do not change much (see Fig 2.10). Hence at each passage along this part of the orbit, which take place alternately near solar activity minimum and maximum, Ulysses measures how the solar wind varies with heliocentric latitude, other parameters being roughly constant. On the other hand, the distance, latitude and solar activity vary simultaneously during the aphelion phase, when the spacecraft is moving less rapidly.

As clearly visible from Figure 2.10, the Ulysses data include regions of both fast and slow wind. In this work we analyse solar wind velocity, magnetic and density field measured during the first passage of the spacecraft over the north solar pole. All the measurements are referred to a RTN reference frame (Fig. 2.11), where R (radial) indicates the sun-spacecraft direction, centered on the spacecraft and pointing out of the sun, N (normal) lies in the plane containing the radial direction and the sun rotation axis, while T (tangential) completes the right-handed reference frame. The velocity and density measurements have been performed using a top-hat electrostatic analyzer, while the magnetic field has been measured using a flux gate triaxial magnetometer. This two instruments recording data at very different time resolutions. The sampling time of the plasma data (i.e. velocity, Temperature and density), provided by INAF ("Istituto di Fisica dello Spazio Interplanetario, Roma-Italy), is around 8 minute whereas the one of magnetic field data is of 0.1 seconds (sampling frequency $\sim$ 10 Hz). In order to have uniform time series we reduced the temporal resolution of the magnetic field data in order to obtain a unique sampling time $\Delta T = 482$ seconds ($\sim$ 8 minutes). This operation implies the averaging of the magnetic field components and a resynchronization of all fields involved in our study. We also made a careful treatment of the bad data that was present in almost the 10% of the whole signals. This preliminary work on data had been necessary because we performed high order statistical analysis that are very sensitive to the "quality"

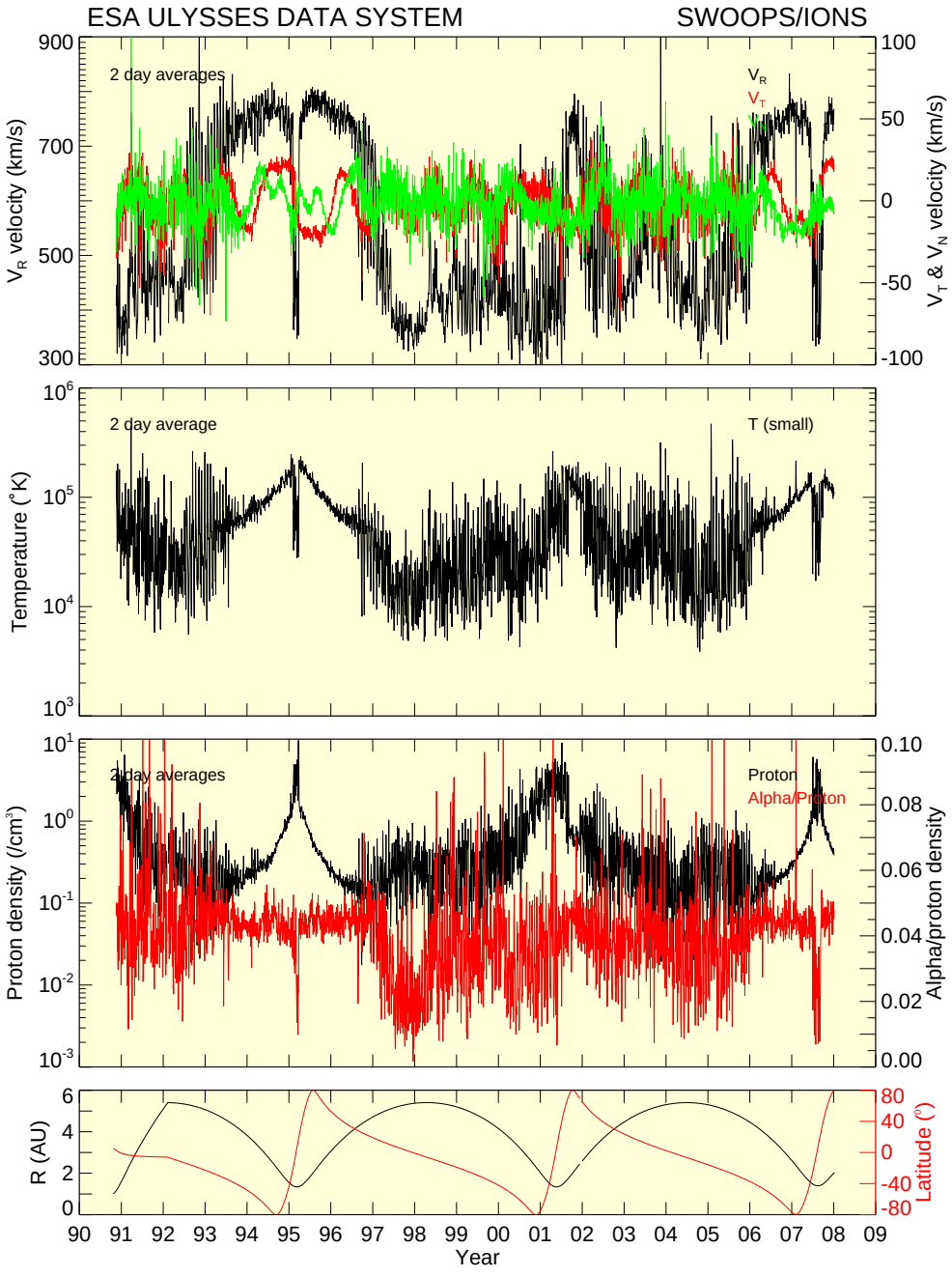

Figure 2.10: Velocity, mass density and temperature as measured by Ulysses during its three orbits around the Sun from 1990 to 2008.

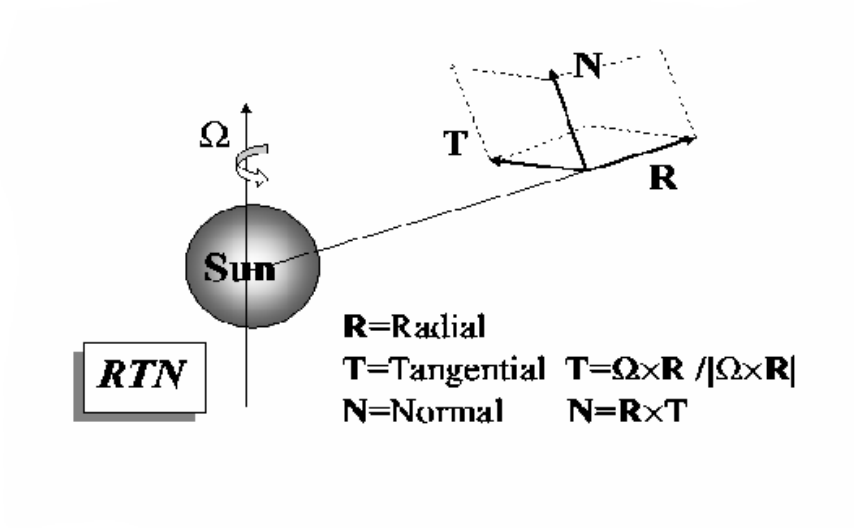

Figure 2.11: The RTN reference frame shown in the configuration used for Ulysses velocity and magnetic field data

of data input. In Figures 2.12 and 2.13 we can observe some samples of the data for both velocity and magnetic field in fast and slow streams.

2.3 The Taylor hypothesis

The experimental data, as for example fields measured with probes, are usually recorded in the time domain, as time series. Conversely, the numerical data can be spatial representation of the fields, often evolving with time, so that the measurements are in the spatial domain. Moreover, turbulence theories very often deal with spatial distribution of structures, assuming stationarity. In turbulence, the *Taylor hypothesis* provides a way to use time series to describe spatial systems (Taylor, 1938). Consider a (unidimensional) flow, moving with velocity $v(x,t)$, measured in the laboratory frame, and let $U = \langle v(x,t) \rangle_t$ be its average velocity. If $u(x,t)$ is the velocity measured in the reference frame comoving with the flow (with velocity U), then

$$v(x,t) = u(x - Ut, t) + U \tag{2.1}$$

We can define the *turbulence intensity* as $I_T = \langle u^2 \rangle^{1/2}/U$, the numerator of previous equation being the variance of the velocity in the comoving frame. Given a position $x = x_0$, when $I_T \ll 1$, then in the right hand side of equation (2.1) the time vatiation of $u(t, x_0 - Ut)$ is mainly due to the evolution of $x_0 - Ut$. In fact, the time variations of u with t are negligible with respect to that term, because the variance of u is small compared to U.

In other words, the time variations of v are determined by the spatial structure of the flow. In experimental measurements, this simply means that the flow bulk velocity is higher than the temporal evolution of the flow itself, so that the probe is recording, in the time domain, a "picture" of the flow, thus capturing its spatial structure. If the sampling time of the probe is ΔT, then the picture of the flow has a spatial resolution $\Delta X = U \Delta T$. When the Taylor hypothesis is verified, it is so possible to switch from the time domain to the spatial domain, and to compare analyses of different kind of data. The Taylor hypothesis have been tested to be valid in all the time series we analyse (for example, in the fast solar wind $I_T = 0.11$), so that in the following we will use both time and spatial domains, without any further comments.

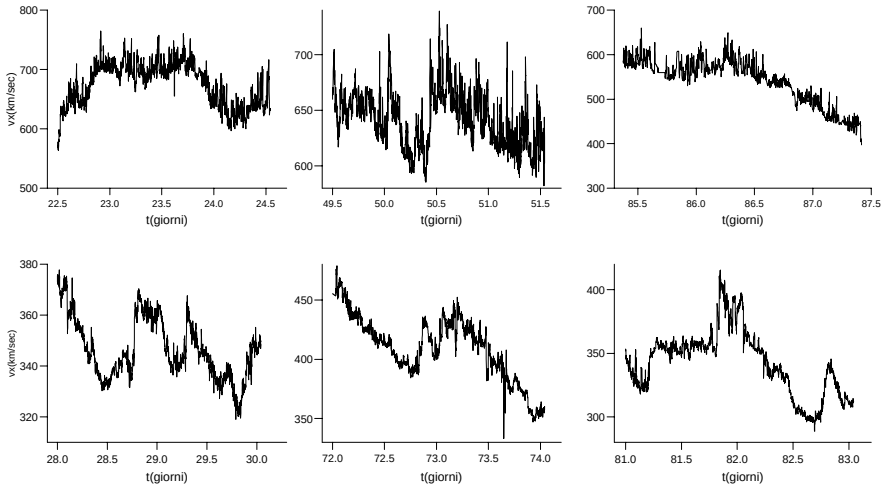

Figure 2.12: The radial component of the velocity v_x for three fast streams (upper panels) and three slow streams (bottom panels).

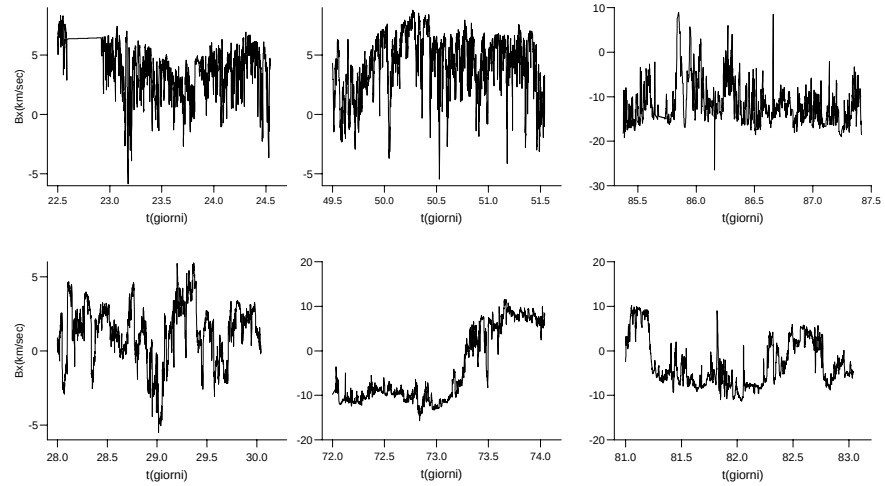

Figure 2.13: The radial component of the magnetic field b_x for the same streams presented in Figure 2.12.

Chapter 3

The inertial energy cascade in solar wind turbulence

3.1 Turbulence in solar wind

3.1.1 Spectral properties

First evidences of the presence of turbulent fluctuations in the solar wind were showed by Coleman (1968) who, using Mariner 2 magnetic and plasma observations, investigated the statistics of interplanetary fluctuations during the period August 27 – October 31, 1962, when the spacecraft orbited from 1.0 to 0.87 AU. By analyzing spectral densities, Coleman concluded that the solar wind flow is often turbulent, energy being distributed over an extraordinarily wide frequency range, from one cycle per solar rotation($\sim$ 28 days) to 0.1 Hz. The frequency spectrum, in a range of intermediate frequencies, was found to behave roughly as $f^{-1.2}$. The magnetic spectrum obtained by Coleman is shown in Figure 3.1.

Spectral properties of the interplanetary medium have been summarized by Russel (1972), who published a composite spectrum of the radial component of magnetic fluctuations as observed by Mariner 2, Mariner 4 and OGO 5 (see Figure 3.2). The frequency spectrum so obtained was divided into three main ranges: up to about 10^{-4} Hz the spectral slope was about f^{-1}; at intermediate frequencies $10^{-4} \leq f \leq 10^{-1}$ Hz a spectral slope of about $f^{-3/2}$ was found; finally, the high-frequency part of the spectrum, up to 1 Hz, was

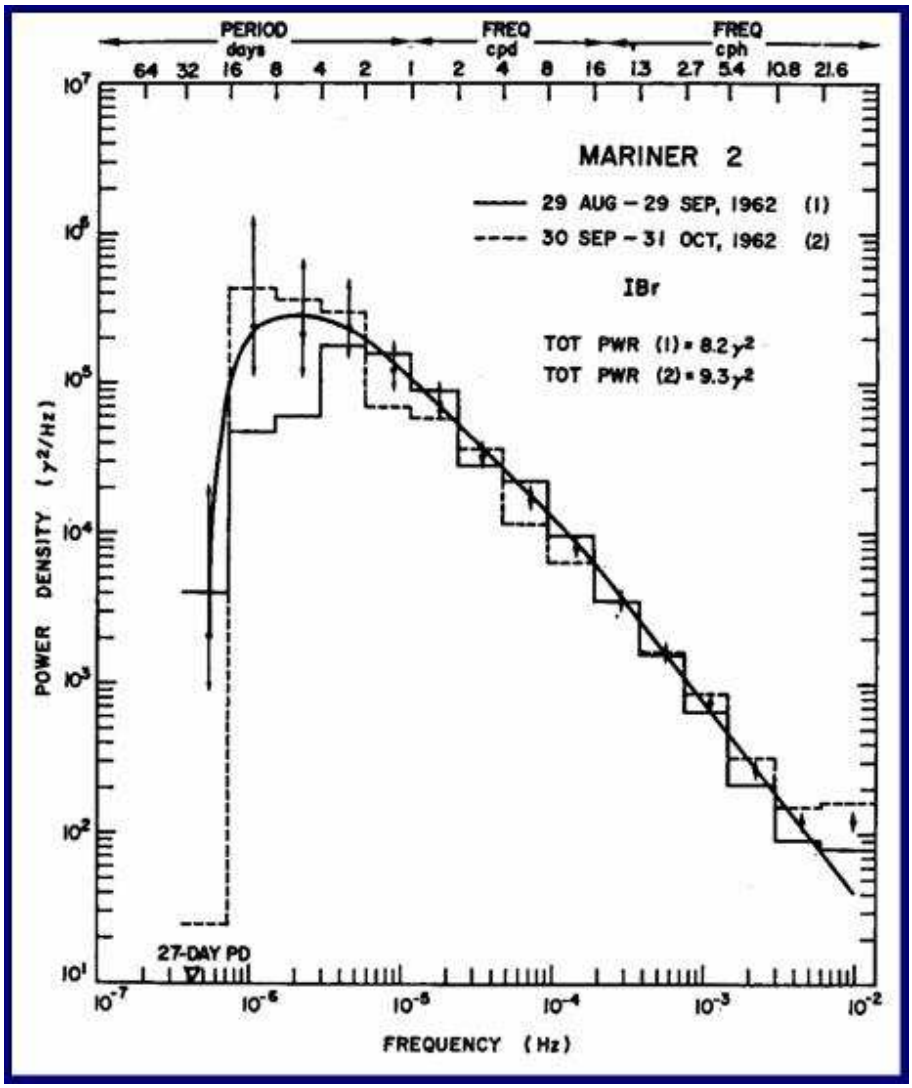

Figure 3.1: The magnetic energy spectrum as obtained by Coleman (1968).

characterized by a f^{-2} dependence. The intermediate range of frequencies recalls spectral properties similar to those introduced by Kraichnan (1965) in the framework of MHD turbulence. It is worth reporting that scatter plots of the values of the spectral index of the intermediate region do not allow to distinguish between a Kolmogorov spectrum $f^{-5/3}$ and a Kraichnan spectrum $f^{-3/2}$ (Veltri, 1980). To be precise, it is worth remarking that there are no convincing arguments to identify as *inertial range* the intermediate range of frequencies where the observed spectral properties are typical of fully developed turbulence. From a theoretical point of view, here the association "intermediate range" $\simeq$ "inertial range" is somewhat arbitrary as we will see later. Then, as far as the solar wind turbulence is concerned it is not so useful to discuss whether or not solar wind developed turbulence can be represented by $\sim f^{-5/3}$ or $f^{-3/2}$, since observations showed that the slope is usually around $f^{-1.6}$ (Bavassano, 1982a; Tu and Marsh, 1995a) which, irony of fate, is just between the two cited values. The Helios 2 spacecraft gave for the first time the unique opportunity to study the radial evolution of turbulent fluctuations in the solar wind within the inner heliosphere. Most of the theoretical studies which aim to understand the physical mechanism at the base of this evolution originate from these observations (Bavassano, 1982b; Denskat and Neubauer, 1983). In Figure 3.3 are re-proposed similar observations taken by Helios 2 during its primary mission to the Sun. These power density spectra were obtained from the trace of the spectral matrix of magnetic field fluctuations, and belong to the same solar wind stream observed by Helios 2 on day 49, at a heliocentric distance of 0.9 AU, on day 75 at 0.7 AU and, finally, on day 104 at 0.3 AU. All the spectra are characterized by two distinct spectral slopes: about -1 within low frequencies and about a Kolmogorov like spectrum at higher frequencies. These two regimes are clearly separated by a knee in the spectrum often referred to as "frequency break". As the wind expands, the frequency break moves to lower and lower frequencies so that larger and larger scales become part of the Kolmogorov-like turbulence spectrum, i.e., of what we will indicate as "inertial range" . Thus, the power spectrum of solar wind fluctuations is not solely function of frequency f but it also depends on heliocentric distance r.

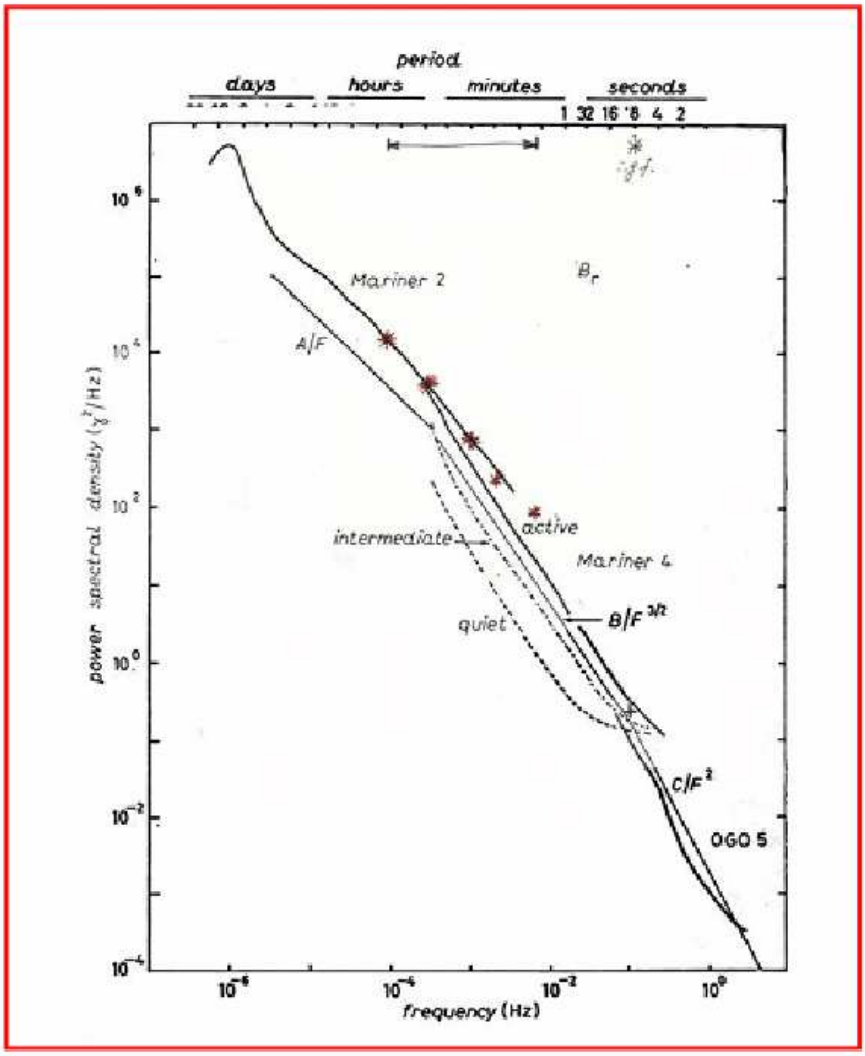

Figure 3.2: A composite figure of the magnetic spectrum obtained by Russel (1972)

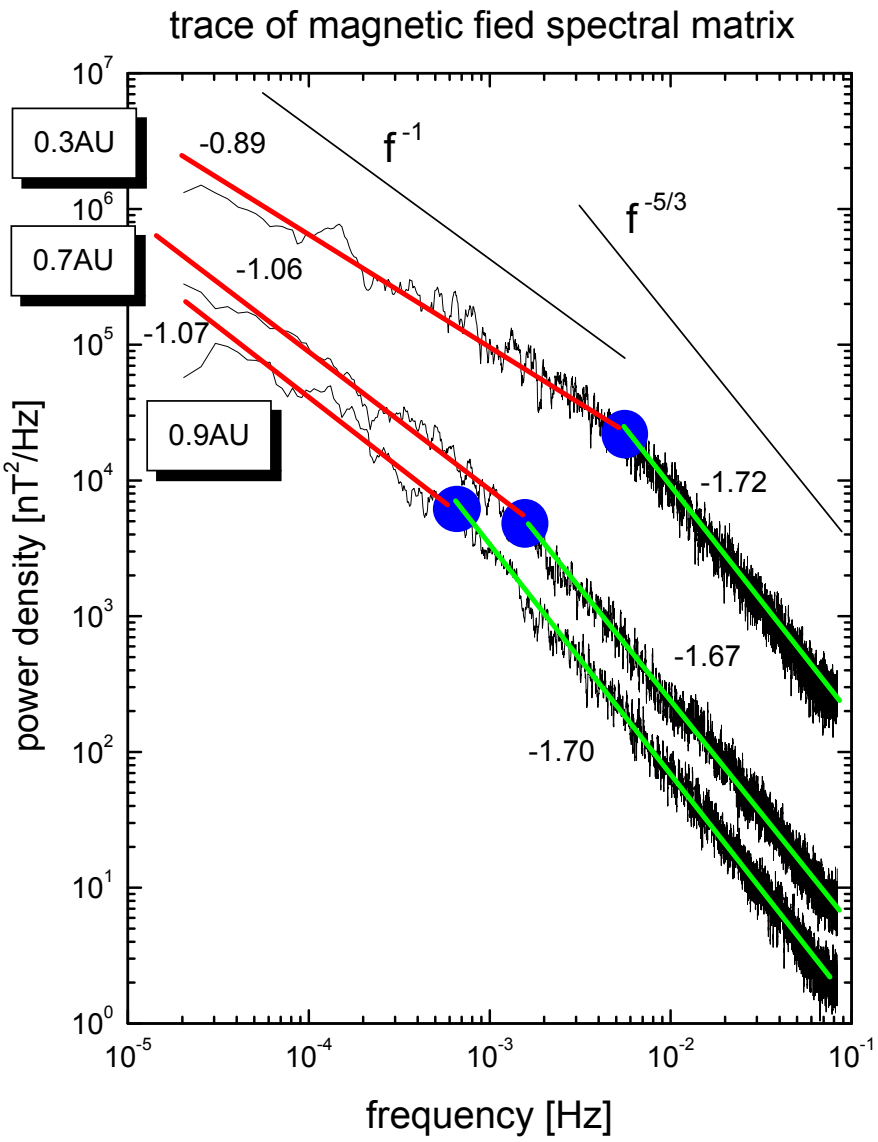

Figure 3.3: Power density spectra of magnetic field fluctuations observed by Helios 2 between 0.3 and 1 AU during the first mission to the Sun in 1976. The spectral break (blue dot) shown by each spectrum, moves to lower and lower frequency as the heliocentric distance increases.

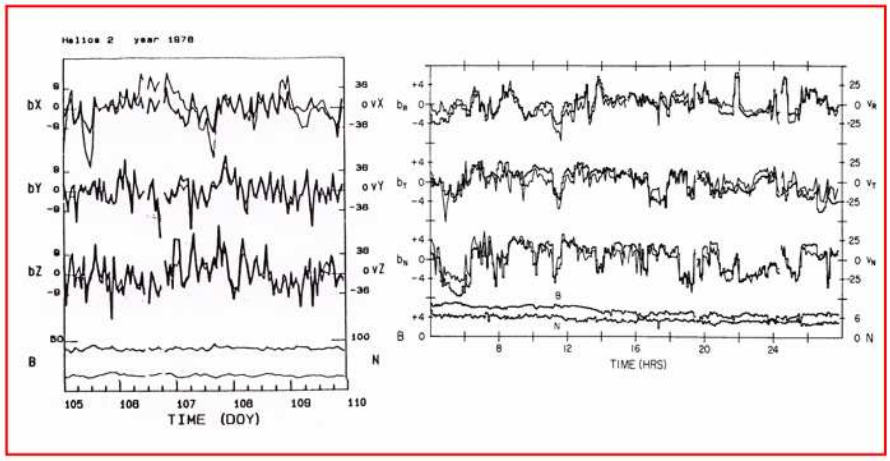

Figure 3.4: Alfvénic correlation in fast solar wind. Left panel: large scale Alfvénic fluctuations found by Bruno (1985). Right panel: small scale Alfvénic fluctuations found for the first time by Belcher (1975).

3.1.2 Alfvénic correlation

In a famous paper, Belcher and Davis Jr. (1971) showed that a strong correlation exists between velocity and magnetic field fluctuations, in the form

$$\delta \mathbf{v} \simeq \pm \frac{\delta \mathbf{B}}{\sqrt{4\pi\rho}}, \tag{3.1}$$

where the sign of the correlation is given by the $sign[-\mathbf{k} \cdot \mathbf{B_0}]$, being $\mathbf{k}$ the wave vector and $\mathbf{B_0}$ the background magnetic field vector. These authors showed that in about 25 d of data from Mariner 5, out of the 160 d of the whole mission, fluctuations were described by Equation (3.1), and the sign of the correlation was such to indicate always an outward sense of propagation of the Alfvén waves with respect to the Sun. Authors also noted that these periods mainly occur within the trailing edges of high-speed streams. Moreover, in the regions where Equation (3.1) is verified to a high degree, the magnetic field magnitude is almost constant ($B^2 \sim$ const.).

Today we know that Alfvénic correlations are ubiquitous in the fast solar wind and that these correlations are much stronger and are found at lower and lower frequencies, as we look at shorter and shorter heliocentric distances. In the right panel of Figure 3.4 are shown the results from Belcher (1975) obtained on the basis of 5 min averages of velocity and magnetic field recorded by Mariner 5 in 1967, during its mission to Venus. On the left panel of Figure 3.4 are shown results from a similar analysis performed by Bruno et al. (1985) obtained on the basis of 1 h averages of velocity and magnetic field recorded by Helios 2 in 1976, when the s/c was at 0.29 AU from the Sun. These last authors found that, in their case, Alfvénic correlations extended to time periods as low as 15 h in the s/c frame at 0.29 AU, and to periods a factor of two smaller near the Earth's orbit. Now, if we think that this long period of the fluctuations at 0.29 AU was larger than the transit time from the Sun to the s/c, this results might be the first evidence for a possible solar origin for these fluctuations, probably caused by the shuffling of the foot-points of the solar surface magnetic field.

Alfvén modes are not the only low frequency plasma fluctuations allowed by the MHD equations but they certainly are the most frequent fluctuations observed in the solar wind. The reason why other possible propagating modes like the slow sonic mode and the fast magnetosonic mode cannot easily be found, depends on the fact that these compressive modes are strongly damped in the solar wind shortly after they are generated. On the contrary, Alfvénic fluctuations, which are difficult to be damped because of their uncompressive nature, survive much longer and dominate solar wind turbulence. Nevertheless, there are regions where Alfvénic correlations are much stronger like the trailing edge of fast streams, and regions where these correlations are weak like intervals of slow wind (Belcher 1971 and 1975). However, the degree of Alfvénic correlations unavoidably fades away with increasing heliocentric distance, although it must be reported that there are cases when the absence of strong velocity shears and compressive phenomena favor a high Alfvénic correlation up to very large distances from the Sun.

Just to give a qualitative quick example about Alfvénic correlations in fast and slow wind, we show in Figure 3.5 the speed profile for about 100 d

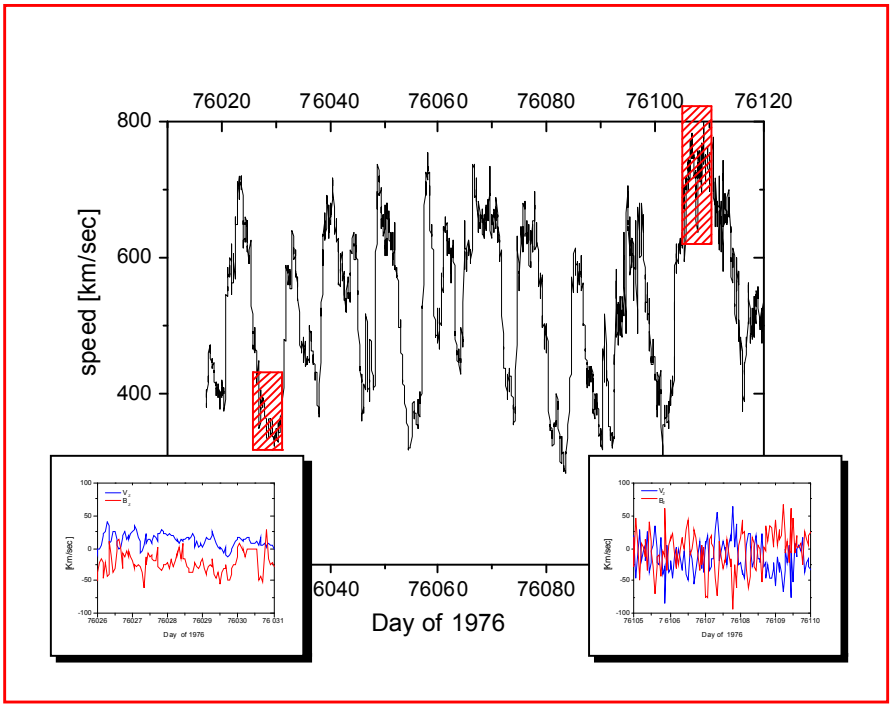

Figure 3.5: Alfvénic correlation in fast and slow wind. Notice the different degree of correlation between these two types of wind.

of 1976 as observed by Helios 2, and the traces of velocity and magnetic field Z components V_Z and B_Z (this last one expressed in Alfvén units) for two different time intervals, which have been enlarged in the two inserted small panels. The high velocity interval shows a remarkable anti-correlation which, since the mean magnetic field $\mathbf{B_0}$ is oriented away from the Sun, suggests a clear presence of outward oriented Alfvénic fluctuations given that the sign of the correlation is the $sign[-\mathbf{k} \cdot \mathbf{B_0}]$. At odds with the previous interval, the slow wind shows that the two traces are rather uncorrelated. For sake of brevity, here is omitted the plot which shows the very similar behavior for the other two components, within both fast and slow wind.

3.1.3 The Alfvénic turbulence: *an apparent paradox*

The discovery of Alfvénic correlations in the solar wind stimulated fundamental remarks by Kraichnan (1974) who, following previous theoretical works (Kraichnan, 1965 ; Iroshnikov, 1963), showed that the presence of a strong correlation between velocity and magnetic fluctuations renders non-linear transfer to small scales less efficient than for the Navier–Stokes equations, leading to a turbulent behavior which is different from that described by Kolmogorov (1941). In particular, when Equation (3.1) is exactly satisfied, non-linear interactions in MHD turbulent flows cannot exist . This fact introduces a problem in understanding the evolution of MHD turbulence as observed in the interplanetary space. Both a strong correlation between velocity and magnetic fluctuations and a well defined turbulence spectrum (Figures 3.3, 3.5) are observed, and the existence of the correlations is in contrast with the existence of a spectrum which in turbulence is due to a non-linear energy cascade. The contradiction between these observations can be immediately seen by introducing the Elsässer variables (see also section 1.1.3)

$$z^{\pm}(\mathbf{x},t) = \mathbf{v} \pm \frac{\mathbf{B}}{\sqrt{4\pi\rho}}$$

where $\mathbf{v}_i$ and $\mathbf{B}_i$ represent the velocity and magnetic field respectively, while ρ is the mass density. These quantities represent Alfvénic fluctuations propagating along the background magnetic field, in opposite directions. MHD equations can be immediately written in terms of these variables as

$$\partial_t z_i^{\pm} + \left(z_\alpha^{\mp}\partial_\alpha\right) z_i^{\pm} = -\partial_i \pi + \lambda^{\pm}\partial_\alpha^2 z_i^{+} + \lambda^{\mp}\partial_\alpha^2 z_i^{-} \tag{3.2}$$

where $\pi = P/\rho$ (P being the the total pressure), ∂_t represents time derivative while ∂_i represents derivative with respect to the spatial variable x_i.

The kinematic viscosity ν and the magnetic diffusivity μ form the dissipative coefficients $\lambda^{\pm} = (\nu \pm \mu)/2$. The second term in equations (3.2) shows that nonlinear interactions only occur between opposite sign fluctuations. Since high correlations between velocity and magnetic fluctuations imply either $z_i^{\mp} = 0$ or $z_i^{\pm} = 0$, a turbulent energy cascade should be incompatible with the disappearence of one of the alfvénic fluctuations. In a seminal paper, Dobrowolny, Mangeney and Veltri (1980), started to solve the puzzle on the existence of this apparent paradox. In presence of a strong magnetic field, nonlinear interactions are slowed down by the transport of fluctuations (Alfvén effect). The usual Kolmogorov's phenomenlogy must then be modified in favor of the Iroshnikov-Kraichnan (IK). For Dobrowolny et al. (1980) this yields to the fact that the energy transfer rates per unit mass for both pseudo-energies associated to alfvénic fluctuations must be of the same order, $\epsilon^+ \sim \epsilon^-$. More precisely, they must have the same scaling laws in the IK phenomenology (Carbone, 1993). Thus, an initial small unbalance between alfvénic fluctuations is maintained during the cascade, eventually leading to both a turbulent spectrum, and high correlations (Dobrowolny et al., 1980). This framework is referred to in the literature as *Alfvénic turbulence*. The above arguments have been criticized (Matthaeus et. Al 1982 , Grappin et Al. 1983) on the basis of the fact that, at variance with the conjecture in Dobrowolny et al. (1980), in numerical simulations the energy transfer rates are never the same.

3.2 The Yaglom law for the MHD

3.2.1 Exact relations in fluid and MHD turbulence

In a fluid system is possible to put rigorously in evidece the presence of a fully developed turbulent state , verifying the validity of a relation, obtained by A.N. Kolmogorov, between the third-order longitudinal structure function of the velocity and the energy dissipation transfer rate, namely the Kolmogorov 4/5-law. Being obtained directly from the Navier-Stokes equations this law represents *"...one of the most important result in fully developed turbulence because it is both exact and non-trivial"* (Frisch, 1995). The 4/5-law states that under the hypothesis of global homogeneity and isotropy, in the limit of infinite Reynolds number (but assuming that the turbulent flow has a finite nonzero mean dissipation energy rate ε), the third-order velocity structure function behaves linearly with ℓ

$$S_r^{(3)} = \langle (v_r)^3 \rangle = -\frac{4}{5}\epsilon r \tag{3.3}$$

The similarities of the MHD equations with the Navier-Stokes equations and the equation for the transport of the passive quantitiy by an advecting fluid, namely Yaglom law (Monin and Yaglom, 1975), suggested to derive an exact relation for the mixed third order moment of the Elsassër variables which can be considered a Yaglom law for the MHD

$$Y_r^{\pm} = \langle \Delta z_r^{\mp} |\Delta z_i^{\pm}|^2 \rangle = -\frac{4}{3}\epsilon^{\pm} r \tag{3.4}$$

Both Equations (3.3, 3.4) are theorems of the turbulence theory and can be used, or better, in a certain sense they *should be* used instead of the Kolmogorov or Kraichnan energy spectrum, to enstablish unambiguosly the presence of fully developed (fluid or plasma) turbulence in the system under study and define in the most rigorous way the corresponding inertial range

energy cascade. Since they are exact relationships derived from Navier-Stokes and MHD equations under usual hypotheses, they represent a kind of "zeroth-order" conditions on experimental and theoretical analysis of the inertial range properties of turbulence.

3.2.2 Derivation of the Yaglom law for the MHD

We derived the Yaglom law for the MHD by using an approach similar to the one used by Danaila et. al. (2001) to obtain the Kolmogorov 4/5-law for the neutral fluid case. Consider the anisotropic MHD equations (3.2) written twice for Elsässer variable $z_i^{\pm}(x_i)$ at the point x_i, and for $z_i^{\pm}(x_i + r_i)$ at the independent point $x_i' = x_i + r_i$. By substraction, we obtain an equation for the differences $\Delta z_i^{\pm} = (z_i^{\pm})' - z_i^{\pm}$ (here and in the following "primed" variables are intended as calculated on the point x_i'). Using the hypothesis of independence of points x_i' and x_i with respect to derivatives, namely $\partial_i (z_j^{\pm})' = \partial_i' z_j^{\pm} = 0$ (where ∂_i' represents derivative with respect to x_i'), we get

$$\partial_t \Delta z_i^{\pm} + z_\alpha^{\mp\prime} \partial_\alpha' \Delta z_i^{\pm} = -(\partial_i' + \partial_i)\Delta P + (\partial_\alpha^{2\prime} + \partial_\alpha^2)\left[\lambda^{\pm}\Delta z_i^{+} + \lambda^{\mp}\Delta z_i^{-}\right] \quad (3.5)$$

($\Delta P = \pi' - \pi$). By adding and substracting the term $z_\alpha^{\mp}\partial_\alpha' \Delta z_i^{\pm}$ to (3.5) we obtain

$$\begin{aligned} \partial_t \Delta z_i^{\pm} + \Delta z_\alpha^{\mp}\partial_\alpha' \Delta z_i^{\pm} \;&+\; z_\alpha^{\mp}(\partial_\alpha' + \partial_\alpha)\Delta z_i^{\pm} = -(\partial_i' + \partial_i)\Delta P + \\ &+\; (\partial_\alpha^{2\prime} + \partial_\alpha^2)\left[\lambda^{\pm}\Delta z_i^{+} + \lambda^{\mp}\Delta z_i^{-}\right] \end{aligned} \quad (3.6)$$

We are seeking for an equation for the second-order correlation tensor $\langle \Delta z_i^{\pm} \Delta z_j^{\pm} \rangle$ related to pseudo-energies. In fact, in a more general approach one should look at a mixed tensor, namely $\langle \Delta z_i^{\pm} \Delta z_j^{\mp} \rangle$, taking into account not only both pseudo-energies but also cross-helicity $\langle z_i^{+} z_j^{-} \rangle$ and $\langle z_i^{-} z_j^{+} \rangle$. However, using the DIA closure by Kraichnan, it is possible to show that these elements are

in general poorly correlated. Since we are interested in the energy cascade, we limit ourself to the most interesting equation that describes correlations about Alfvénic fluctuations of the same sign. To obtain the equations for pseudo-energies we multiply equations (3.6) by $\Delta z_j^{\pm}$, then by averaging we get

$$\begin{aligned}
\partial_t \langle \Delta z_i^{\pm} \Delta z_j^{\pm} \rangle &+ \langle \Delta z_\alpha^{\mp} \partial'_\alpha (\Delta z_i^{\pm} \Delta z_j^{\pm}) \rangle + \langle z_\alpha^{\mp} (\partial'_\alpha + \partial_\alpha)(\Delta z_i^{\pm} \Delta z_j^{\pm}) \rangle = \\
= &- \langle \Delta z_j^{\pm} (\partial'_i + \partial_i) \Delta P + \Delta z_i^{\pm} (\partial'_j + \partial_j) \Delta P \rangle + \\
&+ \lambda^{\pm} \langle \Delta z_j^{\pm} (\partial_\alpha^{2\prime} + \partial_\alpha^2) \Delta z_i^{+} \rangle + \lambda^{\pm} \langle \Delta z_i^{\pm} (\partial_\alpha^{2\prime} + \partial_\alpha^2) \Delta z_j^{+} \rangle + \\
&+ \lambda^{\mp} \langle \Delta z_j^{\pm} (\partial_\alpha^{2\prime} + \partial_\alpha^2) \Delta z_i^{-} \rangle + \lambda^{\mp} \langle \Delta z_i^{\pm} (\partial_\alpha^{2\prime} + \partial_\alpha^2) \Delta z_j^{-} \rangle \quad (3.7)
\end{aligned}$$

If we consider local homogeneity we have

$$\partial'_\alpha \equiv \frac{\partial}{\partial (x_\alpha + r_\alpha)} \simeq \frac{\partial}{\partial r_\alpha}$$

$$\partial_\alpha \equiv \frac{\partial}{\partial (x'_\alpha - r_\alpha)} \simeq -\frac{\partial}{\partial r_\alpha}$$

when applied to difference quantities, so that the nonlinear term, using incompressibility, becomes

$$\langle \Delta z_\alpha^{\mp} \partial'_\alpha (\Delta z_i^{\pm} \Delta z_j^{\pm}) \rangle = \frac{\partial}{\partial r_\alpha} \langle \Delta z_\alpha^{\mp} (\Delta z_i^{\pm} \Delta z_j^{\pm}) \rangle$$

Note that in eq. (3.2) kinematic viscosity are not assumed equal to magnetic diffusivity, and this generates a coupling between $z_i^{\pm}$ and $z_i^{\mp}$ not only in the nonlinear term but also in the dissipative term. We exclude these couplings by making here the usual symplifying assumption, that kinematic viscosity is equal to magnetic diffusivity, $\lambda^{\pm} = \lambda^{\mp} = \nu$. Then, by using the independence of derivatives with respect to both points and using the local homogeneity hypothesis, the dissipative term becomes

$$\nu\langle(\partial_\alpha^{2\prime}+\partial_\alpha^2)(\Delta z_i^\pm\Delta z_j^\pm)\rangle = 2\nu\frac{\partial^2}{\partial r_\alpha}\langle\Delta z_i^\pm\Delta z_j^\pm\rangle - \frac{4}{3}\frac{\partial}{\partial r_\alpha}(\epsilon_{ij}^\pm r_\alpha)$$

where we defined the average dissipation tensor

$$\epsilon_{ij}^\pm = \nu\langle(\partial_\alpha z_i^\pm)(\partial_\alpha z_j^\pm)\rangle \tag{3.8}$$

Using these equations in (3.7), we finally obtain the equation

$$\begin{aligned}\partial_t\langle\Delta z_i^\pm\Delta z_j^\pm\rangle \;+\; & \frac{\partial}{\partial r_\alpha}\langle\Delta z_\alpha^\mp(\Delta z_i^\pm\Delta z_j^\pm)\rangle = \\ = \; & -\Lambda_{ij}-\Pi_{ij}+2\nu\frac{\partial^2}{\partial r_\alpha^2}\langle\Delta z_i^\pm\Delta z_j^\pm\rangle - \frac{4}{3}\frac{\partial}{\partial r_\alpha}(\epsilon_{ij}^\pm r_\alpha)\end{aligned} \tag{3.9}$$

The first and second term on the r.h.s. of the last equation represent respectively a tensor related to large-scale inhomogeneities $\Lambda_{ij} = \langle z_\alpha^\mp(\partial'_\alpha + \partial_\alpha)(\Delta z_i^\pm\Delta z_j^\pm)\rangle$, and the tensor related to the pressure term $\Pi_{ij} = \langle\Delta z_j^\pm(\partial'_i + \partial_i)\Delta P + \Delta z_i^\pm(\partial'_j+\partial_j)\Delta P\rangle$. Equation (3.9) is an exact equation for anisotropic MHD equations that links the second-order complete tensor to the third-order mixed tensor through the average dissipation rate tensor. Using incompressibility and independence of derivatives with respect to both points, the first term on the r.h.s. can be written as $\Lambda_{ij} = (\partial'_\alpha + \partial_\alpha)\langle z_\alpha^\mp(\Delta z_i^\pm\Delta z_j^\pm)\rangle$ which vanishes for a globally homogeneous situation, because in this case $\partial_i\langle\rangle \equiv 0$. The pressure term is more complicated to be managed. Using independence of derivatives and local homogeneity we get

$$\begin{aligned}\langle\Delta z_i^\pm\partial_j\Delta P\rangle \;&=\; \langle\partial_j[\Delta z_i^\pm\Delta P] - (\partial_j z_i^\pm)\Delta P\rangle = \\ &=\; -\langle\partial'_j[\Delta z_i^\pm\Delta P]\rangle - \langle(\partial_j z_i^\pm)\Delta P\rangle\end{aligned} \tag{3.10}$$

from which

$$\Pi_{ij} = \langle \left[\partial'_j (z_i^{\pm})' - \partial_j z_i^{\pm} \right] \Delta P \rangle + \langle \left[\partial'_i (z_j^{\pm})' - \partial_i z_j^{\pm} \right] \Delta P \rangle \tag{3.11}$$

Then the diagonal terms of the tensor containing the pressure vanish. In fact summing over indices eq. (3.11) yields $[\partial'_i (z_i^{\pm})' - \partial_i z_i^{\pm}]$ which is zero for local homogeneity and incompressibility. This means that, assuming global homogeneity and incompressibility, the equation for the trace of tensor can be written as

$$\partial_t \langle |\Delta z_i^{\pm}|^2 \rangle + \frac{\partial}{\partial r_\alpha} \langle \Delta z_\alpha^{\mp} |\Delta z_i^{\pm}|^2 \rangle = 2\nu \frac{\partial^2}{\partial r_\alpha} \langle |\Delta z_i^{\pm}|^2 \rangle - \frac{4}{3} \frac{\partial}{\partial r_\alpha} (\epsilon_{ii}^{\pm} r_\alpha) \tag{3.12}$$

This expression is valid even in the anisotropic case, that is fields depends on the vector r_α. Moreover by considering only the trace, we ruled out the possibility to investigate anisotropies related to different orientations of vectors within the second-order moment. It is worthwhile to remark here that *only* the diagonal elements of the dissipation rate tensor, namely $\epsilon_{ii}^{\pm}$ are positive defined, while in general the off-diagonal elements $\epsilon_{ij}^{\pm}$ can be in principle also negative. For a stationary state the equation (3.12) can be written as the divergenceless condition of a quantity involving the third-order correlations and the dissipation rates

$$\frac{\partial}{\partial r_\alpha} \left[\langle \Delta z_\alpha^{\mp} |\Delta z_i^{\pm}|^2 \rangle - 2\nu \frac{\partial}{\partial r_\alpha} \langle |\Delta z_i^{\pm}|^2 \rangle - \frac{4}{3} (\epsilon_{ii}^{\pm} r_\alpha) \right] = 0 \tag{3.13}$$

from which we can obtain the Yaglom's relation by projecting equation (3.13) along the longitudinal $r_\alpha = r\mathbf{e}_r$ direction. This operation involves the assumption that the flow is locally isotropic, that is fields depends locally only on the separation r, so that

$$\left(\frac{2}{r} + \frac{\partial}{\partial r} \right) \left[\langle \Delta z_r^{\mp} |\Delta z_i^{\pm}|^2 \rangle - 2\nu \frac{\partial}{\partial r} \langle |\Delta z_i^{\pm}|^2 \rangle + \frac{4}{3} \epsilon_{ii}^{\pm} r \right] = 0 \tag{3.14}$$

The only solution that is compatible with the absence of singularity in the limit $r \to 0$ is

$$\langle \Delta z_r^{\mp} |\Delta z_i^{\pm}|^2 \rangle = 2\nu \frac{\partial}{\partial r} \langle |\Delta z_i^{\pm}|^2 \rangle - \frac{4}{3} \epsilon_{ii}^{\pm} r \tag{3.15}$$

which reduces to the Yaglom's law for MHD turbulence in the inertial range (Carbone et al., 2009b) when $\nu \to 0$

$$Y_r^{\pm} = \langle \Delta z_r^{\mp} |\Delta z_i^{\pm}|^2 \rangle = -\frac{4}{3} \epsilon_{ii}^{\pm} r \tag{3.16}$$

An alternative derivation of this result using correlators instead of structure functions had been first obtained by Politano and Pouquet (1998). The Yaglom law (3.16) can be expressed through the sum of six terms, each coupling in different way magentic field and velocity fluctuations:

$$\begin{aligned} Y_r^{\pm} = \left\langle |\Delta v_i|^2 \, \Delta v_r \right\rangle &+ \left\langle |\Delta b_i|^2 \, \Delta v_r \right\rangle \\ \pm 2 \left\langle (\Delta v_i \Delta b_i) \Delta v_r \right\rangle &\mp \left\langle |\Delta v_i|^2 \, \Delta b_r \right\rangle \\ \mp \left\langle |\Delta b_i|^2 \, \Delta b_r \right\rangle &- 2 \left\langle (\Delta v_i \Delta b_i) \Delta b_r \right\rangle \end{aligned} \tag{3.17}$$

The first three terms represent the energy (and cross-helicity) transported by the longitudinal velocity fluctuations Δv_r, while the last three terms give the magnetic field contribution to the pseudo-energy transfer rate. The MHD scaling law (3.16) holds for the sum of all its terms.

Chapter 4

The Yaglom law in solar wind

4.1 Observation of turbulent cascade in fast polar wind

In this thesis, we show that relation (3.16) is indeed satisfied in some periods within solar wind. In order to avoid variations of the solar activity and ecliptic disturbances (like slow wind sources, Coronal Mass Ejections, ecliptic current sheet, and so on), we use high speed polar wind data measured by the Ulysses spacecraft (Smith et al. 1995, Balog et al. 1995). In particular, we analyse here the first seven months of 1996, when the heliocentric distance slowly increased from 3 AU to 4 AU, while the heliolatitude decreased from about 55° to 30° (see Fig. 4.1). The fields components are given in the RTN reference frame (Fig. 2.11). Note that, since the wind speed in the spacecraft frame is much larger than the typical velocity fluctuations, and is nearly aligned with the R radial direction, time fluctuations are in fact spatial fluctuations with time and space scales (τ and r respectively) related through the Taylor hypothesis (section 2.3), so that $r = -\langle v_R \rangle \tau$ (note the *reversed* sign).

From the 8 minutes averaged time series $\boldsymbol{z}^{\pm}(t)$ (section 2.2.3), we compute the time increments $\Delta\boldsymbol{z}^{\pm}(\tau;t) = \boldsymbol{z}^{\pm}(t+\tau) - \boldsymbol{z}^{\pm}(t)$, and obtain the mixed third order structure function

$$Y^{\pm}(-\langle v_R \rangle_t \tau) = \left\langle |\Delta\boldsymbol{z}^{\pm}(\tau;t)|^2 \, \Delta z_R^{\mp}(\tau;t) \right\rangle_t$$

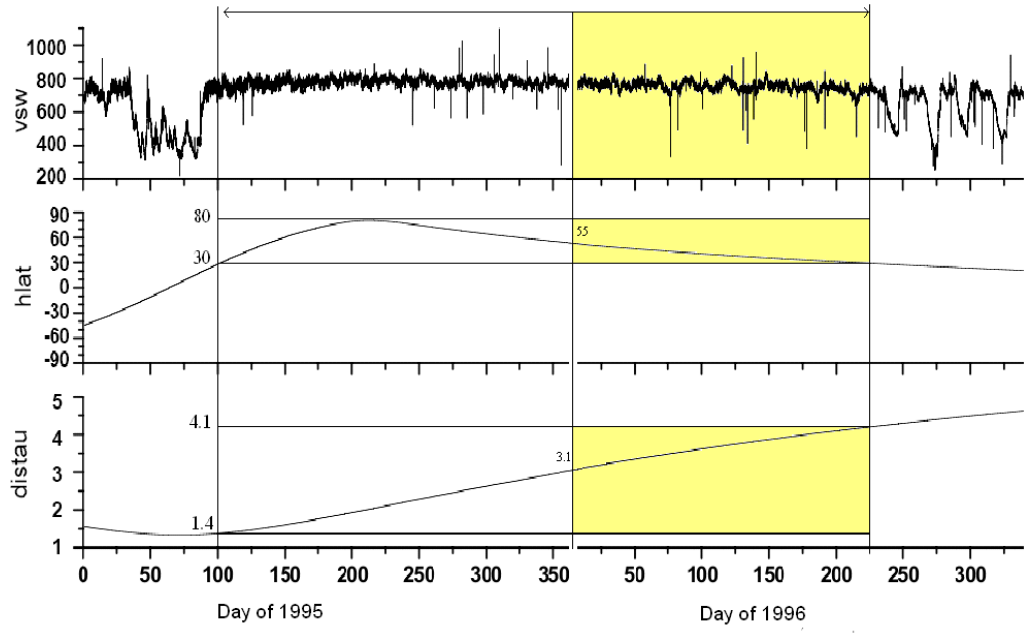

Figure 4.1: Velocity of the Solar Wind as measured by Ulysses during the years 1995 and 1996. The highlighted period has been analysed in this section.

using moving averages $\langle \bullet \rangle_t$ on the time t over periods spanning around 11 days, during which the fields can be considered stationary. A linear scaling $Y^{\pm}(\tau) = 4/3\,\epsilon^{\pm}\,\langle v_R \rangle_t\,\tau$ is indeed observed in a significant fraction of the periods we examined, with an inertial range spanning as much as two decades, indicating the existence of a well defined inertial energy cascade range in plasma turbulence (Sorriso-Valvo et al., 2007). In fact, solar wind inertial ranges can even be larger than the ones reported for laboratory fluid flows (Danaila et. al, 2001), showing the robustness of this result. This is the *first experimental validation* of the turbulence MHD theorem discussed in the section 3.2.2.. Figure 4.2 shows some example of scaling and the extension of the inertial range, for both $Y^{\pm}(\tau)$.

The linear scaling law generally extends from a few minutes to one day or more. This happens in about 20 periods of a few days in the 7 months considered. Several other periods are found in which the scaling range is considerably reduced. In particular, the sign of $Y^{\pm}(\tau)$ is observed to be ei-

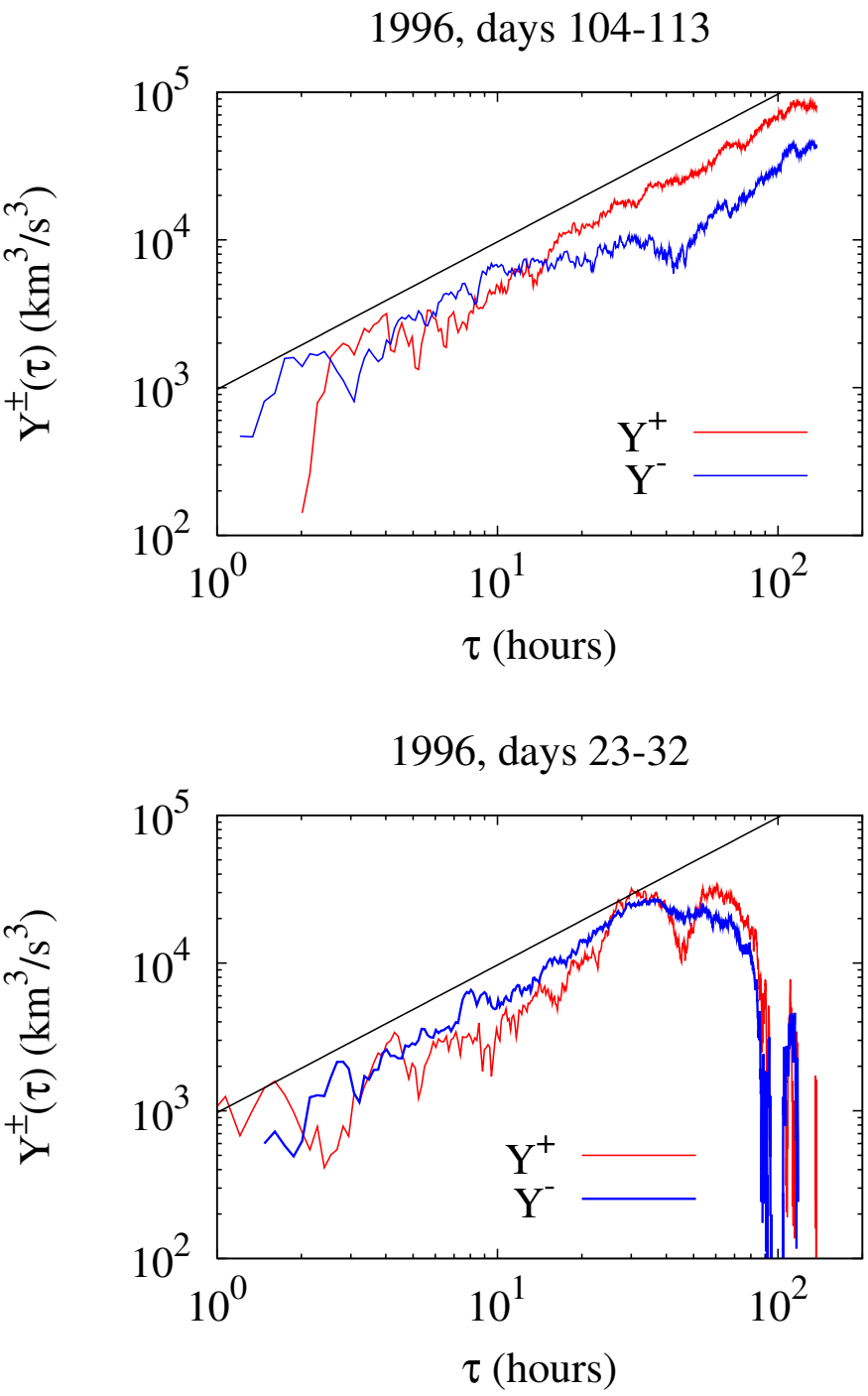

Figure 4.2: The scaling behaviour of $Y^{\pm}(\tau)$ as a function of the time scale τ for two periods we examined. Different colours of the curves refer to positive and negative values of the mixed structure functions $Y^{\pm}(\tau)$ and thus of $\epsilon^{\pm}$. The full black line correspond to a linear scaling law to guide the eye.

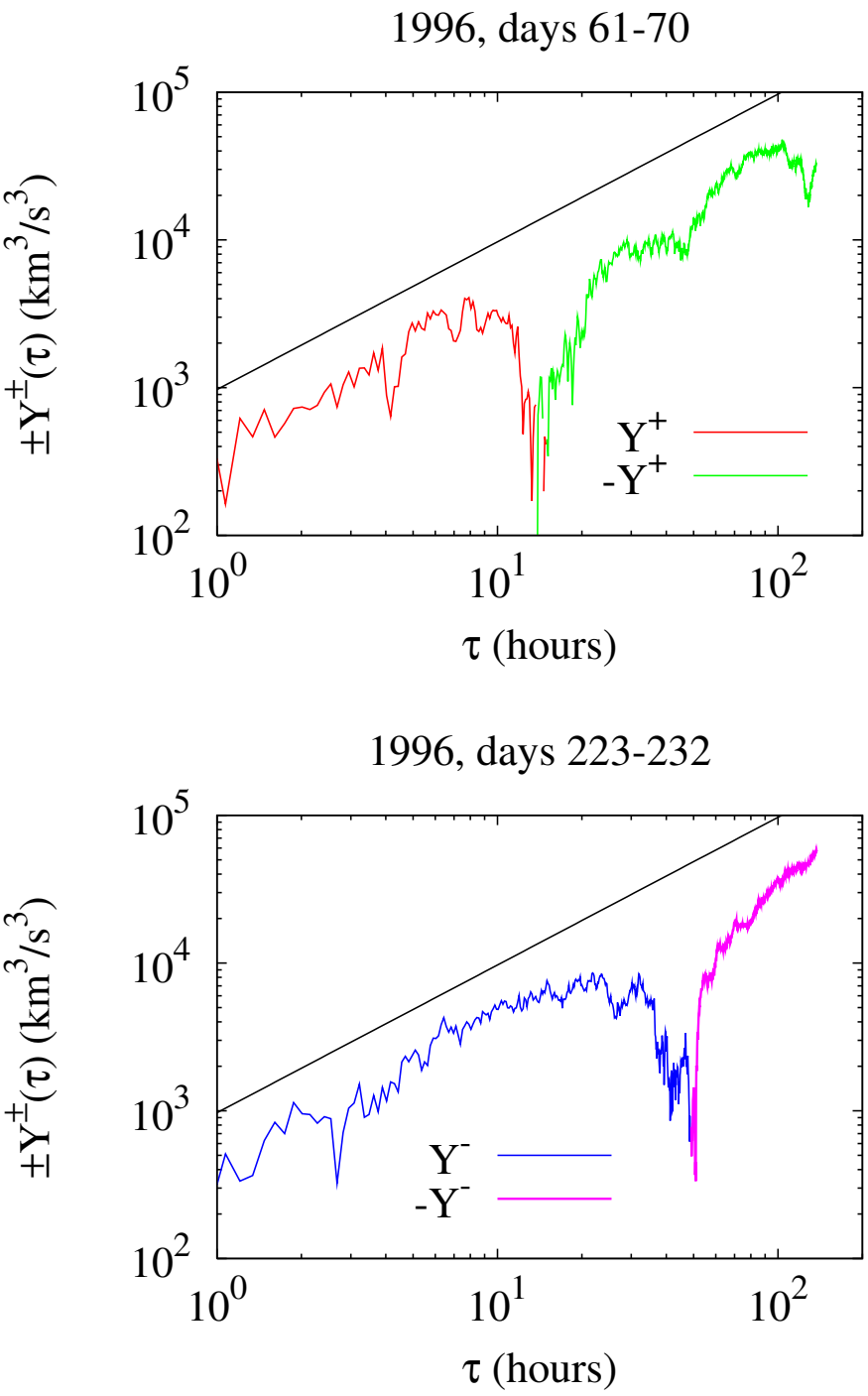

Figure 4.3: The scaling behaviour of $Y^{\pm}(\tau)$ as a function of the time scale τ for two different periods we examined. Different colours of the curves refer to positive and negative values of the mixed structure functions $Y^{\pm}(\tau)$ and thus of $\epsilon^{\pm}$. The full black line correspond to a linear scaling law to guide the eye.

ther positive or negative. Since pseudo-energies dissipation rates are positive defined, a positive sign for $Y^{\pm}(\tau)$ (negative for $Y^{\pm}(r)$) indicates a (standard) forward cascade with pseudo-energies flowing towards the small scales to be dissipated. On the contrary, a negative $Y^{\pm}(\tau)$ is the signature of an *inverse* cascade where the energy flux is being transferred on average toward larger scales.

It is worth noting that, in a large fraction of cases, both $Y^{\pm}(\tau)$ switch from positive to negative linear scaling (or viceversa) within the same time period when going from small to large scales (see Figure 4.3). The occurrence of both kind of cascades within the same flow is not so uncommon within hydrodynamic turbulence. This phenomenon has been attributed to some large scale instability, as observed for example in geophysical flows or when the flow is affected by a strong rotation. In the case of solar wind plasma a possible explanation for the inverse cascade could be the enhanced intensity of the background magnetic field. This would make the turbulence mainly bidimensional allowing for an inverse cascade as observed in numerical simulations (Baroud et Al. 2002). It should also be noticed that in most of the cases the time scale at which the cascade reverses its sign is of the order of 1 day. This scale roughly indicates where the small scale Alfvénic correlations between velocity and magnetic field are lost. This could mean that the nature of the fluctuations changes across the break. However, these particular aspects still deserve to be adequately considered within the solar wind context. The most evident scalings (positive and negative) are shown in the Figures 4.5 $\div$ 4.19 while the correposding informations are collected in the tab 4.1.

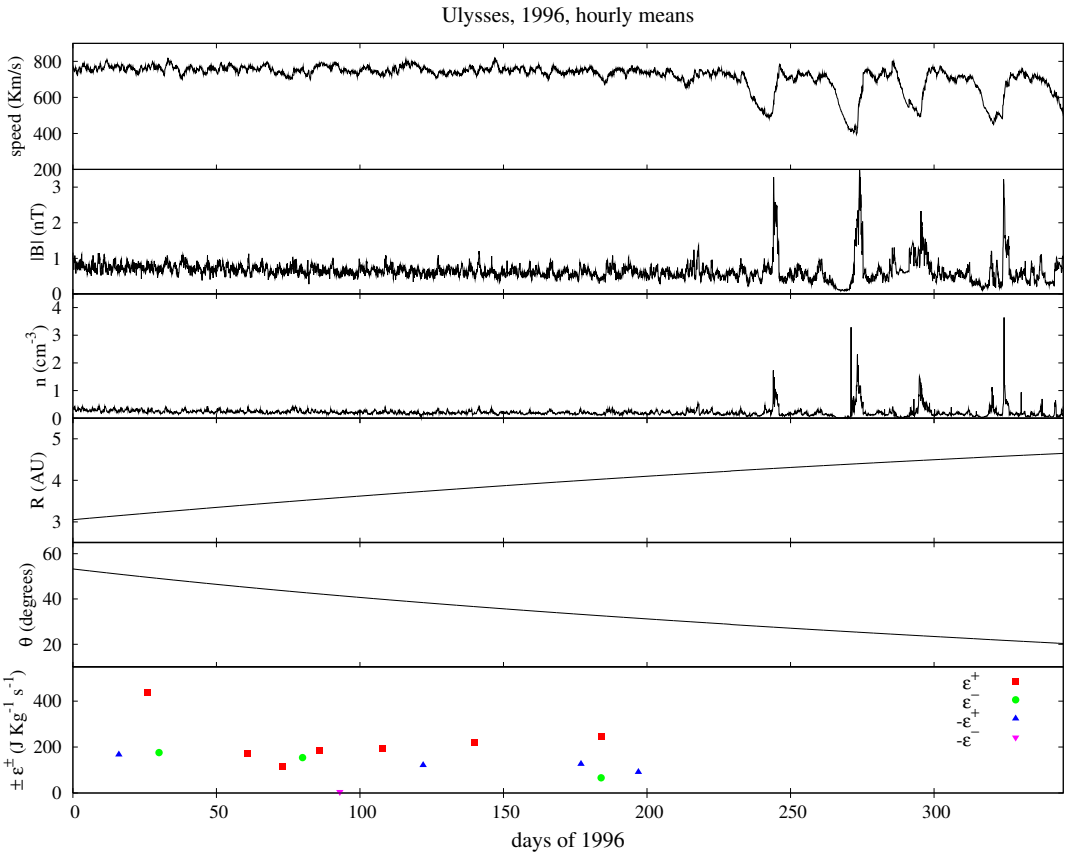

Figure 4.4: Hourly averaged quantities are represented as a function of the flight time of Ulysses. The top panels represent respectively the solar wind speed, the magnitude of the magnetic field, the particle density, the distance from the sun and the heliolatitude angle. In the bottom panel the values of $\epsilon^{\pm}$, calculated through a fit with the function (3.16) during the periods where a clear linear scaling exists, are reported.

day interval (time index)	$(\epsilon^- \pm \delta\epsilon^-)$ $(\frac{J}{kg\,m})$	$(\langle V\rangle \pm \delta\langle V\rangle)$ $\frac{km}{s}$	inertial range
$24 \div 35$ (4370)	176 ± 13	709 ± 114	$3\ h \div 2\ g$
$74 \div 85$ (13470)	154 ± 32	699 ± 102	$1\ h \div 4\ g$
$178 \div 189$ (32200)	66 ± 24	678 ± 95	$5\ h \div 4\ g$
day interval (time index)	$(\epsilon^+ \pm \delta\epsilon^+)$ $(\frac{J}{kg\,m})$	$(\langle V\rangle \pm \delta\langle V\rangle)$ $\frac{km}{s}$	inertial range
$11 \div 22$ (2000)	-167 ± 13	701 ± 105	$1\ h \div 3\ g$
$21 \div 32$ (3950)	436 ± 32	694 ± 112	$30\ m \div 2\ g$
$56 \div 67$ (10150)	174 ± 24	707 ± 131	$1\ h \div 3\ g$
$68 \div 79$ (12360)	115 ± 19	675 ± 96	$2\ h \div 4\ g$
$69 \div 80$ (12550)	113 ± 12	674 ± 102	$2\ h \div 4\ g$
$81 \div 92$ (14700)	185 ± 25	690 ± 90	$3\ h \div 4\ g$
$103 \div 114$ (18695)	194 ± 22	690 ± 85	$5\ h \div 4\ g$
$117 \div 128$ (21111)	-121 ± 13	696 ± 94	$2\ h \div 4\ g$
$135 \div 146$ (24400)	218 ± 28	707 ± 110	$3\ h \div 2\ g$
$172 \div 183$ (31060)	-126 ± 15	678 ± 103	$10\ h \div 4\ g$
$184 \div 195$ (33240)	216 ± 25	696 ± 88	$30\ m \div 4\ g$
$192 \div 203$ (34680)	-91 ± 11	690 ± 94	$4\ h \div 4\ g$

Table 4.1: The tab collects the energy tranfer rates ϵ^+ and ϵ^- estimated through fits of the Yaglom scaling law. In the first column we have the exrtemes (in terms of days of 1996) of the 11-days windows in which the scalings were observed together with an index that identify the windows. The last column shows the extension of the inerntial range in the time domain.

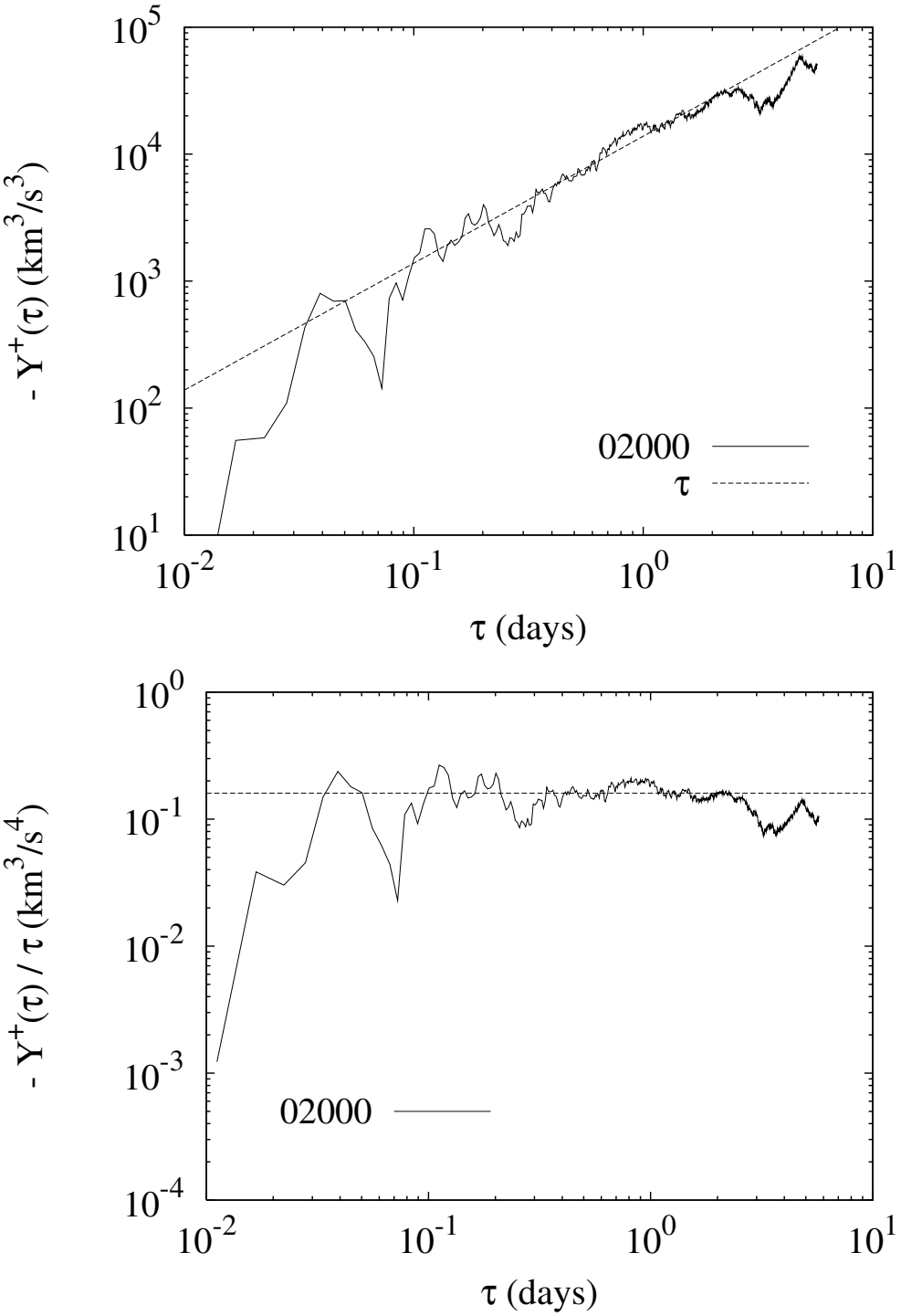

Figure 4.5: The Yaglom scaling $Y^{\pm}$ in the window 2000

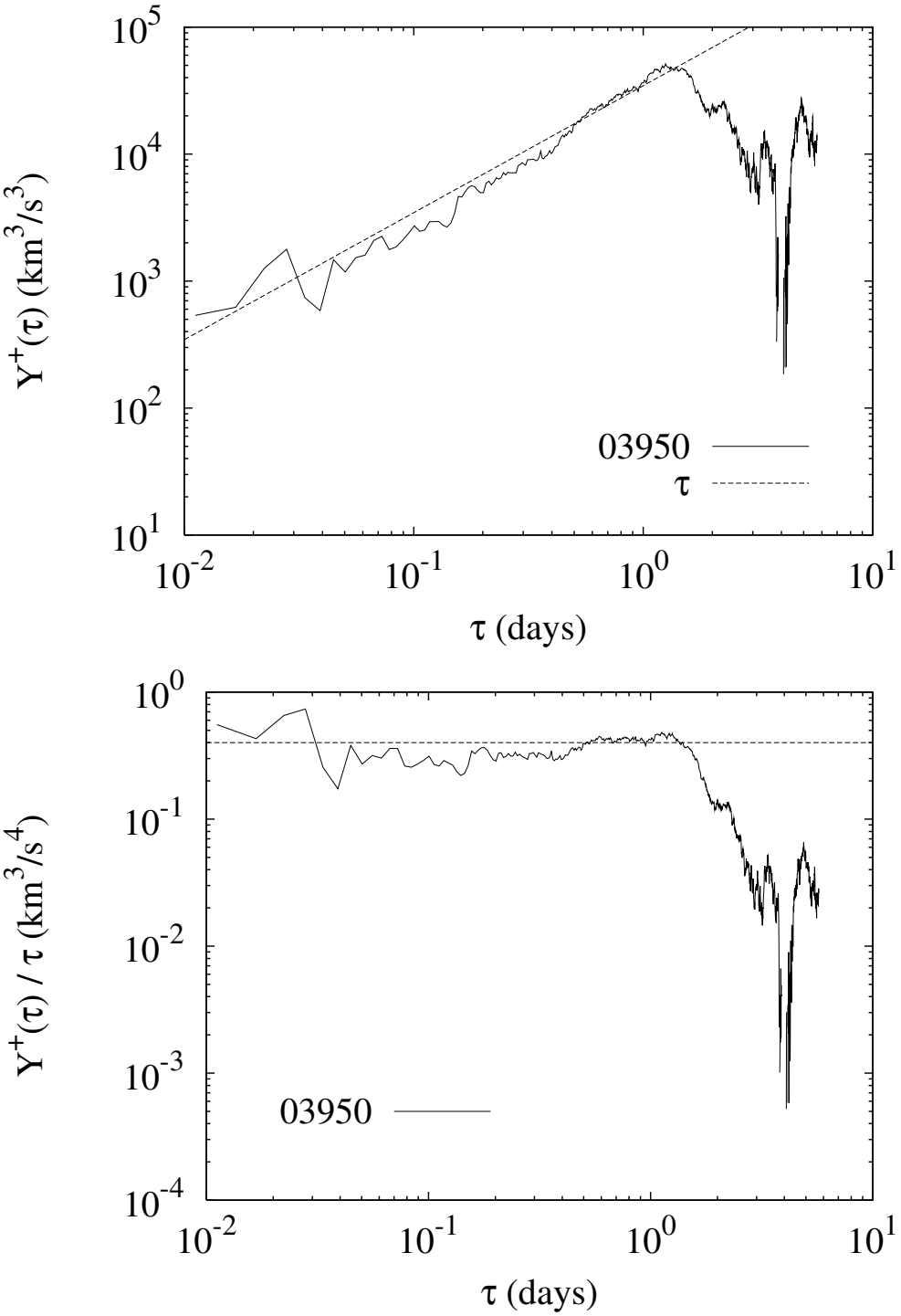

Figure 4.6: The Yaglom scaling $Y^{\pm}$ in the window 3950.

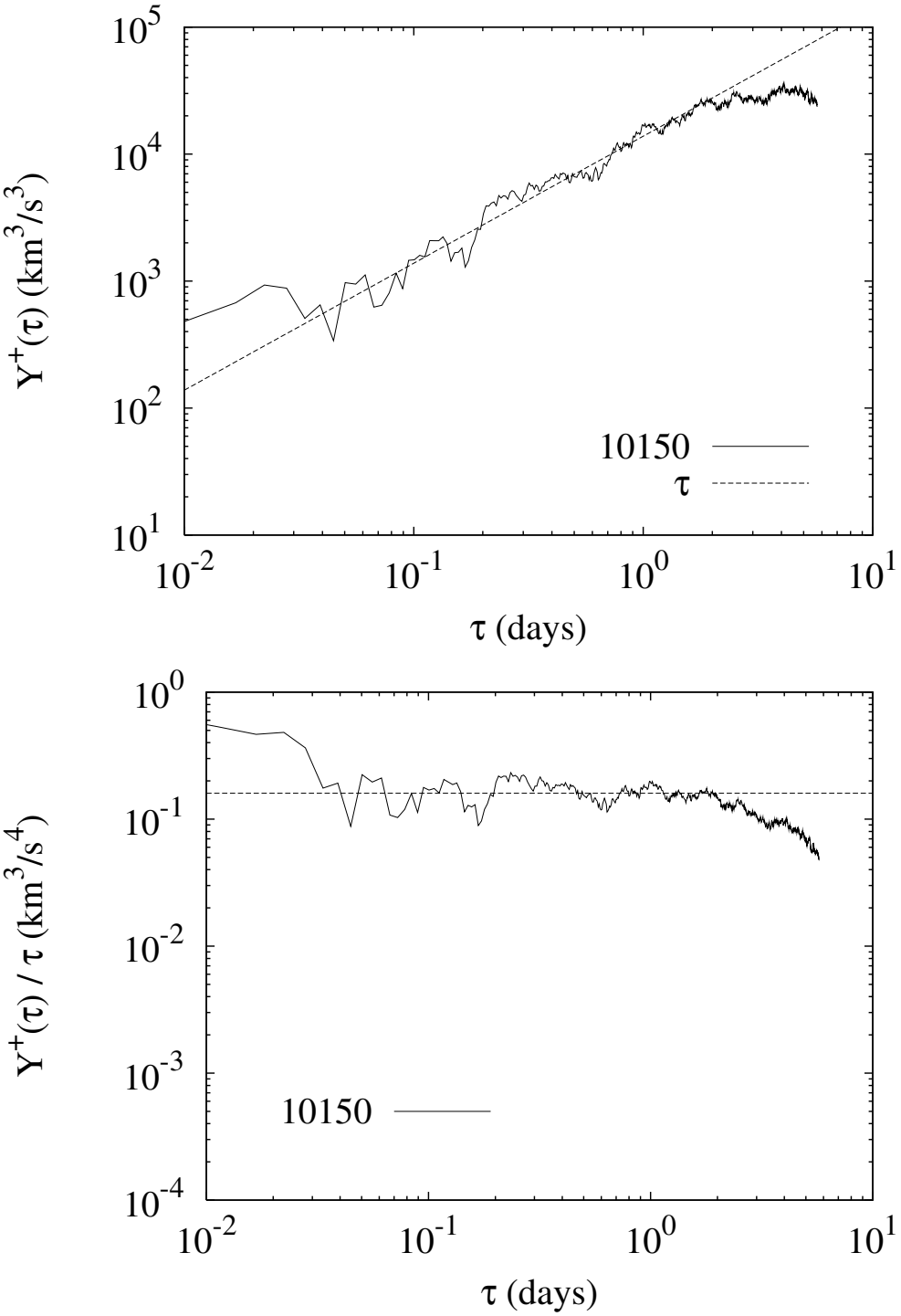

Figure 4.7: The Yaglom scaling $Y^{\pm}$ in the window 10150

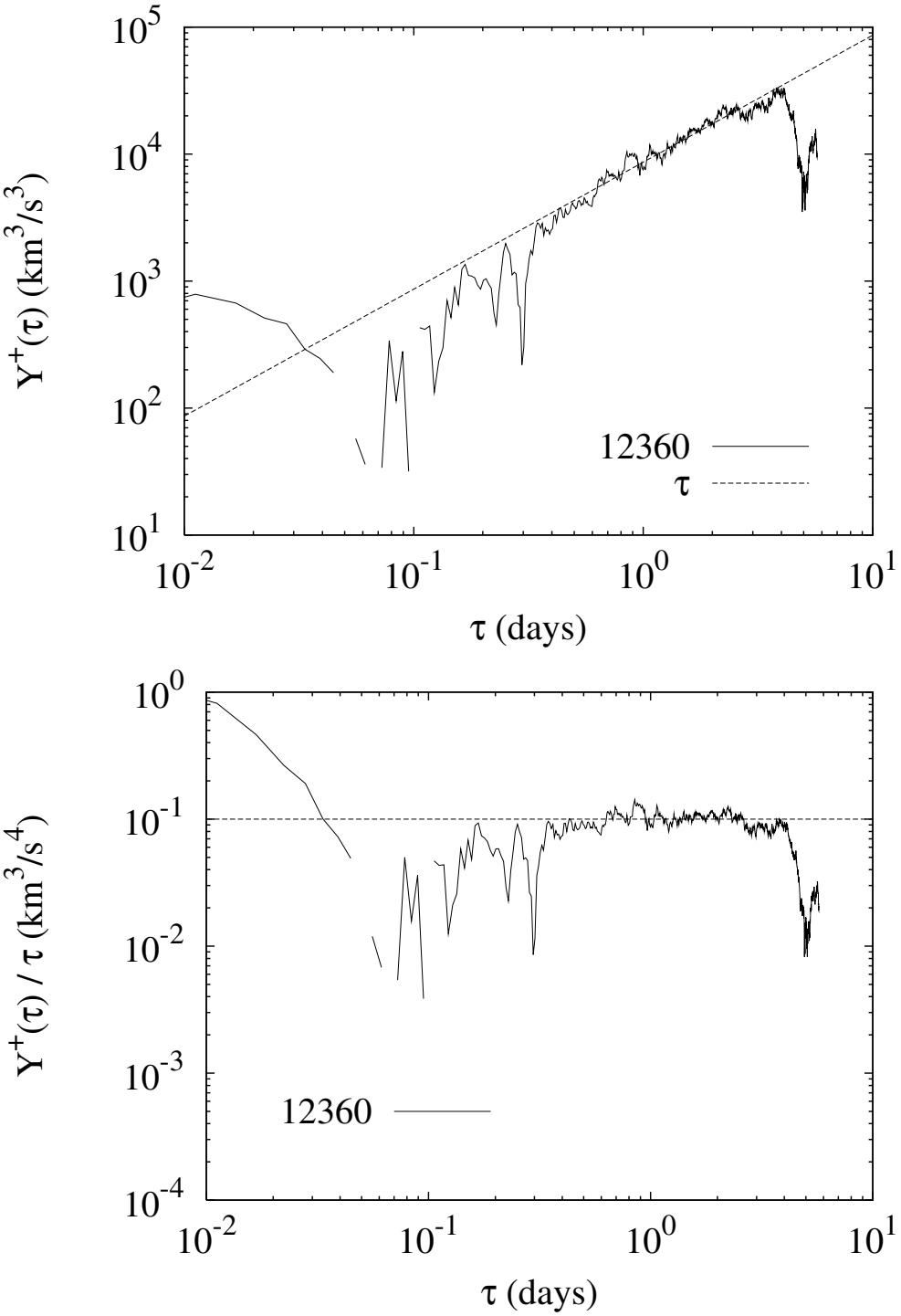

Figure 4.8: The Yaglom scaling $Y^{\pm}$ in the window 12360

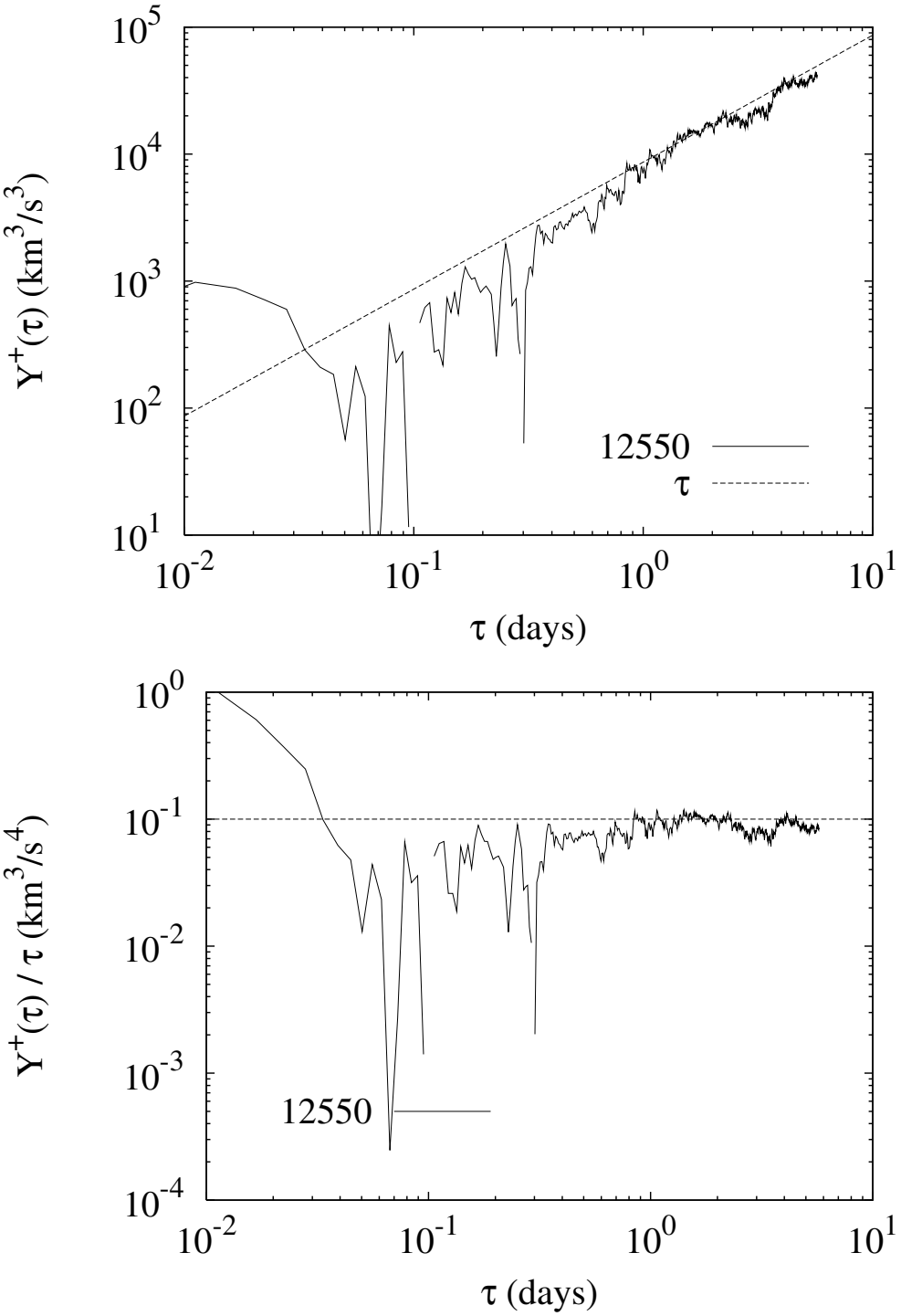

Figure 4.9: The Yaglom scaling $Y^{\pm}$ in the window 12550

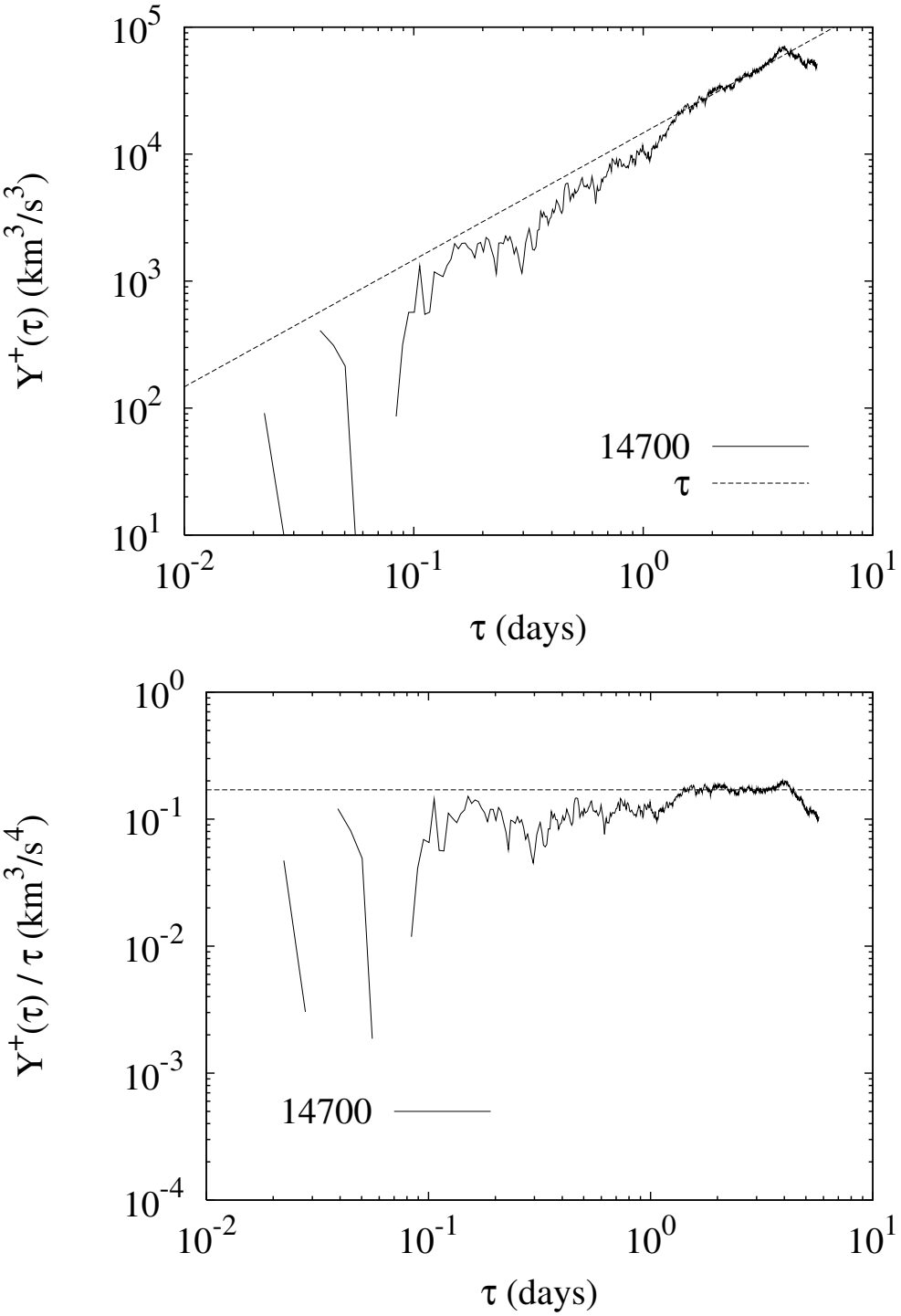

Figure 4.10: The Yaglom scaling $Y^{\pm}$ in the window 14700

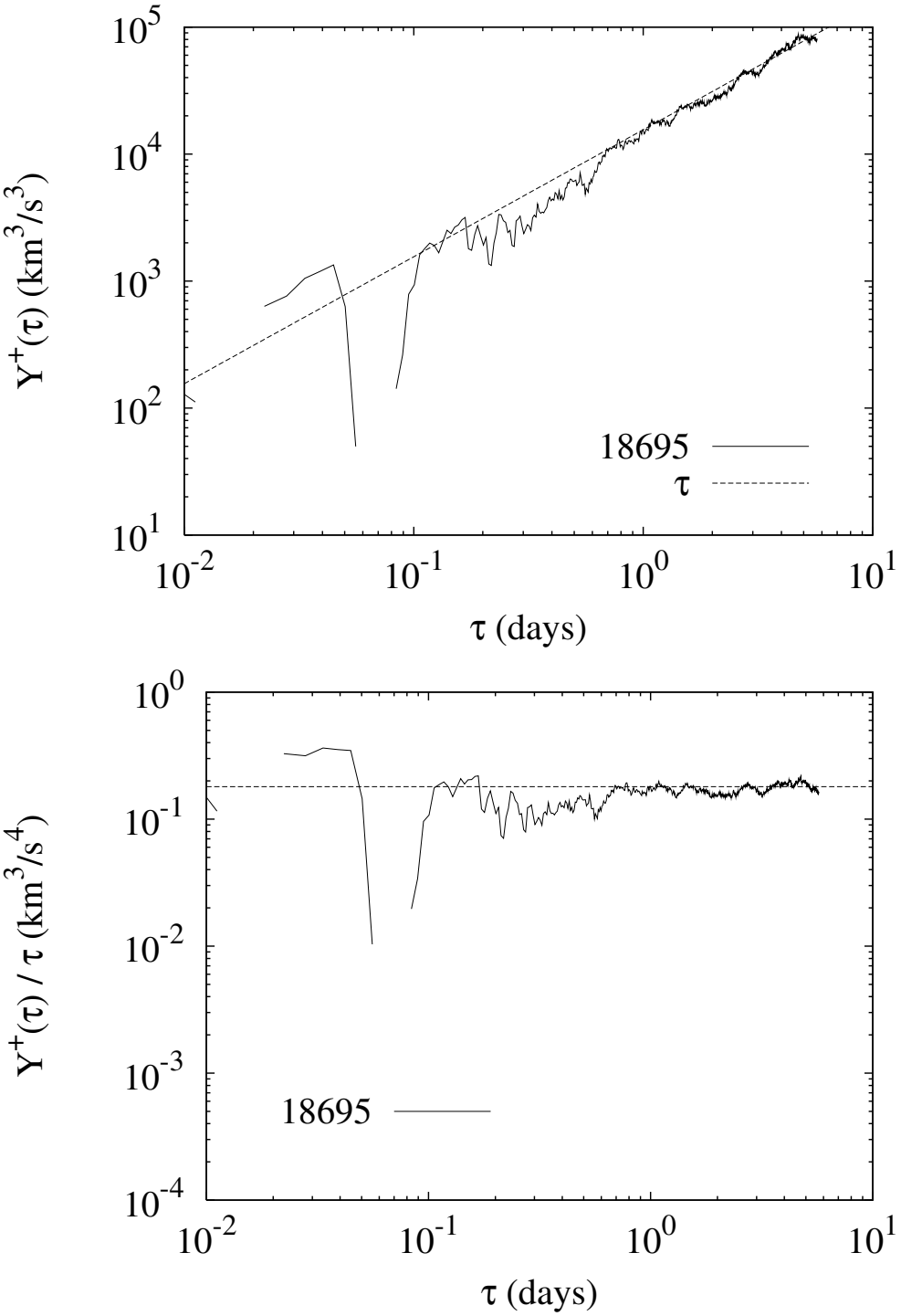

Figure 4.11: The Yaglom scaling $Y^{\pm}$ in the window 18695

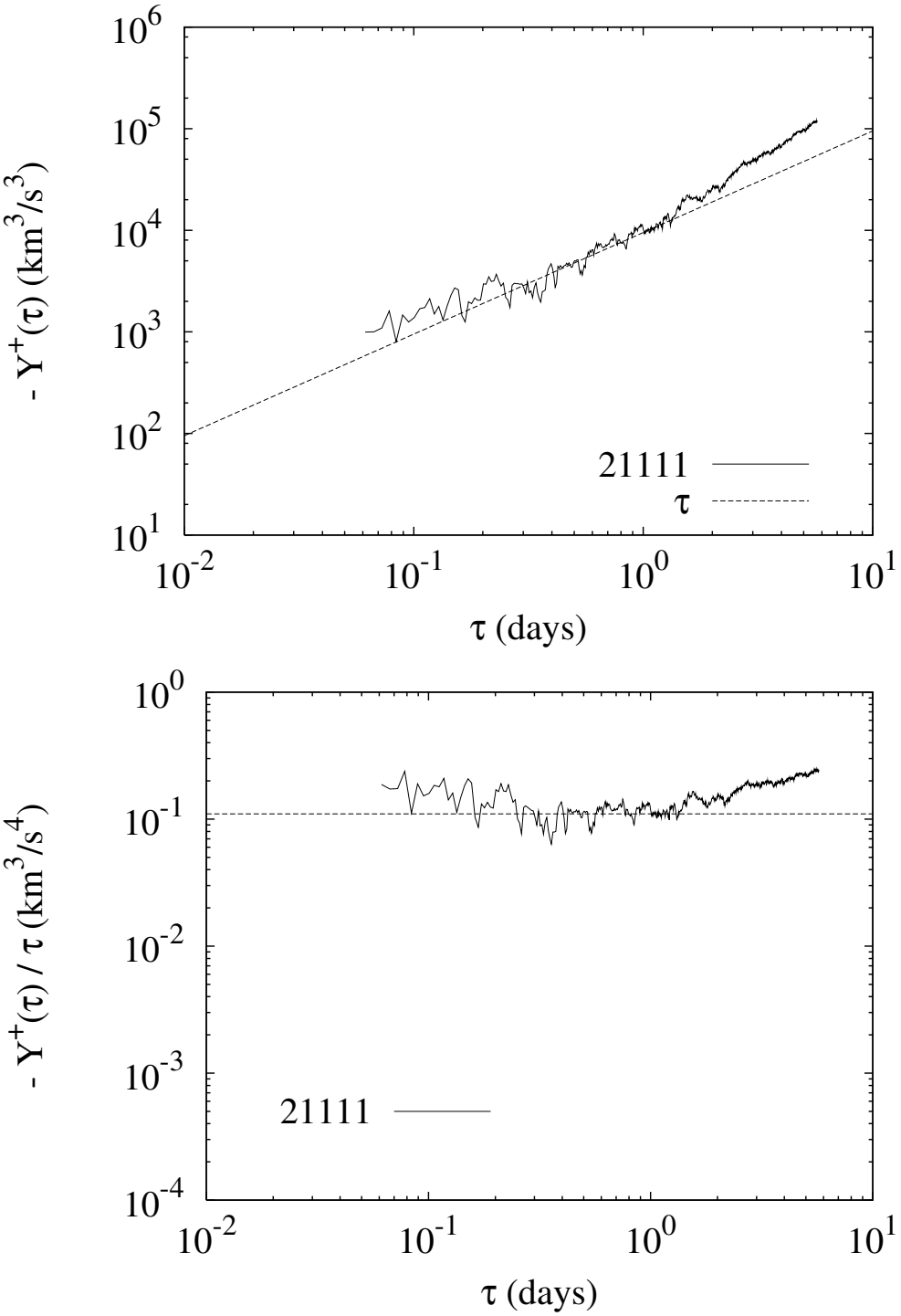

Figure 4.12: The Yaglom scaling $Y^{\pm}$ in the window 21111

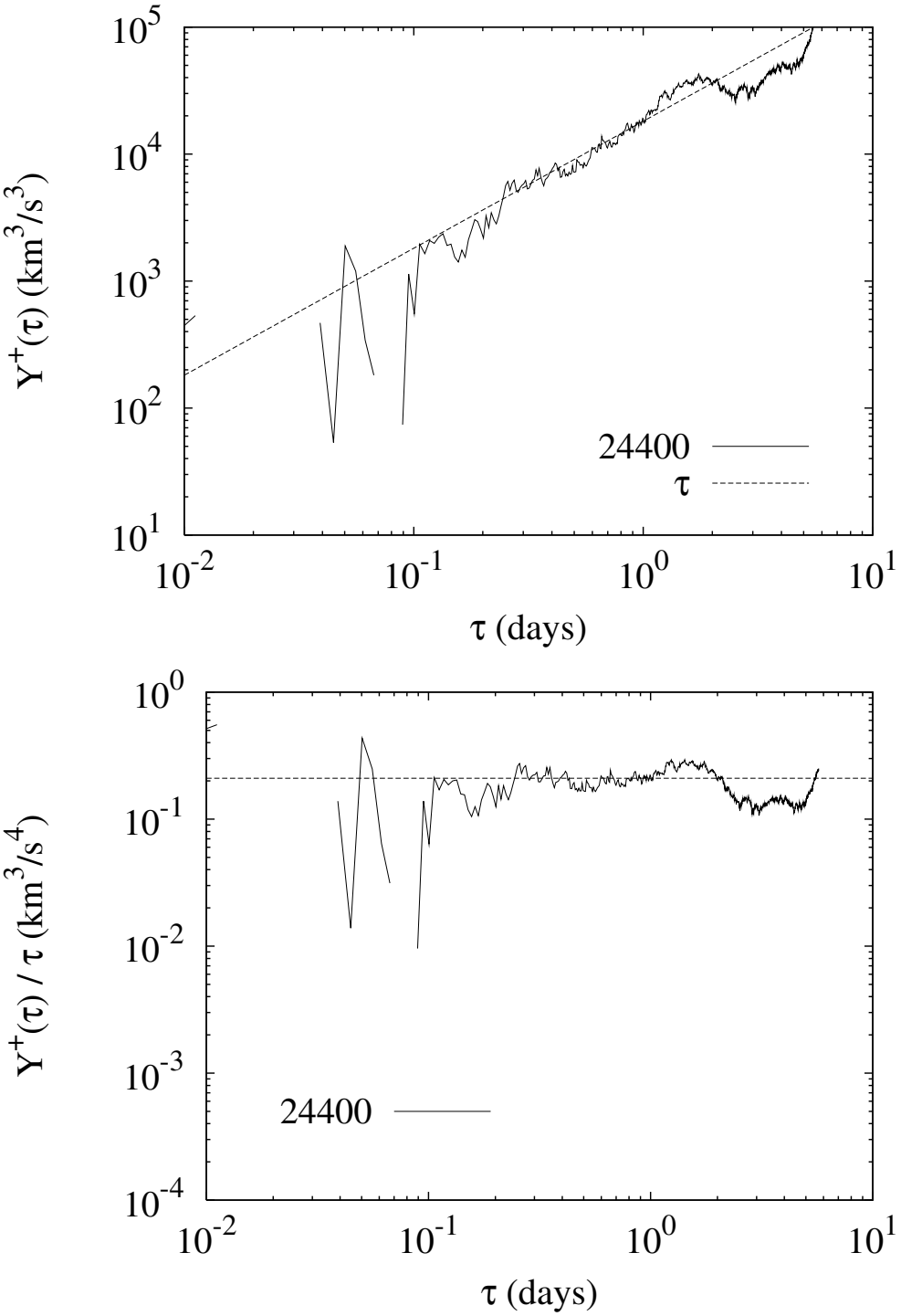

Figure 4.13: The Yaglom scaling $Y^{\pm}$ in the window 24400

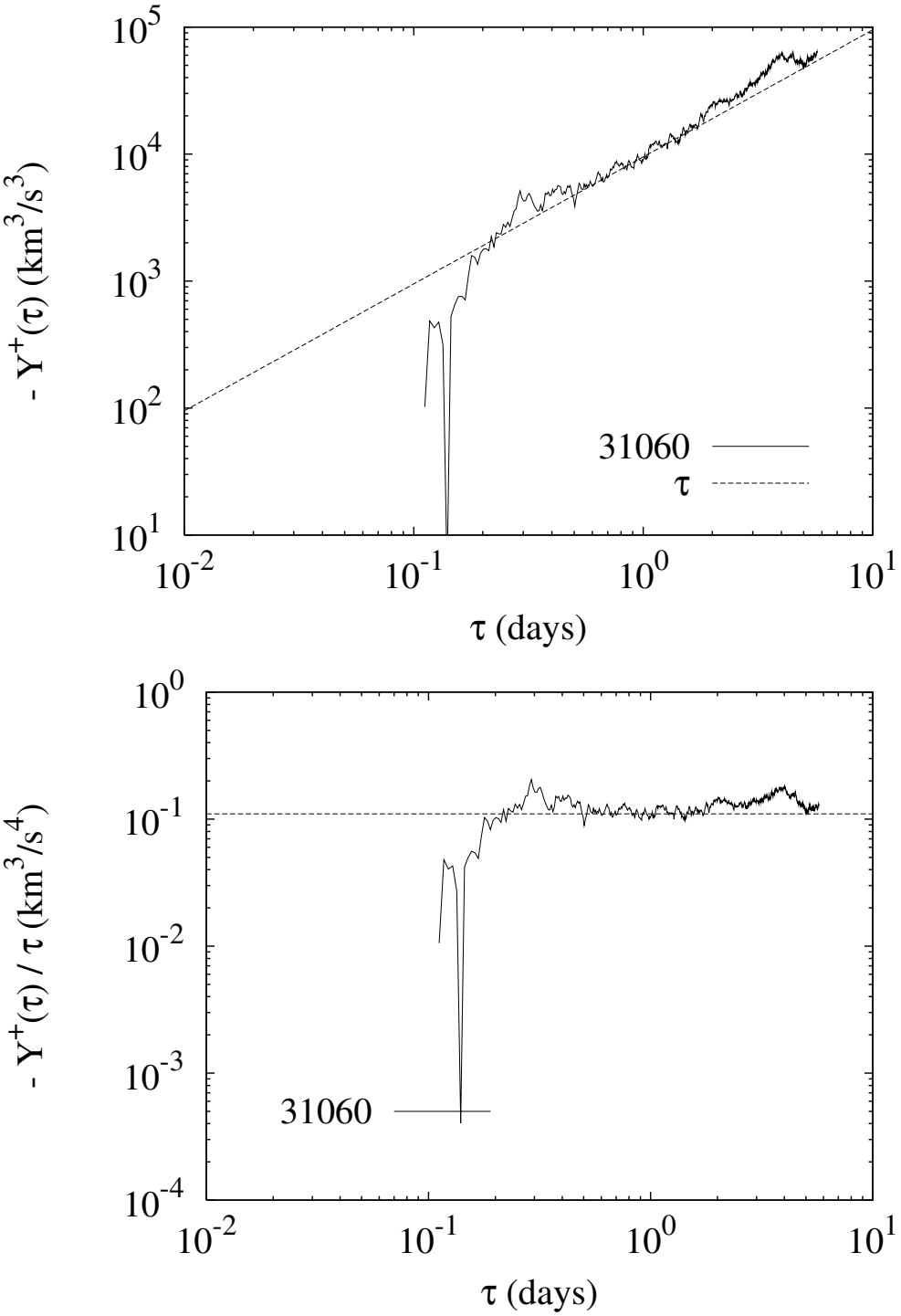

Figure 4.14: The Yaglom scaling $Y^{\pm}$ in the window 31060

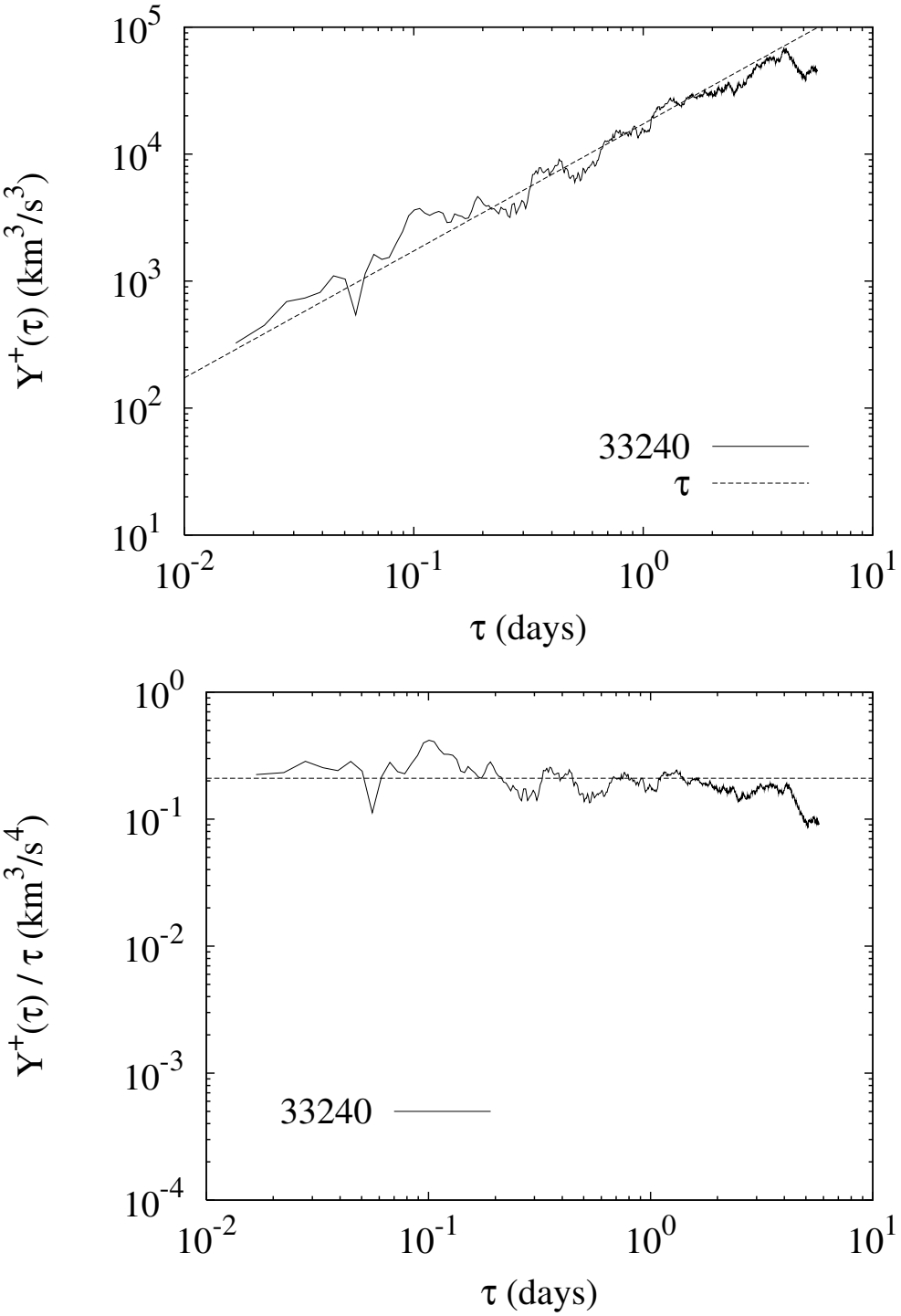

Figure 4.15: The Yaglom scaling $Y^{\pm}$ in the window 33240

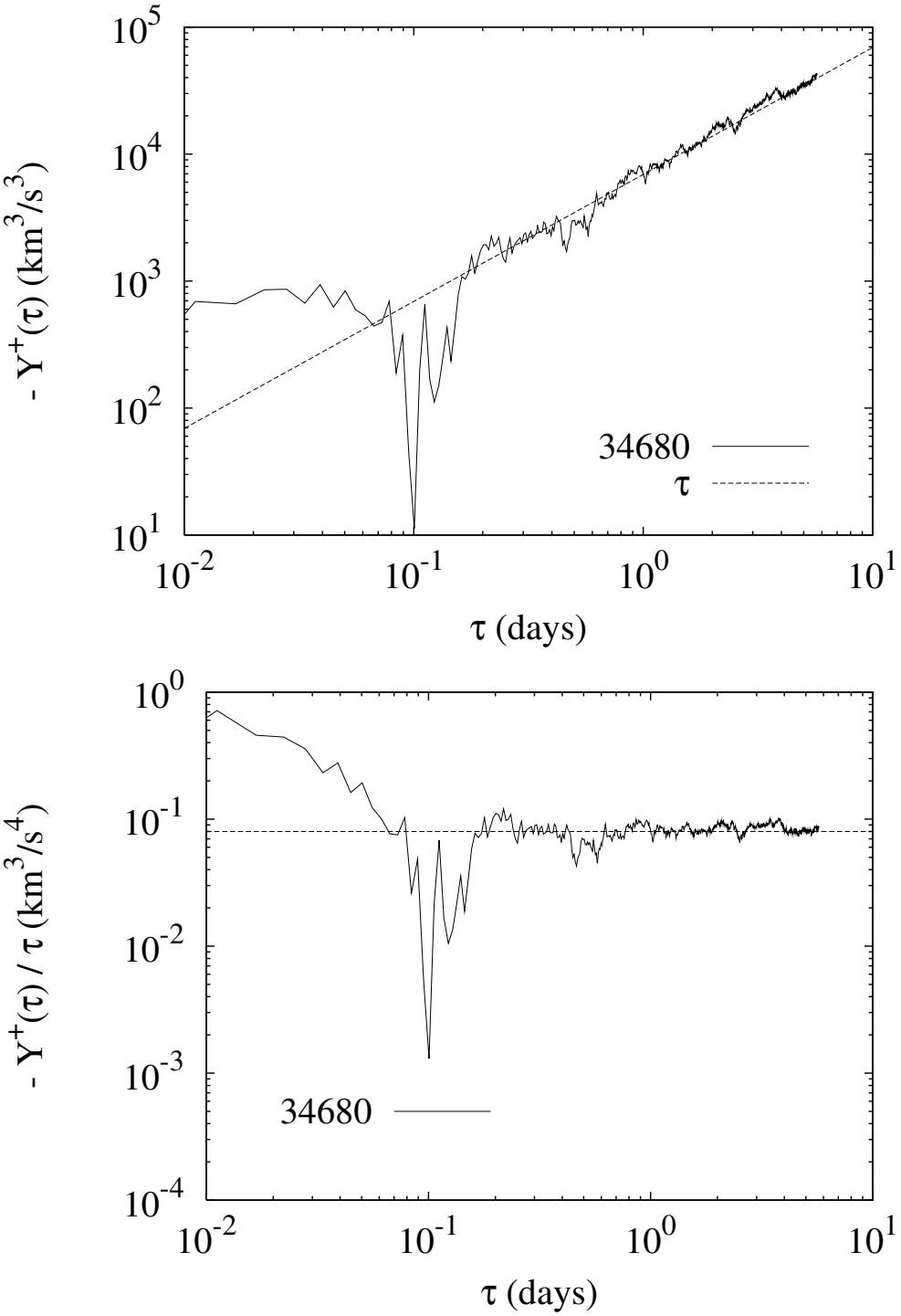

Figure 4.16: The Yaglom scaling $Y^{\pm}$ in the window 34680

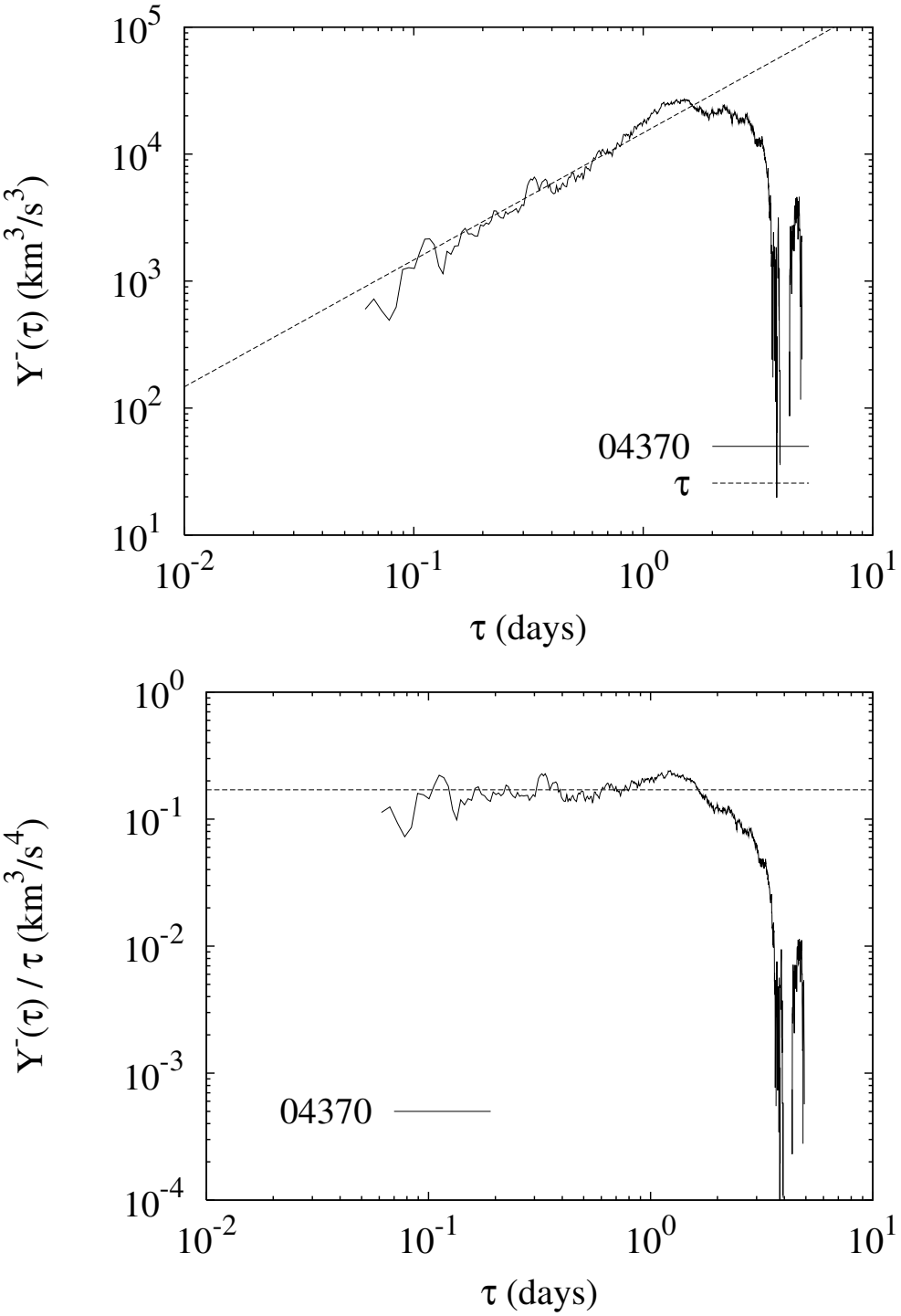

Figure 4.17: The Yaglom scaling $Y^{\pm}$ in the window 4370

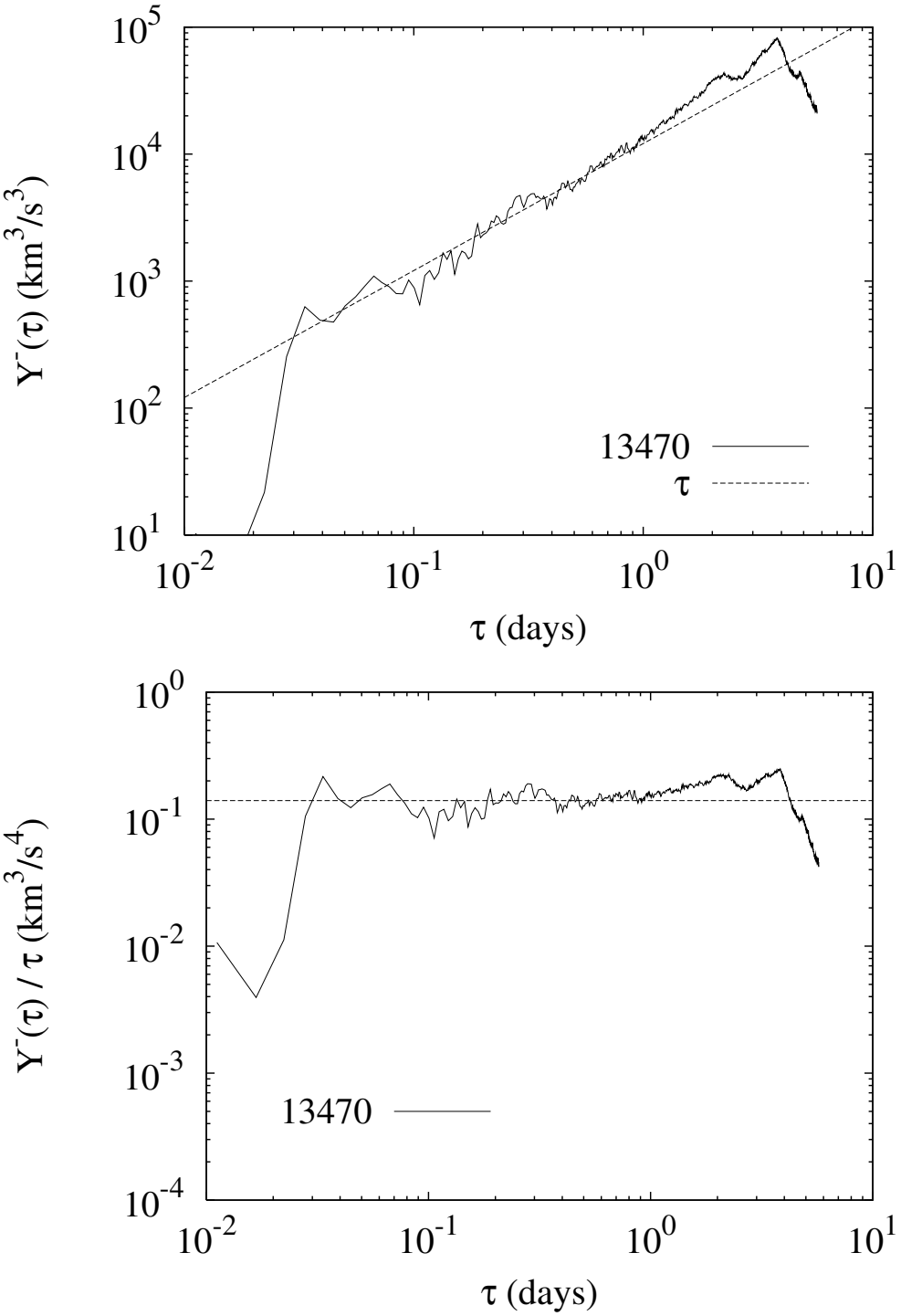

Figure 4.18: The Yaglom scaling $Y^{\pm}$ in the window 13470

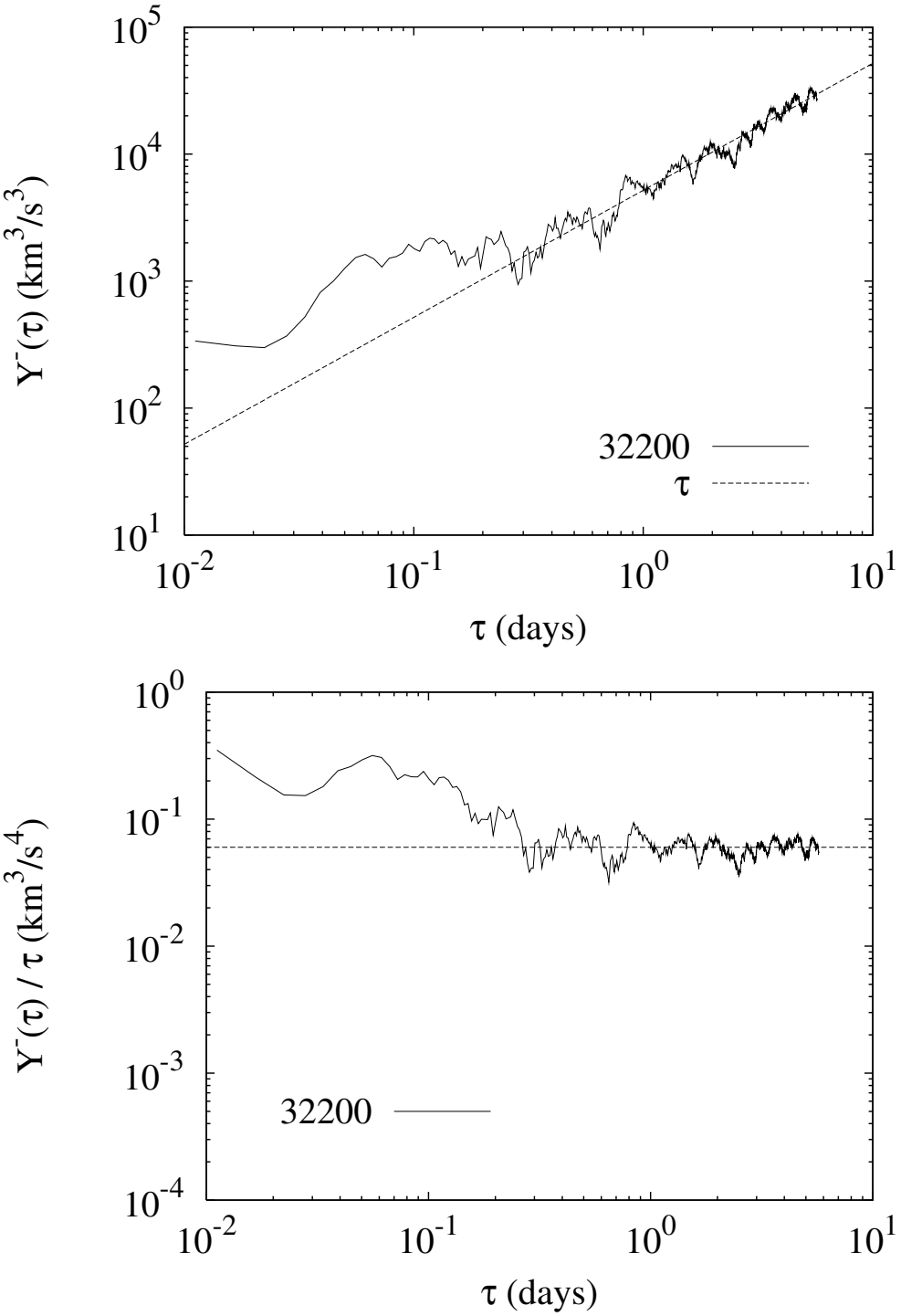

Figure 4.19: The Yaglom scaling $Y^{\pm}$ in the window 32200

Figure 4.22 shows the location of the most evident scaling intervals, together with the values of the flux rate $\epsilon^{\pm}$ estimated through a fit of the scaling law (3.16), typically of the order of a few hundreds in $\mathrm{J\,kg^{-1}\,s^{-1}}$. For comparison, values found for ordinary turbulent fluids are $1 \div 50\ \mathrm{J\,kg^{-1}\,s^{-1}}$ (Cerutti and Meneveau 2000).

At this point, the question is why the scaling is not observed all the time within the solar wind. As already stated, equation (3.16) is verified only when local homogeneity, incompressiblity and isotropy conditions are satisfied. In general, solar wind inhomogeneities play a major role at large scales so that local homogeneity is generally fulfilled within the range of interest. Regarding incompressibility, it has been shown that compressive phenomena mainly affect shocked regions and dynamical interaction regions like stream-stream interface. However, the time interval we analyse, because of Ulysses high latitude location, is not affected by these compressive phenomena. On the other hand, it has also been shown that magnetic field compressibility increases mainly at very small scales within the fast wind regime. It follows that the incompressibility assumption can be considered valid to a large extent for the analyzed interval and at intermediate scales. The large scale anisotropy, mainly due to the average magnetic field, is only partially lost at smaller scales, and a residual anisotropy is always present (Sorriso-Valvo 2006), generally breaking the local isotropy assumption. Thus, while inhomogeneity, compressibility and anisotropy could all be responsible for the loss of linear scaling, anisotropy probably is the main candidate within high latitude regions of the solar wind. It is important to note that the presence of a Yaglom-like law that involves the third order mixed moment, is more general than the phenomenology usually involving the second order moment. Indeed, while the Yaglom MHD relation (3.16) involves only differences along the parallel direction, that are in fact the only quantities accessible from single satellite measurements, phenomenological arguments involve the full spatial dependence of vector fields that cannot be directly measured yet. This means that our result is compatible with both Kolmogorov and Iroshnikov-Kraichnan type cascade (Dobrowolny et al., 1980), and does not help in discriminating between these phenomenologies.

4.2 Turbulence in the ecliptic wind

The results presented in previous section refer to the steady, fast polar wind, where the ecliptic disturbances of solar origin are reduced. Other authors have studied the Yaglom law in ecliptic wind at 1AU, obtaining good results and values of the energy transfer rate higher than the ones reported in the previous section. Figure 4.20 shows examples of fast and slow wind ecliptic scaling of the mixed third order moment as in Yaglom law, for both Y^+ and Y^-. Figure 4.21 shows the locations of the scaling regions (top panel) in the alternate fast and slow ecliptic stream, and the corresponding values of the pseudo-energy transfer rates (bottom panel). A clear difference between the fast and slow wind appears. First of all, the pseudo-energy transfers in the fast wind streams are comparable with the ones obtained in polar wind, where only fast wind is present. This confirm that the results are consistent and that the energy transfer rate depends on the bulk velocity of the wind. The slow streams, on the contrary, are characterized by larger values of $\epsilon^{\pm}$, so that a clear separation between the two species is visible in figure 4.21 (Marino et al., 2009). This is in agreement with the observation of larger intermittency in the slow streams (Sorriso-Valvo 1999). Moreover, in the fast streams only one of the modes (Y^+ or Y^-) is prevalently observed to satisfy the Yaglom law in a given location. In the slow streams, the two modes have often simultaneous scaling, which allows the estimation of the total energy $\epsilon_{tot} = (\epsilon^+ + \epsilon^-)/2$. This difference suggests that in the fast ecliptic wind the Alfvénic correlations kill the turbulence in one of the modes, suggesting the presence of purely alfvénic turbulence (Marino et al, 2009). Both observations are evidences that fast and slow wind own different properties and, therefore, should always be analysed separately. In slow streams, the scaling samples are interestingly found in correspondence with the stream interfaces (figure 4.21). This suggests that the turbulent cascade observed through the Yalgom law could be activated by the energy injection due to the shears of velocity and magnetic field, that characterize the interface regions.

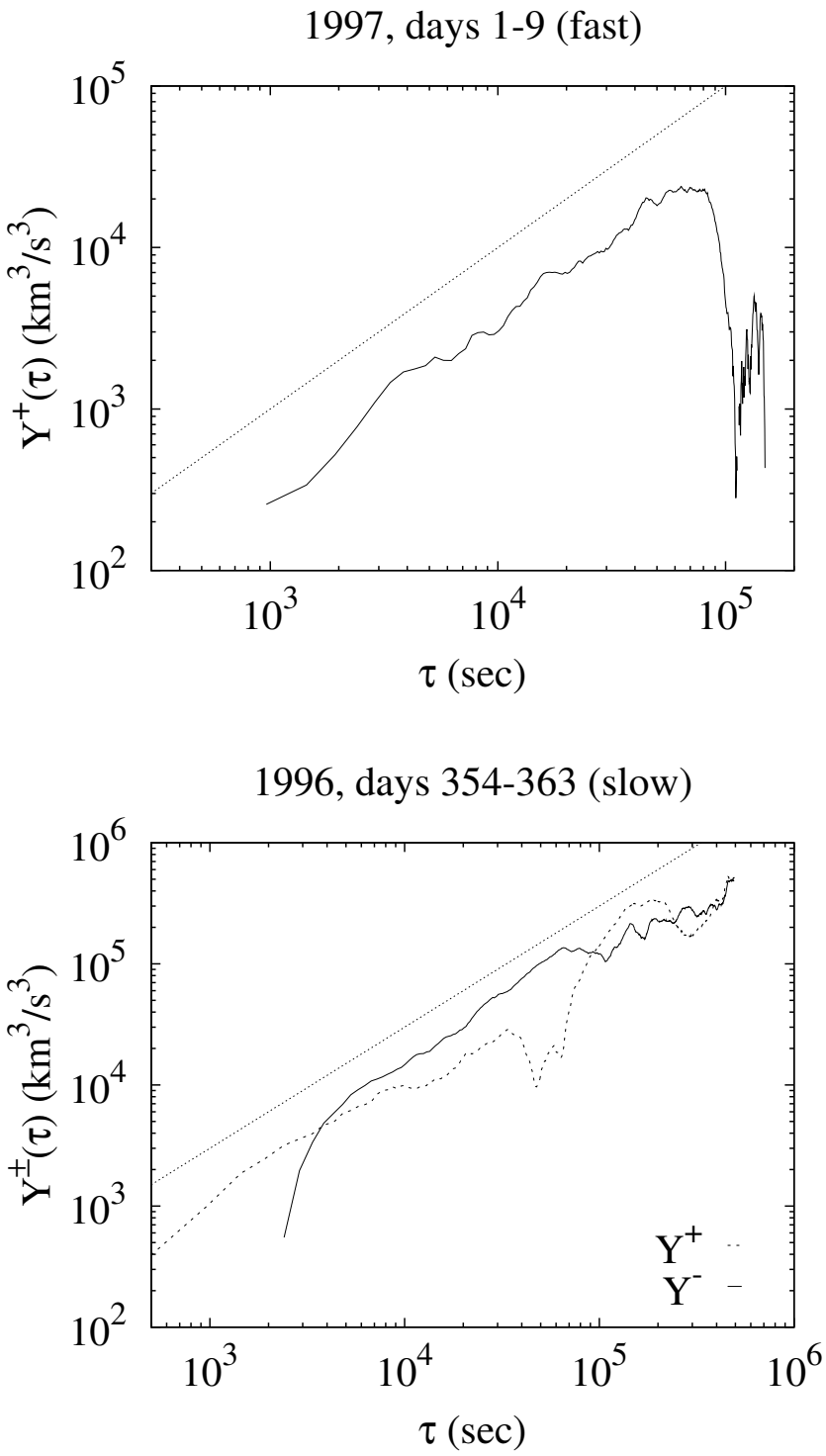

Figure 4.20: Top panel: scaling behaviour of Y^+ in the fast ecliptic wind. Bottom panel: scaling behaviour of both $Y^{\pm}$ in a slow wind stream. The solid line shows a linear scaling law to guide the eye.

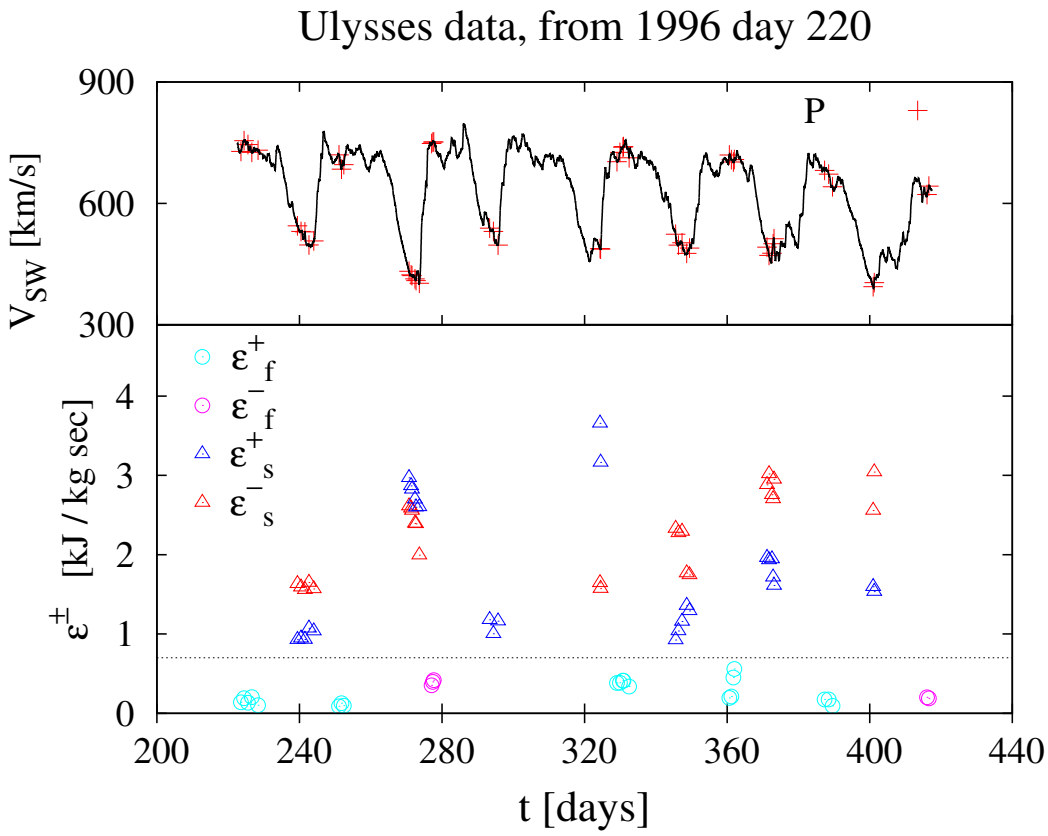

Figure 4.21: Top panel: the solar wind bulk speed and the starting points of each 11 days windows where scaling was observed (crosses). Bottom panel: the values of the estimated pseudo-energy transfer rates $\epsilon^{\pm}$ in the ecliptic wind measured by Ulysses starting from day 220 of 1996 (in $\mathrm{kJ\,kg^{-1}\,s^{-1}}$), for both fast (circles) and slow (triangles) wind. The values of the total energy $\epsilon_{tot} = (\epsilon^{+} + \epsilon^{-})/2$ are also shown (stars) where both pseudo-energy fluxes were available.

4.3 Heating the solar wind by the MHD turbulent cascade

The first models of solar wind proposed an adiabatic expansion of the plasma from the outer corona throughout the heliosphere. For such a model, the proton temperature T should decrease with the heliocentric distance r as $T(r) \propto r^{-4/3}$. Spacecraft measurements have shown that the temperature decay is in fact considerably slower than expected. Fits of the radial temperature profile gave an effective decrease $T \sim T_0(r_0/r)^{\xi}$ in the ecliptic plane, with the exponent $\xi \in [0.7 \div 1]$, much smaller than the adiabatic case (Schwenn 1983, Goldstein 1996). This observation implies that some heating mechanism must be at work within the wind plasma to supply the energy required to slow down the decay.

The nature of the heating process is an open problem. Among the heating sources, the dissipation of energy occurring at the end of a turbulent MHD cascade towards the dissipative scales could play an important role. This possibility has been explored in recent works, giving consistent results (Verma 1995, Vasquez 2007). However, the presence of an MHD turbulent cascade had not been proven so far, but only suggested by the well established observation of a Kolmogorov-like power-law spectrum of both kinetic and magnetic energy.

In this thesis, we compare the first reliable estimates of the MHD turbulent energy transfer rate with the heating rate necessary to reproduce the temperature radial decrease. As it has been explained in the previous section, we obtained the values of the turbulent energy transfer rate through a fit of the Yaglom law (3.16), using the mean velocity of the wind $\langle v_r \rangle_t$ through Taylor hypothesis. Observed values are collected in Table 4.24 and in Figure 4.23, and should now be compared to the heat flux estimated from temperature measurements. The physical processes involved in the cases in which we observed the scaling of $-Y^{\pm}(\tau)$ are not understood yet, so we chose to not consider them in this study. It should be noted that the flux contributing to the heating is in fact the *total energy* flux $\epsilon_{tot} = \epsilon^+ + \epsilon^-$. However, it is very rare to observe simultaneous scaling for both Elsässer variables. In the

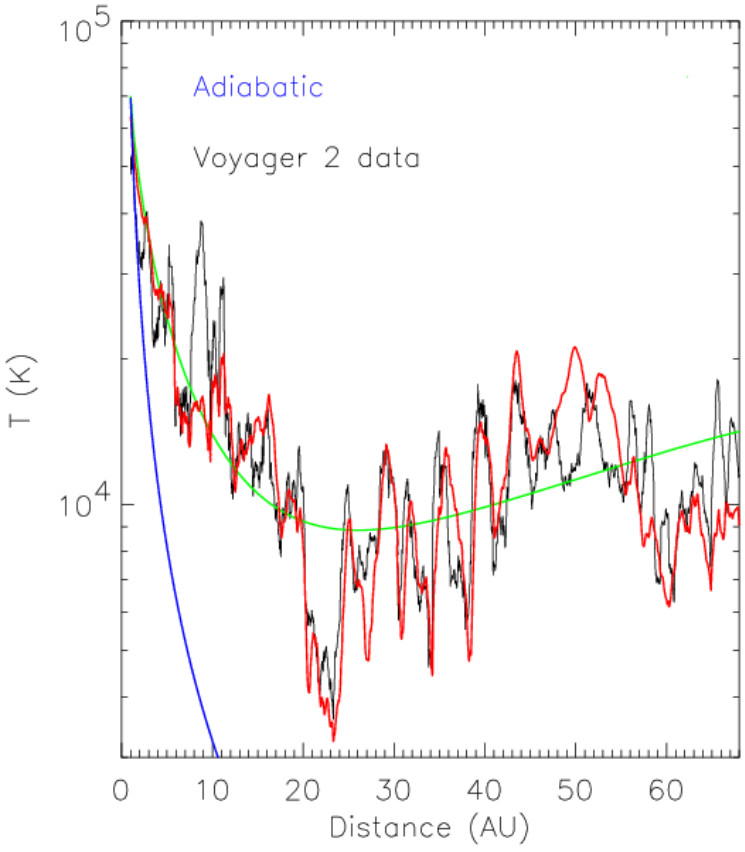

Figure 4.22: The radial proton temperature profile as measured by the spacecraft Voyager (black line) together with the adibatic trend (blue line).

few cases where it happens, we found that one of the fluxes $\epsilon^{\pm}$ is completely dominating the other. We thus used each measured value of $\epsilon^{\pm}$ as a surrogate for the energy flux ϵ_{tot} to increase the statistics on the dissipation, but the relation between the Elsässer pseudo-fluxes $\epsilon^{\pm}$ and the energy ϵ_{tot} and cross-helicity $\epsilon_C = \epsilon^+ - \epsilon^-$ fluxes is a very delicate and intriguing question that deserves further study through numerical simulations. We need now to obtain an estimate of the solar wind heating rate to compare it with the turbulent energy transfer rate. Verma et al. (1995) derived an expression for the radial temperature profile which includes, besides the adiabatic expansion heat loss, a correction due to the turbulent heating by dissipation processes occurring at the bottom of the energy cascade. Introducing the observed power-law temperature decrease $T \sim T_0(r_0/r)^{\xi}$, Vasquez (2007) used that relation to retrieve the heating rate ϵ_T at a given distance from the sun r

$$\epsilon_T(r) = \frac{3}{2}\left(\frac{4}{3} - \xi\right)\frac{V_{SW}(r)\, k_B\, T(r)}{r\, m_p}\ , \tag{4.1}$$

with $V_{SW}(r)$ being the radial profile of the bulk wind speed (which weakly fluctuates around 750 km/sec, see Table 4.24), k_B the Boltzmann constant and m_p the proton mass. This relation is obtained considering a polytropic index $\gamma = 5/3$ for the adiabatic expansion of the solar wind plasma, the protons being the only particle heated in the process. Such assumption are only partially correct, since the electrons could play a relevant role in the heat exchange. Heating rates obtained using (4.1) should thus be only seen as a first approximation that could be improved with better models of the heating processes. The Ulysses database provides two different estimates for the temperature, T_1, indicated as $T_{\rm large}$ in literature, and T_2, known as $T_{\rm small}$. In general, T_1 and T_2 are known to give sometimes an overestimate and an underestimate of the true temperature, respectively. So, we performed the whole analysis using both temperatures. From these, we estimated the heating rate at the same positions for which the energy cascade was observed, as indicated in Table 4.24. The bulk speed and temperature in equation (4.1)

are computed as moving averages within the same 11 days windows used for the turbulent cascade analysis. Scaling exponents of the temperature profiles ξ are evaluated independently by performing a power-law fit of the data over an extended dataset, from 1995 April 10^{th} to 1996 August 10^{th}. Since the relation between sampling times and heliocentric distance r is not linear, we first re-sampled the Ulysses temperature time series by averaging the data using a regular distance spacing, with step $\delta r = 0.01\,\mathrm{AU}$, so that the resampled temperature profile consists of 225 data points. This procedure is important to give every point the same weight for the fit, avoiding the effects of point clustering due to the spacecraft trajectory. Also, it has the advantage of filtering out small scale structures in the temperature, and provides an error bar estimate for each data point, evaluated as the standard deviation of the original data within each δr bin. Figure 4.23 shows the fit of the radial temperature profile for both T_1 and T_2, measured scaling exponents being $\xi_1 = 0.49 \pm 0.06$ and $\xi_2 = 1.10 \pm 0.08$ respectively. Values of ϵ_1 and ϵ_2 obtained from (4.1) are then plotted in Figure 4.25 and reported in Table 4.24, together with the corresponding turbulent transfer rates when the positive scaling law (3.16) is observed. It is worth mentioning that, from the assumed temperature profile and from equation (4.1), the radial decrease of the estimated heating will be trivially $\epsilon_T(r) \propto r^{-1-\xi}$.

We can now compare the estimated local heating rate of the solar wind plasma with the dissipation rate (equal to the transfer rate) of the turbulent cascade, as *measured* directly from the data. This makes a difference with previous works, where the values of the turbulent energy transfer rate were in fact *inferred* from the spectral properties of the wind (Verma 1995, Vasquez 2007). Figure 4.25 indicates that turbulent transfer rate represents a significant amount of the expected heating. Looking at Table 4.24, our results show that the MHD turbulent cascade contributes to the *in situ* heating of the wind from 8 % (T_1) to 50 % (T_2) on average, and up to 100 % in some cases (Marino et al., 2008). It should be thus considered as an important ingredient of the heating. However, the turbulent cascade alone seems unable to provide all the heating needed to explain the observed slowdown of the temperature decrease, in the framework of the model profile (4.1). Note that

turbulent dissipation and heating rates are much closer when the lower temperature measure T_2 is considered. The bottom panel of Figure 4.25 shows profiles of the observed turbulent dissipation, together with the corresponding temperature and estimated heating, computed at the same locations. The three signals present evident correlations, so that when the turbulent energy transfer rate increases, both temperature and the estimated heating also increase (Marino et al., 2008). Such correlations could be attributed to the leading role of the kinetic energy to the turbulent transport, since in polar, fast, hot wind the velocity is quite correlated with the temperature. On the other hand, the MHD scaling law (3.16) is not observed at all times in the solar wind. As we said, this could be due to many reasons: the presence of compressive effects, or the enhancement of local anisotropies or large scale inhomogeneities. All those effects have to be considered as possible sources of disturbance, inhibiting the full development of the *measurable* nonlinear turbulent cascade. They could also lead to underestimate the observed contributions from the turbulent cascade to the heating of the expanding wind. However, the indication that turbulent heating is present, and well correlated with the wind temperature, is already of great physical interest. In particular, we have evidenced that the energy contained at large scales, up to a few days, that can be introduced by the solar coronal structures, or by large scale structure of the solar wind, can be transported through the nonlinear interactions in a MHD turbulent cascade towards smaller scales, where conversion into heat can take place. However, the results presented here do not give any information about the dissipation mechanism itself.

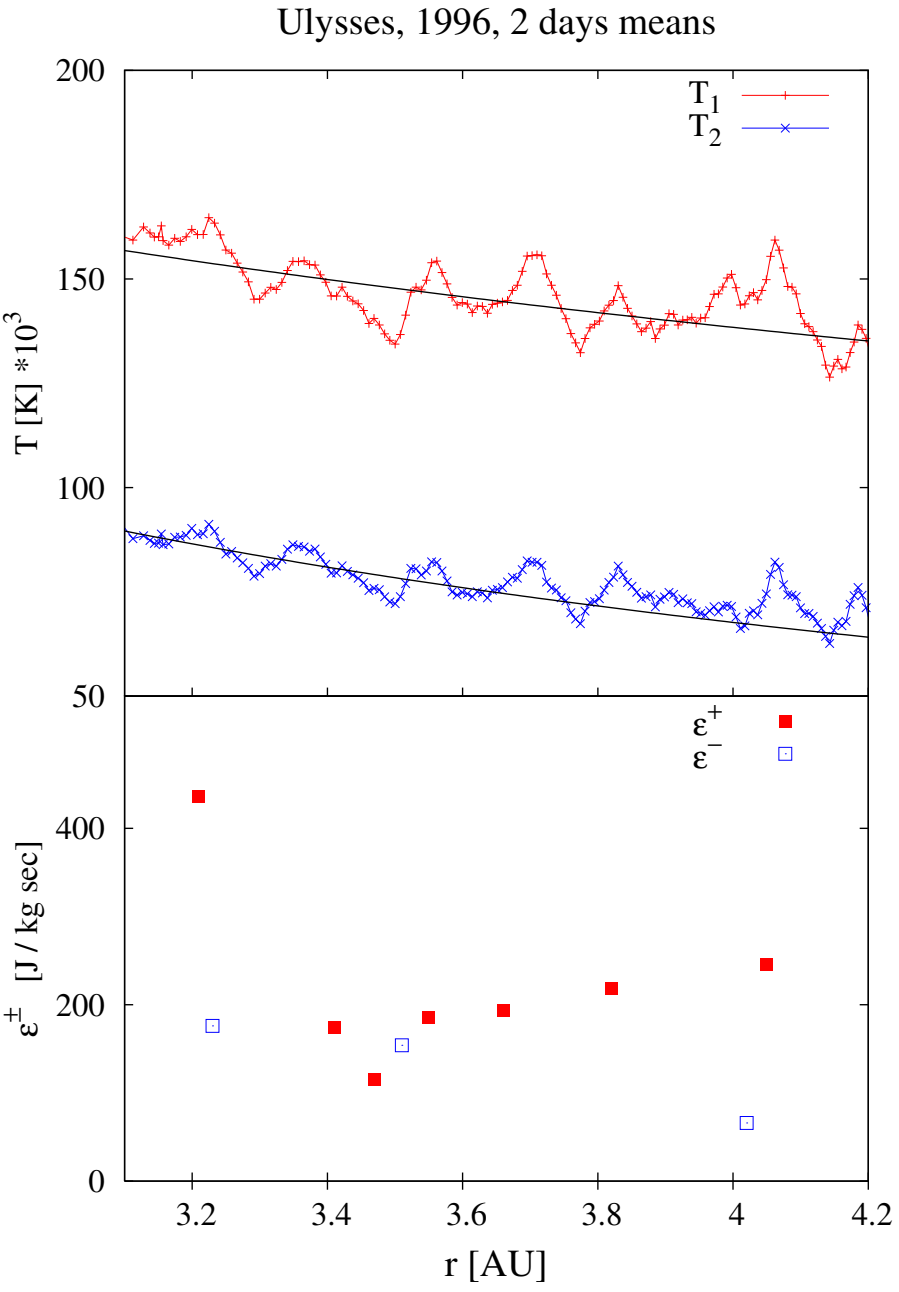

Figure 4.23: Top panel: the radial decrease of the temperatures T_1 and T_2 as measured by Ulysses during the first half of 1996 (2 days averages). Superimposed are the power law fits $T(r) \propto r^{-\xi}$, with $\xi_1 = 0.49 \pm 0.06$ and $\xi_2 = 1.10 \pm 0.08$. Bottom panel: the values of the turbulent pseudo-energy transfer rates, as obtained from the fit of the scaling law (3.16), in $\mathrm{J\,kg^{-1}\,s^{-1}}$. Squares refer to ϵ^+, circles to ϵ^-.

t_0	r	V_{SW}	T_1	T_2	ϵ_1	ϵ_2	$\lvert\epsilon^{\pm}\rvert$	$\lvert\epsilon^{\pm}\rvert/\epsilon_1$	$\lvert\epsilon^{\pm}\rvert/\epsilon_2$
21	3.22	765 ± 20	163 ± 18	90 ± 15	2696 ± 301	414 ± 68	436 ± 32	0.16	1.05
24	3.23	770 ± 19	164 ± 19	90 ± 15	2715 ± 314	412 ± 69	176 ± 13	0.07	0.43
56	3.42	764 ± 16	148 ± 20	81 ± 14	2308 ± 308	349 ± 62	174 ± 24	0.08	0.50
68	3.49	736 ± 18	136 ± 17	73 ± 12	2005 ± 256	298 ± 51	115 ± 19	0.06	0.39
69	3.49	734 ± 17	135 ± 17	73 ± 13	1983 ± 262	294 ± 53	113 ± 12	0.06	0.38
74	3.52	746 ± 24	145 ± 21	80 ± 16	2149 ± 320	326 ± 66	154 ± 32	0.07	0.47
81	3.56	769 ± 21	153 ± 19	82 ± 14	2304 ± 292	340 ± 60	185 ± 25	0.08	0.54
103	3.67	749 ± 20	147 ± 19	79 ± 15	2091 ± 271	309 ± 61	194 ± 22	0.09	0.63
135	3.83	760 ± 22	148 ± 27	81 ± 19	2044 ± 381	308 ± 75	218 ± 28	0.11	0.71
178	4.04	732 ± 25	146 ± 20	70 ± 18	1841 ± 259	245 ± 44	66 ± 24	0.04	0.27
184	4.06	743 ± 20	159 ± 18	82 ± 16	2031 ± 234	290 ± 58	216 ± 25	0.11	0.75
$\langle\cdot\rangle$	3.6	752	149	80	2197	326	186	0.08	0.56
$stdev(\cdot)$	0.3	15	10	6	285	51	95	0.03	0.22

Figure 4.24: The values of the measured turbulent energy transfer rates $\epsilon^{\pm}$ (in $\mathrm{J\,kg^{-1}\,s^{-1}}$) at different distances from the sun r (AU), along with the expected values of the heating rates $\epsilon_{1,2}$ (same units) as computed using the parameters V_{SW} ($\mathrm{km\,s^{-1}}$), $\xi_{1,2}$, and the two values of the temperature T_1 and T_2 measured by the Ulysses spacecraft (in 10^3K). All wind parameters were computed as mean values over 11 days windows, along with their standard deviations. In the case of the distance r, the variation within each 11 days window is roughly 0.05AU. The heating rates $\epsilon_{1,2}$ are estimated from the parameters in equation (4.1), using the two different values of the temperature. The first column indicates the initial time t_0 of the 11 days window in the time series (in day of the year 1996).

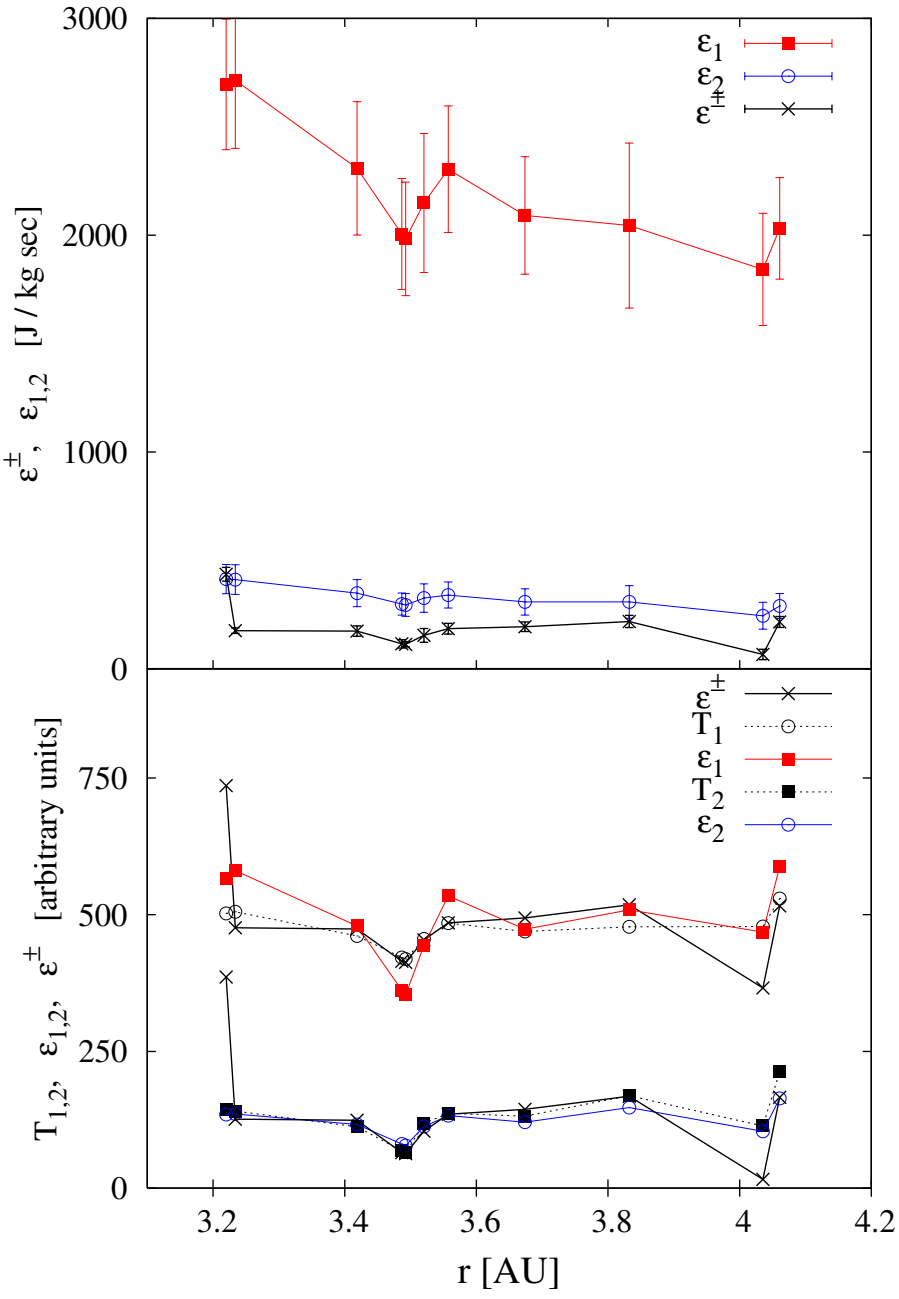

Figure 4.25: Top panel: the values of $\epsilon^{\pm}$ and $\epsilon_{1,2}$. Bottom panel: we compare the behaviour of the measured $\epsilon^{\pm}$ with the estimated $\epsilon_{1,2}$, after removing the $r^{-1-\xi}$ trend and adding an arbitrary offset. The same is done for the temperature $T_{1,2}$, where the $r^{-\xi}$ trend has been removed and arbitrary rescaling and offset have been applied. Units are arbitrary and offsets have been added to separate the two plots, to evidence the high correlation between the signals.

Chapter 5

The compressive turbulent cascade

5.1 Phenomenology in fluid and MHD turbulence

A first attempt to include density fluctuations in the framework of fluid turbulence was due to Lighthill (1955). He pointed out that in a compressible energy cascade, the mean energy transfer rate *per unit volume* $\epsilon_V \sim \rho v^3/\ell$ should be constant in a statistical sense (v being the characteristic velocity fluctuations at the scale ℓ), obtaining $v \sim (\ell/\rho)^{1/3}$. Fluctuations of a density-weighted velocity field $\mathbf{u} \equiv \rho^{1/3}\mathbf{v}$ should thus follow the usual Kolmogorov scaling $u^3 \sim \ell$. We introduce now the same phenomenological conjecture can be in MHD turbulence by considering the pseudo-energy dissipation rates per unit volume $\epsilon_V^{\pm} \equiv \rho\epsilon^{\pm}$, and introducing density-weighted Elsässer fields, defined as $\mathbf{w}^{\pm} \equiv \rho^{1/3}\mathbf{z}^{\pm}$. The equivalent of the Yaglom-type relation

$$W^{\pm}(\ell) \equiv \langle |\Delta\mathbf{w}^{\pm}|^2 \Delta w_{\parallel}^{\mp} \rangle \, \langle\rho\rangle^{-1} = -\frac{4}{3}\,\epsilon^{\pm}\,\ell \tag{5.1}$$

should then hold for the density-weighted increments $\Delta\mathbf{w}^{\pm}(\ell)$. Note that we have defined the flux $W^{\pm}(\ell)$ so that it reduces to $Y^{\pm}(\ell)$ in the case of constant density, allowing for comparisons between the compressible scaling (5.1) and

the purely incompressible one (3.16). Despite its simple phenomenological derivation, the introduction of the density fluctuations in the Yaglom-type scaling (5.1) seems to describe correctly the turbulent cascade for compressible fluid (or magnetofluid) turbulence. The law for the velocity field has been observed in recent numerical simulations (Kritsuk et al.,2007; Kowal et al., 2007).

5.2 Compressive turbulent cascade in solar wind

In this section we study the cascade properties of compressive MHD turbulence from solar wind data. In order to avoid as far as possible variations due to solar activity, or other ecliptic disturbances such as slow wind sources, coronal mass ejection, current sheets, we concentrate our analysis on pure Alfvénic state turbulence observed in high speed polar wind. In particular we use the same dataset and approach of the incompressive case, so we analyze the solar wind measured by Ulysses spacecraft in the first six months of 1996. Again we use the Taylor hypothesis, 8 minutes averaged time series of both Elsässer variables $\mathbf{z}^{\pm}(t)$ and density $\rho(t) = n_{\rm p} + 4n_{\rm He}$ (obtained as the sum of proton density and 4 times He density) to compute the density-weighted time series $\mathbf{w}^{\pm}(t)$. From this time series we calculate the increments $\Delta\mathbf{w}^{\pm}(\tau) = \mathbf{w}^{\pm}(t+\tau) - \mathbf{w}^{\pm}(t)$ for different time lags τ, and the third-order mixed structure functions $W^{\pm}(\tau) = \langle|\Delta\mathbf{w}^{\pm}(\tau)|^2 \Delta w_R^{\mp}(\tau)\rangle_t$ by time averaging $\langle\bullet\rangle_t$ over windows of fixed duration t. In order to eliminate instationarities, heliolatitude and heliocentric distance changes, and to explore the wind properties locally, averages are computed over a moving window of about 11 days, consisting of 2048 data points. We found that the third-order structure functions $W^{\pm}(\tau)$ computed from the Ulysses data show a linear scaling

$$W^{\pm}(\tau) \sim \frac{4}{3}\,\epsilon^{\pm}\,\langle v_R\rangle\,\tau \tag{5.2}$$

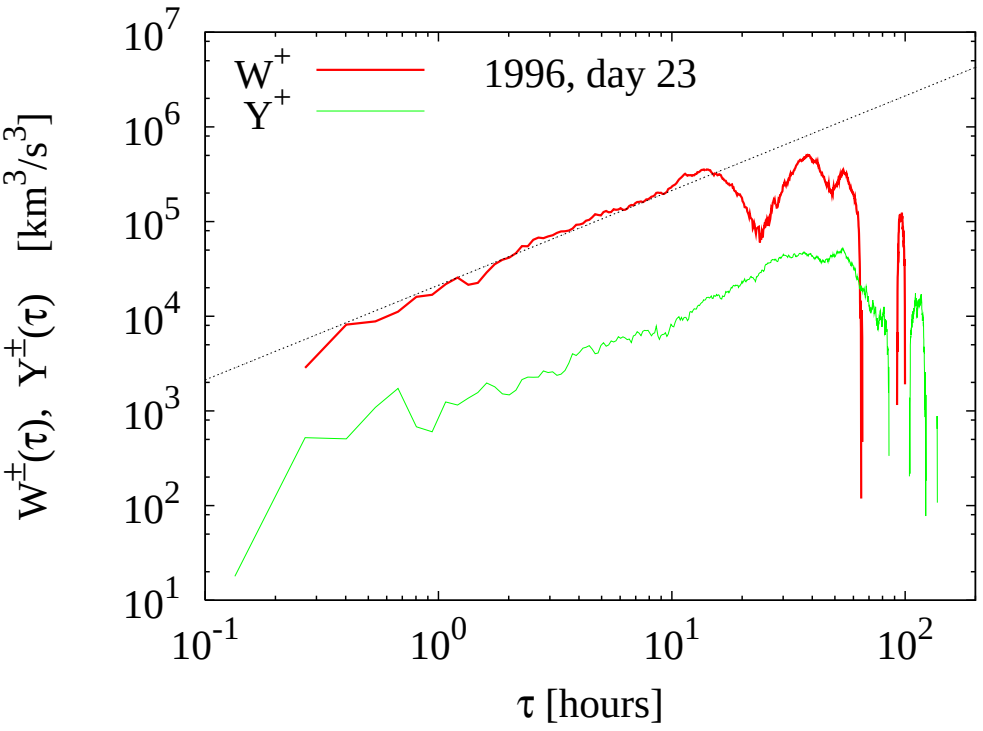

Figure 5.1: One example of the mixed third order compressible pseudo-energy flux $W^+(\tau)$ as computed from the Ulysses data during days 23 to 32 of 1996. The incompressible flux $Y^+(\tau)$ in the same time window and a linear fit are also indicated. In this case, both compressible and incompressible fluxes obey a Yaglom-like law.

during a considerable fraction of the period under study (Carbone et al., 2009a). In particular, we observed linear scaling of $W^+(\tau)$ in about half of the signal, while $W^-(\tau)$ displays scaling on about a quarter of the sample. As comparison, the corresponding incompressive scaling law for $Y^\pm(\tau)$ was only observed in a third of the whole period, considerably smaller than the compressible case. The portions of wind where the scaling is present are distributed in the whole period, and their extensions span from 6 hours up to 10 days. The linear scaling law generally extends on about 2 decades, from a few minutes to one day or more. For the compressible scaling, the two fluxes $W^\pm(\tau)$ coexist in a large number of cases. This does not hold for the incompressive scaling, where in general the scaling periods for the two fluxes $Y^\pm(\tau)$ are disjoint.

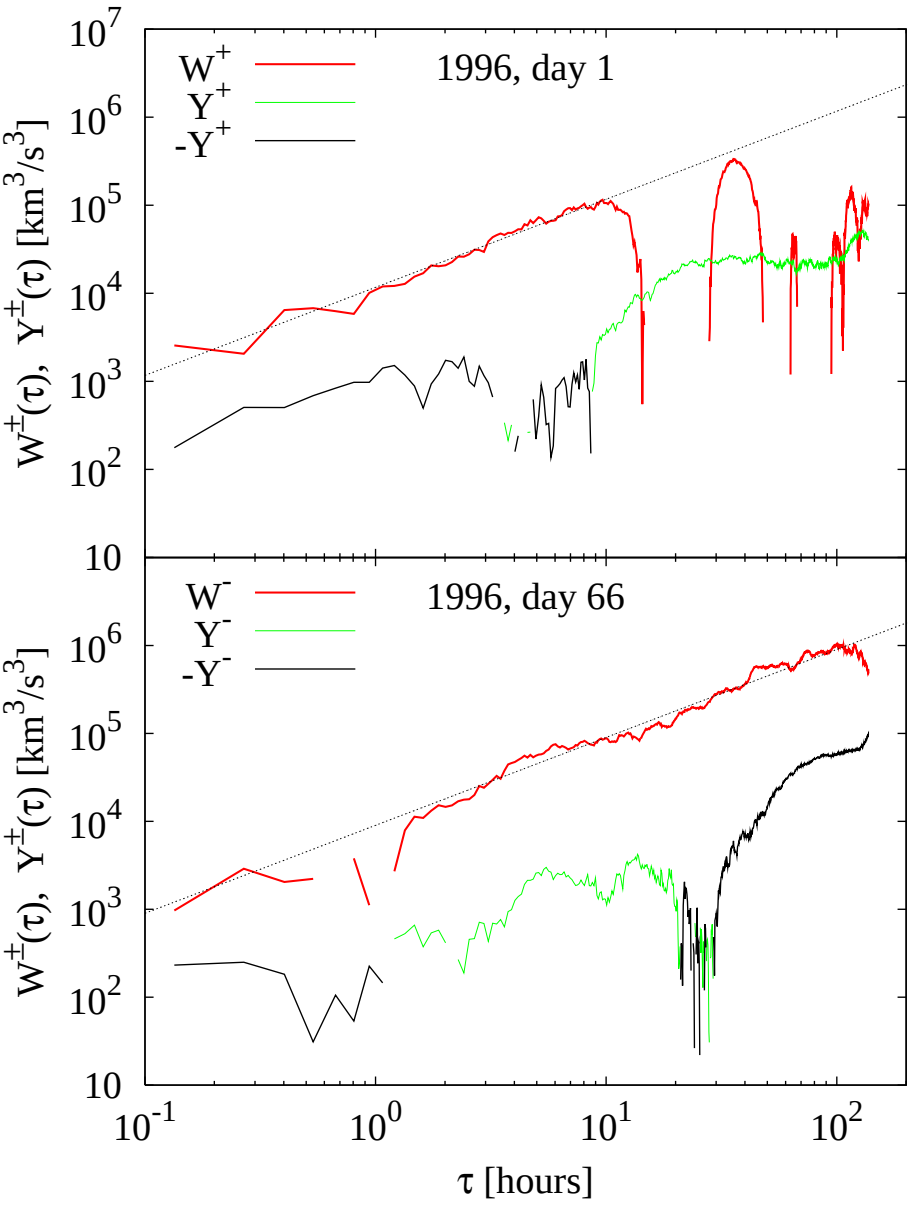

Figure 5.2: Top panel: an example of the third order compressible pseudo-energy flux $W^+(\tau)$ during days 1 to 10 of 1996. Bottom panel: $W^-(\tau)$ for days 66 to 75 of the same year. In both panels, the corresponding incompressible fluxes $Y^{\pm}(\tau)$ (no scaling present) and a linear fit are displayed.

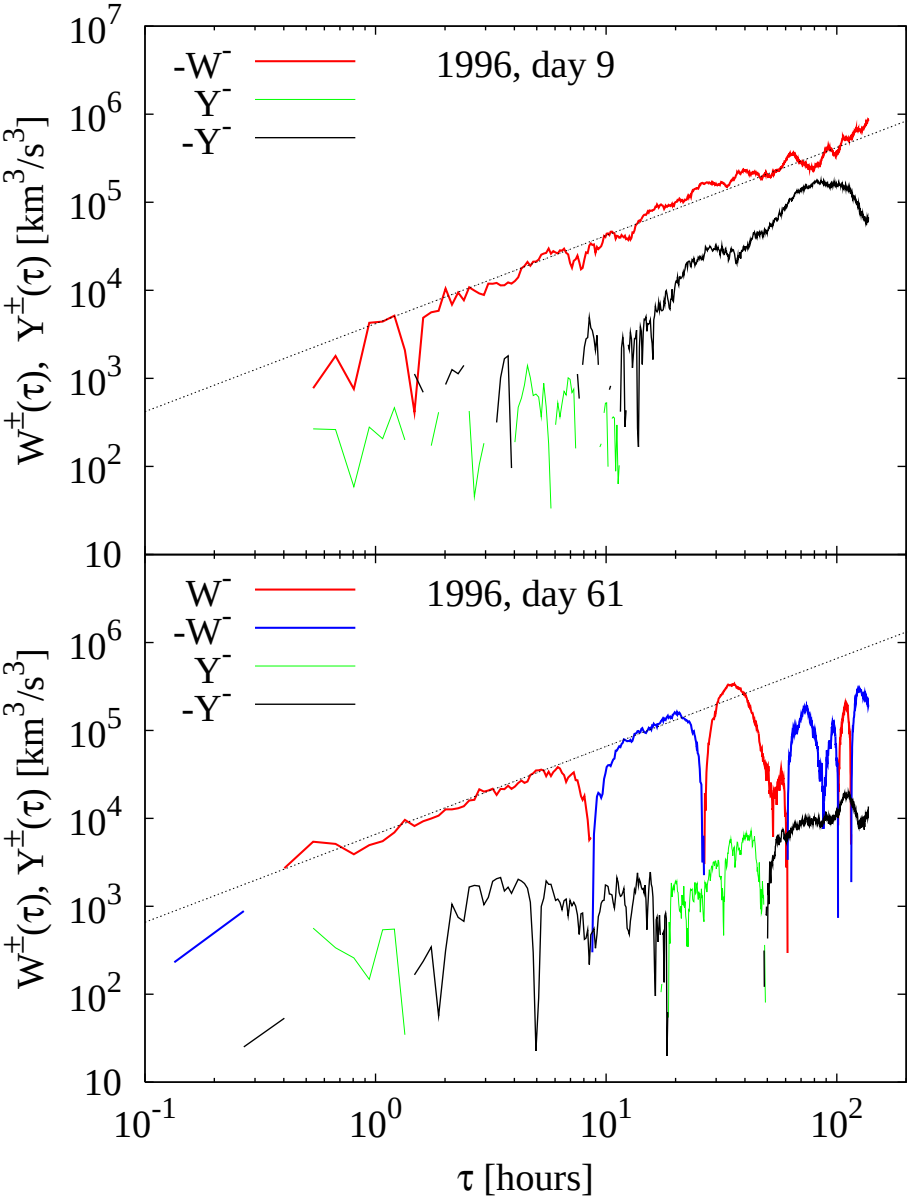

Figure 5.3: The top panel shows an example of the mixed third order pseudo-energy flux $-W^{-}(\tau)$ during days 9 to 18 from 1996. In this example, the scaling observed is negative defined. The origin of such signed scaling is not clear. Correspondingly, scaling of the incompressible flux $Y^{\pm}(\tau)$ in the same time window is not present. On the bottom panel, $W^{-}(\tau)$ presents two reduced scaling regions of opposite sign in a window starting on day 61 of 1996. As in the previous case, no scaling range is observed on the corresponding $Y^{\pm}(\tau)$.

Figure 5.1 shows one example of both mixed third-order structure functions $W^+(\tau)$ and $Y^+(\tau)$ computed in the same 11 days windows where the scaling was observed. Figure 5.2 shows two more examples of scaling, observed both for $W^+(\tau)$ and $W^-(\tau)$, in two different time windows. The $W^+(\tau)$ scaling extends over 2 decades, while $W^-(\tau)$ behaves linearly on the whole range of scales considered here (3 decades). In the last example, the scaling is not present for the incompressible fluxes $Y^{\pm}(\tau)$. This evidence shows that the inclusion of compressible effect through the density-weigthed fluctuations improves the scaling (3.16) and modify the energy cascade. In Figure 5.3 we report two cases in which $W^-(\tau)$ appears with the negative sign or shows both positive and negative. Also in the case of a compressive cascade is not clear if the sign of the mixed third order moment of the Elsässer variables is somehow related to the direction of the energy cascade. The scaling relation 5.1, as for the incompressive case, allows a direct estimate of the pseudo-energy transfer rates in the compressible case. A fit of the linear law 5.2 provides the local values of the amount of pseudo-energy transferred from large to small scales by the turbulent MHD cascade. This was already measured in the incompressive case (chapter 4), so that it is possible to compare the transfer rates in the two cascades. The mean values, computed over the 46 observed scaling cases at different radial distances from the sun, ($\pm$ their dispersion, in [J kg^{-1} sec^{-1}]) for the compressible cascade are $\epsilon^+ = 3668 \pm 1900$ (29 cases) and $\epsilon^- = 3536 \pm 2500$ (17 cases). Both values are considerably larger than the corresponding values for the incompressive case: $\epsilon_I^+ = 182 \pm 73$, 24 cases, and $\epsilon_I^- = 156 \pm 50$, 11 cases (Marino et al., 2008). This result shows again that the cascade in the solar wind is strongly enhanced by density fluctuations, despite their small amplitude. Note that the new variables are built by coupling the Elsässer fields with the density, before computing the scale dependent increments. Moreover, the third order moments are very sensitive to intense field fluctuations (intermittency), that could arise when density fluctuations are correlated with velocity and magnetic field. Similar results, but with considerably smaller effect, were found in numerical simulations of compressive MHD (Mac Low, 1999).

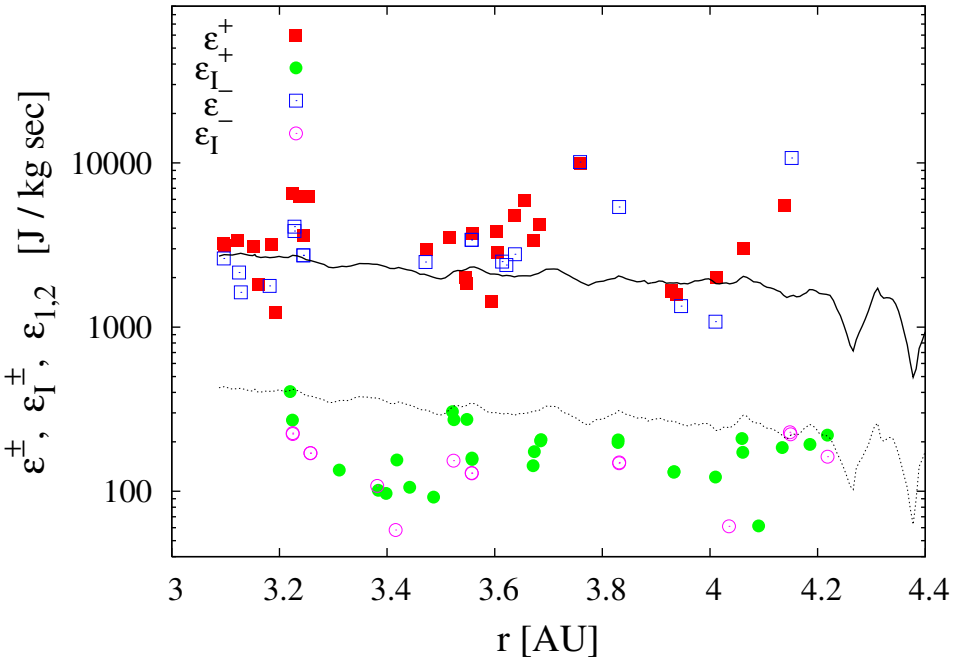

Figure 5.4: Radial profile of the pseudo-energy transfer rates obtained from the turbulent cascade rate through the Yaglom relation, for both the compressive and incompressive case. The solid lines represent the radial profiles of the heating rate required to obtain the observed temperature profile.

5.3 The role of density fluctuations in solar wind heating

As remarked previously, an interesting open question is the problem of the solar wind heating. We showed in the section 4.3 that the incompressible dissipation rate of pseudo-energies, measured through the equation (3.16), can only account for up to 50 % of the solar wind heating (Marino et al, 2008).

Figure 5.4 shows the radial profiles of the pseudo-energy transfer rates for both the compressive and incompressive cascades. In the same figure, we show the profiles of the heating rates needed to obtain the observed temperatures, as estimated from heating models (Verma,1995; Vasquez, 2007; Marino et al., 2008) and from the measured temperatures (the two different values refer to the different estimates of the temperature obtained from

Ulysses instruments). It is evident that, while the incompressive cascade cannot provide all the energy needed to heat the wind, the density fluctuations coupled with magnetohydrodynamic turbulence can supply the amount of energy required (Carbone et al., 2009a). This evidence shows the importance of the density fluctuations in polar, fast solar wind turbulence, confirming that it should be considered as an example of compressive fully developed MHD turbulence. Note that, since in a few samples we measured both ϵ^+ and ϵ^- in the same period, the values of the energy $\epsilon = (\epsilon^+ + \epsilon^-)/2$ and cross-helicity $\epsilon_H = (\epsilon^+ - \epsilon^-)/2$ transfer rates can be disentangled. From the values obtained, it is clear that the cross-helicity contribution, indicating the importance of the Alfvénic state of turbulence, can vary from a negligible fraction (less than 1 %) to a considerable 25 % of the energy contribution. Since its amplitude does not appear to be correlated with the observation of the cascade, Alfvénicity seems not to play a crucial role in the cascade at the observed scales. This would be in agreement with previous analysis of solar wind turbulence anisotropy, where the Alfvénic contribution to the field fluctuations is small (Bieber, 1996; Horbury, 2005).

CONCLUSIONS

The whole heliosphere is permeated by the solar wind, a supersonic and super Alfvénic plasma flow of solar origin which continuously expands into the space. This medium offers the best opportunity to study directly collisionless plasma phenomena, mainly at low frequencies where high-amplitude fluctuations have been observed. During its expansion, the solar wind develops a strong turbulent character, which evolves towards a state that resembles the well known hydrodynamic turbulence described by Kolmogorov. Because of the presence of a strong magnetic field carried by the wind, low-frequency fluctuations in the solar wind are usually described within a magnetohydrodynamic benchmark. Turbulence in the solar heliosphere plays a relevant role in several aspects of plasma behavior in space, such as solar wind generation, high-energy particles acceleration, plasma heating, and cosmic rays propagation. In the 1970s and 80s, impressive advances have been made in the knowledge of turbulent phenomena in the solar wind. However, at that time, spacecraft observations were limited by a small latitudinal excursion around the solar equator and, in practice, only a thin slice above and below the equatorial plane was accessible, i.e., a sort of 2D heliosphere.

In the 1990s, with the launch of the Ulysses spacecraft, investigations have been extended to the high-latitude regions of the heliosphere, allowing the characterization study of turbulence evolution in the polar regions. The polar wind is a flow in which the effects of large scale inhomogeneities are considerably less important than in low-latitude wind and, consequently, the turbulent evolution of its fluctuations results to be much slower. A specific property of turbulence is the scale invariance which manifests itself in the form of a *power law spectrum*. This viewpoint was first introduces in the

solar wind by Coleman (1968). On the other hand Belcher and Davis (1971) observed that during a substantial portion of the time, the velocity and the magnetic field fluctuation, not only are of the same magnitude, but are almost completely correlated. When this happens non-linear interactions in MHD turbulent flows cannot exist (as it's evident looking at the MHD equation written in terms of the Elsässer variables). This fact introduces a problem in understanding the evolution of MHD turbulence as observed in the interplanetary space. Both a strong correlation between velocity and magnetic fluctuations and a well defined turbulence spectrum are observed, and the existence of the correlations is in contrast with the existence of a spectrum which in turbulence is due to a non-linear energy cascade. Dobrowolny et al. (1980) started to solve the puzzle on the existence of *Alfvénic turbulence*, say the presence of predominately outward propagation and the fact that MHD turbulence with the presence of both Alfvénic modes present will evolve towards a state where one of the mode disappears.

In this thesis we rederive the Yaglom law for the MHD, a proportionality relation between the mixed third-order moment of the longitudinal increments of the Elsassër fields and the increment scale that is the equivalent of the Kolmogorov's law, the only exact and nontrivial theoretical result on turbulence. Using Ulysses spacecraft measurements, we observed *for the first time* the existence of such relation in solar wind which firmly enstablish the presence of a local energy cascade and the turbulent character of the field fluctuations. The scaling holds in a number of relatively long periods of about 11 days. Although our data might not fully satisfy requirements of homogeneity, incompressibility and isotropy everywhere, the observed linear scaling extends on a wide range of scales and appears very robust. This result estabilishes a firm point within solar wind phenomenology, and, more generally, provides a better knowledge of plasma turbulence, carrying along a wide range of practical implications on both laboratory fusion plasmas and space physics. The observation of the Yaglom law for MHD provided to obtain the *first direct estimation* of the pseudo-energy dissipation rate in solar wind hydrodynamic turbulence.

At this point we explored the possibility that the dissipation of energy

occurring at the end of a turbulent MHD cascade can be responsible for the solar wind heating. As a matter of fact spacecraft measurements show that the solar wind temperature decays slower than the adiabatic case as suggested by the first models of solar wind expansion. This discrepancy implies that some heating mechanism must be at work within the wind plasma to supply the energy required to slow down the cooling. We compared the energy dissipation rate measured from the Ulysses data with the local heating rate estimated through a model for the prediction of the turbulent heating rate values nedeed to justify the observed proton temperature profile. We found that incopressive turbulent cascade can contribute to the solar wind *in situ* heating from 8% to 50% on average, and up to 100% in some cases. The ecliptic wind measured by Ulysses has been also studied in this thesis using the same analysis performed in the polar wind. This has been done by separating fast and slow streams, in order to avoid mixing of different physical conditions. Our results show that while the fast ecliptic streams have similar properties as the polar fast wind, the slow streams show an highly enhanced energy transport, and a non negligible contribution from the cross-helicity terms of the Yaglom law. This evidence further support the need for separate analysis of the two types of wind.

The last part of this thesis project has been dedicated to the study of the role of large scale solar wind density fluctuations in the framework of the MHD turbulece. Using density-weighted Elsässer fields we showed that a phenomenological compressive Yaglom-like relation is verified to a large extent within the solar wind turbulence. This implies that low amplitude density fluctuations play a crucial role for scaling laws of solar wind turbulence. This observation also confirm the results for the Kolmogorov 4/5-law from numerical simulations of compressible turbulence (Mac Low, 1999), while no experimental evidences from real fluids had been found so far. This could be attributed to the incompressible nature of flows in ordinary fluids accessible to laboratory experiments. Here in fact, we presented the first experimental observation of relation 5.1 in real systems. Using solar wind data, we have had access to a sample of weakly compressible MHD turbulence in nature. Scaling law is found to be quite common and extends on a large range of

scales, indicating not only that a nonlinear MHD cascade for pseudo-energies is active in the solar wind turbulence, but also that compressible effects are an important ingredient of the cascade. Finally we pointed out that, if compared to the incompressive cascade, the compressive one is responsible for the transfer of a considerably larger amount of energy toward the small scales, where it can be dissipated to heat the plasma and seems to be sufficent to slow down the radial cooling of the wind as observed in interplanetary space.

Bibliography

[1] Akhiezer, A. I., Akhiezer, A., Polovin, R. V., Sitenko, A. G., and Stepanov, K. N., 1975, *Plasma electrodynamics, Vol. 2 Linear Theory*, Pergamon, New York, 1975.

[2] Balogh A., Southwood D.J., Forsyth R.J., Horbury T.S., Smith E.J., and Tsurutani B.T., *Science* **268**, 1007, 1995.

[3] Baroud C.N., Plapp B.B., She Z.S., Swinney H.N., *Phys. Rev. Lett.* **88**, 114501, 2002.

[4] Bavassano B., Dobrowolny M., Mariani F., Ness N.F., *J. Geophys. Res.*, **87**, 3617, 1982a.

[5] Bavassano B., Dobrowolny M., Fanfoni G., Mariani F., Ness N.F., *Solar Phys.*,**78**, 373, 1982b.

[6] Belcher J.M. and Davis Jr L., *J. Geophys. Res.* **76**, 3534, 1971.

[7] Belcher J.W. and Solodyna C.V., *J. Geophys. Res.*, **80**, 181, 1975.

[8] Bieber J.W., Wanner W., and Matthaeus W.H., *J. Geophys. Res.* **101**, 2511, 1996.

[9] Bruno R., Bavassano B. and Villante U., *J. Geophys. Res.* **90**, 4373, 1985.

[10] Carbone V., *Phys. Rev. Lett.* **71**, 1546, 1993.

[11] Carbone V., Marino R., Sorriso-Valvo L., Noullez A., Bruno R., *Phys. Rev. Lett.* **103**, 061102, 2009a.

[12] Carbone V., Sorriso-Valvo L., Marino R., *Europhys. Lett.* **88**, 25001, 2009b.

[13] Cerutti S. and Meneveau C., *Phys. Fluids* **12**, 1143, 2000.

[14] Coleman, P. J., Turbulence, viscosity and dissipation in the solar wind plasma, *Astrophys. J.*, **153**, 371, 1968.

[15] Danaila L., Anselmet F., Zhou T., Antonia R.A., *J. Fluid Mech.* **430**, 87, 2001.

[16] Denskat K.U. and Neubauer F.M., *Solar Wind Five*, **2280**, 81, 1983.

[17] Dobrowolny, M., Mangeney, A., and Veltri, P., Fully developed anisotropic hydromagnetic turbulence in the interplanetary space, *Phys. Rev. Lett.*, **45**, 144, 1980.

[18] Dobrowolny, M., Mangeney, A., and Veltri, P., *Astron. Astrophys.*, **83**, 26, 1980b.

[19] Elsässer, W. M., The hydromagnetic equations, *Phys. Rev.*, **79**, 183, 1950.

[20] Frisch, U., *Turbulence: the legacy of A. N. Kolmogorov*, Cambridge U. P., 1995.

[21] P. Goldreich P., and Sridhar S., *Astrophys. J.* **438**, 763, 1995.

[22] B.E. Goldstein, et al., *Astron. Astrophys.* **316**, 296, 1996.

[23] Grappin R., Pouquet A., Leorat J., *Astron. Astrophys.* **51**, 126, 1983.

[24] Horbury T.S., Forman M.A., and Oughton S., *Plasma phys. Control. Fusion* **47**, B703, 2005.

[25] Hundhausen, A. J., *Coronal expansione and Solar Wind*, Springer-Verlag, New York, 1972.

[26] Iroshnikov, P., *Sov. Astron.*, **7**, 566, 1963.

[27] Kolmogorov, A. N., Local structure of turbulence in incompressible fluid, *Dokl. Akad. Nauk SSSR*, **30**, 9–13, 1941, (in russian), translated in "Kolmogorov ideas 50 years on", *Proc. R. Soc. Lond. A*, **434**, 9–13, Eds. J.C.R. Hunt and O.M. Phillips, 1995.

[28] Kolmogorov, A. N., A refinement of previous hypotheses concerning yhe local structure of turbulence in a viscous incompressible fluid at high Reynolds number, *J. Fluid Mech.* **13**, 82–85, 1962.

[29] Kowal G. and Lazarian A., *Astrophys. J.* **666**, L69, 2007.

[30] Kraichnan, R. H., Inertial-range spectrum of hydromagnetic turbulence, *Phys. Fluids*, **8**, 1385, 1965.

[31] Kraichnan R.H., *J. Fluid Mech.*, **62**, 305, 1974.

[32] Kritsuk A.G., et al., *Astrophys. J.* **665**, 416, 2007.

[33] Landau, L. D. & Lifshitz, E. M., *Fluids Mechanics*, 2nd edition, Pergamon, Oxford, 1987.

[34] Lighthill M.J., *in IAU Symp. 2*, Gas Dynamics of Cosmic Clouds (Amsterdam: North Holland), 121, 1955.

[35] Mac Low M.M., *Astrophys. J.* **524**, 169, 1999.

[36] Marino R., Sorriso-Valvo L., Carbone V., Noullez A., Bruno R. and Bavassano B, *Astrophys J.* **677**, L71, 2008.

[37] Marino R., Sorriso-Valvo L., Carbone V., Veltri P., Noullez A. and Bruno R., *Planetary and Space Science.*, submitted 2009.

[38] Matthaeus, W. H., *Geophys. Res. Lett.*, **9**, 660, 1982.

[39] Matthaeus W. H., *Paper presented at 1986 Sherwood Controlled Fusion Theory Conference, Courant Institute of Mathematical Sciences, New York*, 1986.

[40] Matthaeus W.H., Goldstein M.L., Montgomery D.C., *Phys. Rev. Lett.*, **51**, 1484, 1982.

[41] Meyer-Vernet N., *Basics of solar wind*, Cambridge, 2007.

[42] Monin A.S., Yaglom A.M., *Statistical Fluid Mechanics, Vol 2*, MIT Press, 1975.

[43] Politano, H., Pouquet, A. and Sulem, P. L., *Phys. Plasmas*, **2**, 2931, 1995.

[44] Politano, H. & Pouquet, A., *J. Geophys. Lett.*, **25**, 273, 1998.

[45] Richardson, L. F., *Weather prediction by numerical process.*, Cambridge University Press, 1922.

[46] Russell C.T., *Solar Wind*, 365, 1972.

[47] Schwenn R., *Solar Wind Five*, NASA Conf. Publ., CP-2280, 489, 1983.

[48] Smith E.J., Marsden R.G., and Page D.E., *Science* **268**, 1005, 1995.

[49] Sorriso-Valvo, L., Carbone, V., Consolini, G., Bruno R., & Veltri, P., *Geophys. Res. Lett.*, **26**, 13, 1801–1804, 1999.

[50] Sorriso-Valvo L., Carbone V., Bruno R. and Veltri P., *Europhys. Lett.* **75**, 832, 2006.

[51] Sorriso-Valvo L., Marino R., Carbone V., Noullez A., Lepreti F., Veltri P., Bruno R., Bavassano B., and Pietropaolo E., *Phys. Rev. Lett.* **99**, 115001, 2007.

[52] Taylor, G. I., The spectrum of turbulence, *Proc. R. Soc. A*, **164**, 476, 1938.

[53] Tu, C. Y. & Marsch, E, *MHD structures, waves and turbulence in the solar wind*, Kluwer Academic Publishers, London, 1995; reprinted from *Space Science Rev.*, **73**, Nos. 1–2, 1995a.

[54] Tu, C. Y. & Marsch, E, *J. Geophys. Res.*, **100**, 12323, 1995b.

[55] Vasquez B.J., Smith C.W., Hamilton K., MacBride B.T., and. Leamon R.J., *J. Geophys. Res.* **112**, A07101, 2007.

[56] Veltri, P. & Mangeney, A., Scaling Laws and Intermittent Structures in Solar Wind MHD Turbulence, *Solar Wind Nine*, Proceedings of the Ninth International Solar Wind Conference, Nantucket, MA, October 1998. Edited by S. R. Habbal, R. Esser, J. V. Hollweg, and P. A. Isenberg. AIP Conference Proceedings, Vol. 471, 1999.

[57] Verma M.K., Roberts D.A., and Goldstein M.L., *J. Geophys. Res.* **100**, 19839, 1995.